DOCTORAL THESIS

MARISE JACOBA ERIKA WESTBROEK

PATH INTEGRAL APPROACH TO DARCY FLOW

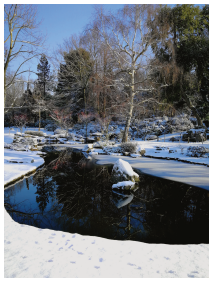

SIMULATION OF FLOW THROUGH STOCHASTIC POROUS MEDIA USING MONTE CARLO METHODS AND SIMULATED ANNEALING

Department of Earth Science and Engineering
Imperial College London, 2019

E-MAIL:
marisewestbroek@gmail.com

The titlepage includes a photograph of Kyoto Gardens in Holland Park, London, taken on 1 March 2018.

DECLARATION OF ORIGINALITY

Most of the work presented in this thesis was done by the author, under the supervision of Prof. Peter R. King and Prof. Dimitri D. Vvedensky, and in collaboration with Dr. Stephan Dürr and Dr. Ronnie L. Schwede. Any results that were not arrived at by the author are appropriately referenced.

COPYRIGHT DECLARATION

ACKNOWLEDGEMENTS

I wish to thank my supervisors, Peter and Dimitri, for their support. Peter, thank you for your continual confidence in me and in the power of path integrals, without which this project would never have taken place. Dimitri, thank you for your rigor in going through my work. 'My' papers became 'our' papers under your critical eye.

A special thanks goes to my informal tutor, Stephan. Without your kindness in taking the time to introduce me to the technicalities of path integrals on a lattice, I would still be reading about the harmonic oscillator. I would like to thank my patient collaborator Ronnie for introducing me to the wonders of field generators and parallelization. It was a pleasure to work with you. I am also indebted to former MSc student Gil-Arnaud Coche. Thank you for helping me to get started. I owe Andrew Duncan a word of thanks for his excellent lectures on applied and computational stochastic processes and his in-depth answers to my questions. I would like to thank the members of the Condensed Matter Theory Group for the enlightening lunchtime conversations.

From those closest to me, I have received support of a different kind. *Mama, je bent mijn grootste steun geweest tijdens mijn werk aan dit proefschrift. Papa, je blijft mijn held. Je bent altijd bij me.* Kelly, thank you for your support in terms of physics and life more generally. Thank you, simply, for being my friend.

Finally, I would like to acknowledge the financial support I have received through a Janet Watson scholarship from the Department of Earth Science and Engineering and a studentship in the Centre for Doctoral Training on Theory and Simulation of Materials funded by the EPSRC (EP/L015579/1), both at Imperial College London.

ABSTRACT

We explore a path integral approach to Darcy flow through a stochastic permeable medium. In one dimension, Darcy's law can be solved exactly. We give a derivation of the path integral used to obtain the Darcy pressure statistics. We also outline the computational setup for the conventional finite-volume method and the implementation of a stochastic field generator. We provide a detailed user's guide to the calculation of path integrals on a lattice, including an explicit computational setup and corresponding pseudocode. The higher-dimensional form of Darcy's law lacks an analytic solution. We show that the simulated annealing algorithm provides a viable alternative to simulating a path integral for Darcy's law. We compare the results for the path integral and simulated annealing methods to those for the finite-volume method. All comparisons pass a Kolmogorov-Smirnov test at the 95% confidence level. We discuss log-normal and Gaussian fits to the pressure statistics. Finally, we make a number of suggestions for future work, such as the use of the renormalization group and the extension of Darcy's law to multiphase flow.

CONTENTS

LIST OF FIGURES

LIST OF TABLES

1 INTRODUCTION

Readers with a physics background will be familiar with the problem of measuring the position of a quantum particle. The position of a classical particle with mass m can be determined at any given time, provided the initial conditions and sufficient information about any external forces are available. The position of a quantum particle, by contrast, is not deterministic. Suppose a quantum particle is observed at position x_A at time t_A, and again at position x_B at time t_B. Even given full details on the circumstances, we cannot reconstruct the particle's trajectory.

This fundamental difference between classical and quantum mechanics is central to modern day physics. Its understanding goes back to the middle of the 19^{th} century. In 1859, Kirchhoff showed that the emission and absorption of electromagnetic radiation of bodies in thermal equilibrium is wavelength-specific [64]. Boltzmann suggested that the energy levels of a system could be discrete in 1877. In 1887, Hertz discovered the photoelectric effect: electrons can be dislodged from a material by shining light on it if the frequency of the light waves exceeds a certain threshold. Einstein's 1905 explanation of this effect [37] postulated that light was made of individual quantum particles, consistent with Planck's hypothesis that any energy-radiating system can be divided into a number of discrete "energy elements". The theory of quantum mechanics was developed by Bohr, Heisenberg, Schrödinger, Pauli and others in the 1920s [16, 93].

Schrödinger's equation and Heisenberg's matrix mechanics are based on Hamiltonian classical mechanics. Their theoretical frameworks explain the statistical approach taken to the position of a quantum particle. For an accessible discussion of the nature of such a statistical characterization, see Ref. [48]. In 1933, Dirac [29, 30] proposed an approach to quantum mechanics based on the Lagrangian, which he regarded as more fundamental than the Hamiltonian. Dirac suggested that the transition amplitude in quantum mechanics, also called the propagator, correspond to the quantity $\exp(iS/\hbar)$, in which S is the classical action evaluated along the path the particle takes.

In 1948, Feynman [38] extended Dirac's ideas and formulated quantum mechanics based on the sum over *all* paths between fixed initial and final states. Each path contributes a pure phase $\exp(iS/\hbar)$ to the propagator, as Dirac suggested, with the amplitudes of the paths combined according to the usual quantum mechanical procedure for the superposition of amplitudes. Because the sum over paths is typically an integral over a contin-

uum of paths, this procedure is now known as the "path integral method". Feynman derived his path integral method in a seminal paper [38] that laid the foundation for many formal developments of path integrals in quantum physics [52], such as perturbation theory, the pictorial representations of the behavior of subatomic particles that are now known as "Feynman diagrams" [15, 39] and lattice quantum chromodynamics, a lattice gauge theory formulated on a grid. The path integral also has applications in other areas of physics, including statistical mechanics [97], and stochastic dynamics [101].

In fact, although largely unknown to the physics community at that time, the notion of the integral over paths had been introduced in the 1920s by the mathematician Norbert Wiener [98] for diffusion and Brownian motion. Wiener's presentation had a similar formal structure to the Feynman path integral, though in a purely classical context [15, 59]. For details on Feynman's extension of the Wiener measure to quantum mechanics, we refer to a review article by Gel'fand and Yaglom [43].

The path integral is an explicit expression for the probability amplitude. Once we have the path integral, we are *in business*[1]: we can calculate the expectation value of the position at any time, higher-order moments of the position, correlations between the positions at various times, et cetera.

Readers with an engineering background, on the other hand, will be familiar with the problem of calculating the pressure of Darcy flow through a porous material. Extensive descriptions of flow through porous media can be found in Refs [55, 87, 92]. The field is fundamental to many areas of science, including filtration [103], geothermal engineering [2], hydrology [92], materials science [7] and even physiology [53, 61, 62]. It is also relevant to the flow of oil in a reservoir, which will be the application presented in this thesis.

The ways to describe flow and transport in a porous medium fall into (at least) two conceptually different categories; for a review, see Ref. [9]. The first is to carry out any desired calculations at the pore scale. One approach is to solve the Navier-Stokes equations, developed by Navier and Stokes in 1822 [4, 10], which encode conservation of momentum for a fluid. The equations arise from applying Newton's second law to fluid motion, together with the assumption that the stress in the fluid is the sum of a diffusing viscous term and a pressure term. The Navier-Stokes equations can be solved computationally on domains on the millimeter to centimeter scale, when the structure of the medium is known exactly and the necessary computational power available, with the proviso that the initial conditions are known. The solution to the Navier-Stokes equations yields the pressure and the flow at any position in the medium.

1 Turn of phrase borrowed from René van Roij.

Pore-scale simulations [5], using the lattice-Boltmann method [19, 77] or cellular automata [85], provide another avenue to a detailed description of the flow. On this microscopic scale, the pore space and fluid configurations can be imaged using X-ray microcomputed tomography [32, 69].

Some problems related to flow through a porous material, such as the flow of oil through a reservoir, require flow and pressure descriptions on the kilometer scale. Due to the limited availability of information about the pore structure, pore-scale simulations cannot be realized on the kilometer scale. Note that this problem, contrary to that of the positions of a quantum particle, is not fundamental. It is merely an issue of lack of information. However, the problem poses practical considerations. Even in the hypothetical case that full information about the rock permeability were known, the computational demands associated with the calculation of a pressure field would be prohibitive.

Instead, the problem calls for coarse-graining of the medium and the flow over regions large on the pore scale but small on the scale of the macroscopic system. Typically, permeability data are only available at a limited number of points in the rock. On the "mesoscopic" scale, it is necessary to have an appropriate stochastic description of the permeability. An overview of the various methods for reservoir modeling is given in Refs [20, 82].

For the problem of slow flow of a viscous fluid, Darcy's law provides a reliable description of the average flow rate and the average pressure gradient, given the stochastic permeability. Darcy proposed his law as an empirical relation in 1856, in his work *"Les fontaines publiques de la ville de Dijon"* [24], which described the design of a network of pipes to bring spring water into the city. Darcy realized the importance of sand filters to drinking water, and based his law on a series of flow experiments. One can, however, derive Darcy's law by averaging Stokes flow over a representative volume element and observing that viscous forces predominate in the case of a viscous fluid, and that a pressure gradient is required for flow at constant velocity [47, 75, 96]. Another way to arrive at the same conclusion is to do a scaling analysis of Stokes flow through a dilute random array of fixed obstacles [86].

Often in reservoir engineering, the pressure p_A at point x_A as well as the pressure p_B at point x_B can be fixed. The analogy with the quantum particle does not need further elucidation. The aim of this thesis, as the title hints, is to develop a path integral approach to Darcy flow. Based on the cornucopia of literature on the path integral (for a thorough review, see [104]), we expect to be able to develop such an approach and use it to calculate Darcy flow. A path integral approach to Darcy flow will make the arsenal of techniques developed for path integrals available to the problem of Darcy flow through a permeable medium. Previous derivations [3, 33, 89] of path integrals related to Darcy's law have used their analytic properties to determine general

flow characteristics. This thesis focuses on comparison of the Darcy pressure statistics obtained from the path integral to those obtained through the numerical integration of Darcy's law using the conventional finite-volume method. It highlights the strengths and weaknesses of introducing the path integral to the problem of flow through random porous media and provides a user's manual for its implementation.

1.1 OUTLINE

Chapter 2 gives the necessary background on Darcy's law, including its analytic solution in one dimension. Chapters 3 and 4 explore the toy problem of one-dimensional pressure calculations: Chapter 3 introduces traditional computational techniques, while Chapter 4 outlines the path integral formalism. In Chapter 5, a user's manual is given. It should provide enough details for the interested reader to calculate her or his own path integral. Chapter 6 presents the results obtained using the theory and computational background given in previous chapters. In Chapter 7, the extension of the main problem to higher dimensions is discussed. This chapter addresses the limitations of the path integral approach and introduces an alternative method where the original approach breaks down. Chapter 8 contains the higher-dimensional results achieved through the methods described in Chapter 7. Finally, Chapter 9 contains a summary and suggestions for future work, including the application of the renormalization group to the Darcy path integral and the extension of Darcy's law to multiphase flow. All mathematical details, as well as pseudocode, can be found in the Appendices.

1.2 LIST OF PUBLICATIONS

A subset of the work described here has already been published in scientific journals.

- Marise J. E. Westbroek, Peter R. King, Dimitri D. Vvedensky and Stephan Dürr. "User's guide to Monte Carlo methods for evaluating path integrals." In: *American Journal of Physics* 86 (20 March 2018) pp. 293-304. DOI: 10.1119/1.5024926.
- Marise J. E. Westbroek, G.-A. Coche, Peter R. King and Dimitri D. Vvedensky. "Evaluation of the path integral for flow through random porous media." In: *Physical Review E* 97 (12 April 2018), pp. 042119-042123. DOI: 10.1103/PhysRevE.97.042119.

Some preprints of further publications are also available.

- Marise J. E. Westbroek, G.-A. Coche, Peter R. King and Dimitri D. Vvedensky. "Pressure statistics from the path integral for Darcy flow through random porous media." Available at: arXiv:1811.01781.
- S. Mittal, Marise J. E. Westbroek, Peter R. King and Dimitri D. Vvedensky. " Path integral Monte Carlo method for the quantum anharmonic oscillator." Available at: arXiv:1811.04669.

Two more papers are in progress.

1.3 LIST OF PRESENTATIONS

The work in this thesis has been presented at various conferences, summer schools and institutions, resulting in valuable feedback and collaborations.

- *Physics by the Lake*: two-week national summer school on theoretical condensed matter physics - poster presentation (2015).
- *New England Complex Systems Institute*: two-week international summer school on complex systems science (2016).
- *ECMOR XV*: European Conference on the Mathematics of Oil Recovery - conference talk (2016).
- *Nordita*: the Nordic Institute for Theoretical Physics - invited seminar (2017).
- *Royal Dutch Shell*: Shell Projects & Technology NL - invited lunchtime seminar (2017).
- *Interpore*: International Society for Porous Media - conference talk (2017).
- *SIAM GS*: Conference on Mathematical and Computational Issues in the Geosciences - conference talk (2017).
- *Total S.A.*: Geoscience Research Centre, Aberdeen - invited seminar (2017).
- *Bergische Universität Wuppertal* - invited seminar (2018).
- *Saint Ann's School, New York City* - two outreach talks (2019).

2 DARCY'S LAW

2.1 INTERPRETATION AND APPLICABILITY

This thesis is restricted to a consideration of single-phase flow, in which one fluid saturates the pore space. The methodology is illustrated for the example of the slow flow of oil through a rock. For the present case of the slow flow of a viscous fluid, Darcy's law relates the flow rate q and the average pressure gradient ∇p to the effective stochastic permeability K:

$$q = -K\nabla p. \tag{1}$$

Here, $K = k(x)/\mu$, where k is the stochastic permeability of the medium and μ is the viscosity of the fluid. For the work presented in this thesis, we used a log-normal model for the effective permeability K, which will henceforth be referred to as the permeability. This permeability model has the required feature of strict positivity. Published work suggests that the log-normal model is a realistic one [40]. It should be pointed out, however, that the permeability can be represented by any other stochastic model with a well-defined mean and covariance. The typical flow speed is approximately 10 centimeters per day.

Oil is a relatively incompressible fluid:

$$\nabla \cdot q = 0. \tag{2}$$

Together with Darcy's law, (1), the conservation of volume (2) yields the result

$$\nabla \cdot (K\nabla p) = 0. \tag{3}$$

2.2 ANALYTIC SOLUTION IN ONE DIMENSION

To develop an intuition for Darcy's law, this Section solves the one-dimensional case. This form of Darcy's law, initially intended as a toy model, turns out to be fundamentally different from its higher-dimensional analogue.

The one-dimensional toy model is a "rock" of length X, with viscous flow only along the x-axis (see Fig. 1). The one-dimensional form of Darcy's law

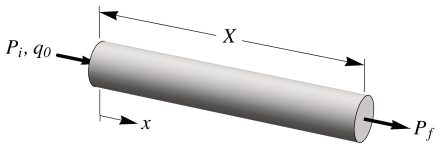

Figure 1: Schematic depiction of one-dimensional flow through a permeable medium. The term "one-dimensional flow" refers to the number of spatial coordinates required to describe the flow.

(1) reads:

$$q(x) = -K(x)\frac{dp(x)}{dx}. \tag{4}$$

In one dimension, incompressible flow reduces to constant flow:

$$q(x) = q_0. \tag{5}$$

It is straightforward to integrate the differential equation (4) subject to the initial condition

$$p(0) = P_i,$$

as follows:

$$p(x) = P_i - q_0 R(x), \tag{6}$$

where

$$R(x) = \int_0^x \frac{1}{K(x')}\, dx'. \tag{7}$$

The integral over $1/K(x)$ has the interpretation of a resistance term.

Setting $x = X$, we obtain a relation between the flow q_0 and the final pressure P_f:

$$P_f = P_i - q_0 R(X), \quad \text{or } q_0 = -\frac{P_f - P_i}{R(X)}. \tag{8}$$

To solve for $p(x)$, one additional variable must be specified. Imposing q_0, the derivative of $p(x)$ at the boundary, defines a Neumann boundary condition (NBC). In oil field terms, fixed q_0 corresponds to a constant production. The specification of P_f, the pressure at the other end of the well, is mathematically is mathematically known as a Dirichlet boundary condition (DBC).

We let $L(x) = \log K(x)$ denote the log-permeability of the rock. The Gaussian random variable $L(x)$ can be effectively modeled as a stationary

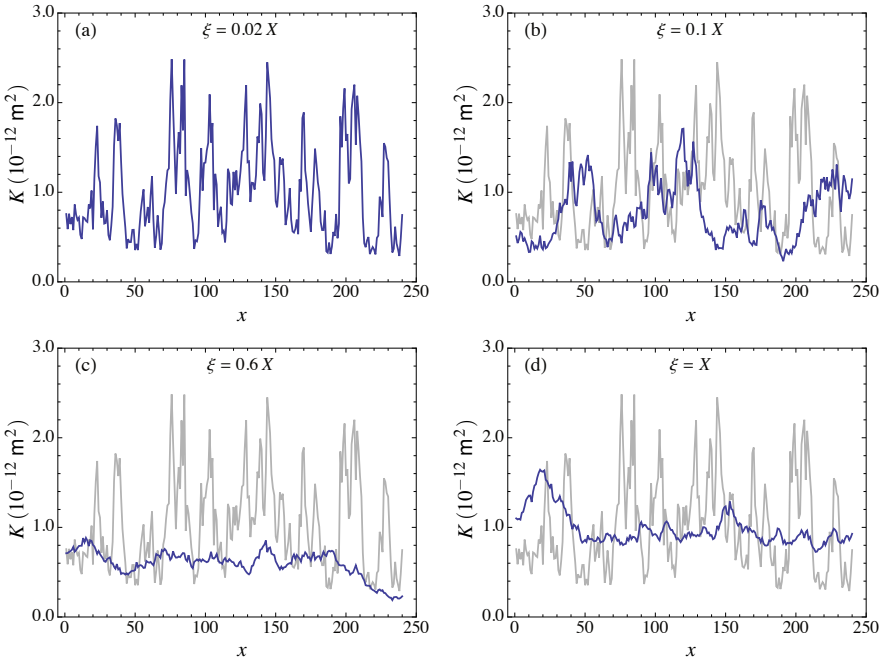

Figure 2: Realizations of the permeability $K(x)$, for the indicated correlation lengths obtained from a stationary Ornstein-Uhlenbeck process with the correlation function (9). For $\xi = 0.02X$ (a), the effect of correlations in the permeability is barely visible. For $\xi = X$ (d), correlations of the permeability are apparent in the small site-to-site variations. These simulations were carried out on systems of $N_x = 240$ sites with $\Delta x = 0.5$ m. In (b), (c), and (d), the profile in (a) shown in gray to emphasize the contrasting scale and magnitude of permeability fluctuations as a function of the correlation length.

Ornstein-Uhlenbeck process [87]. Such a process is fully characterized by its mean (set to zero) and covariance function

$$\mathrm{Cov}(L(x), L(y)) = \sigma^2 e^{-|x-y|/\xi}. \tag{9}$$

Unless otherwise specified, we have set $\sigma = 0.5$ for the simulations presented in this work. More information about the Ornstein-Uhlenbeck process and a derivation of its covariance function can be found in Appendix E. For more detailed discussions, we refer to the original paper by Uhlenbeck and Ornstein [90], as well as Ref. [44]. The correlation length ξ sets the length scale of the variation in the permeability. The effect of the correlation length is illustrated in Fig. 2. For a correlation length equal to a few lattice spacings (Fig. 7(a)), the permeability is effectively random on neighboring sites, and so shows substantial fluctuations over small distances. As the correlation length increases to the system size (Fig. 7(b,c,d)), the site-to-site variations of the permeability are significantly diminished, as is the magnitude of the fluctuations through the system, though appreciable variations can still occur over larger distances.

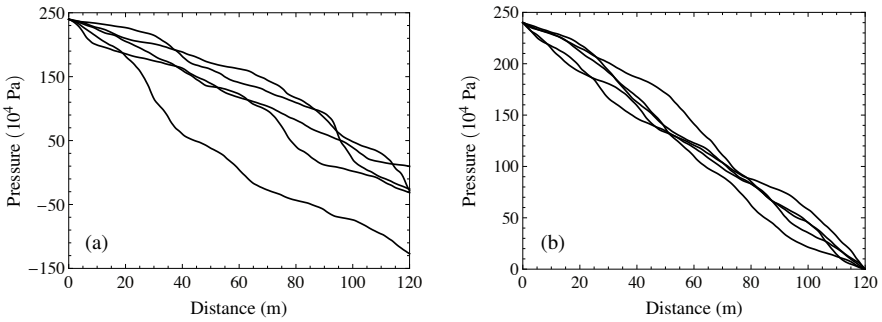

Figure 3: Pressure profiles with (a) Neumann and (b) Dirichlet boundary conditions for $\xi = 0.1X$. The simulations were carried out on systems of $N_x = 120$ sites with $\Delta x = 1$. Only pressure differences are meaningful; negative pressures are the result of a particular choice of a zero of pressure.

Examples of pressure trajectories under both types of boundary conditions are shown in Fig. 3. For both Neumann and Dirichlet boundary conditions the pressure decreases monotonically due to the resistance of the permeable medium. The difference is that, for DBC, the pressure is fixed at both ends of the system while, for NBC, the pressure is fixed only at entry (along with the production rate), so the exit pressure is a free variable. In particular, the distribution of pressures broadens along the system for NBC, but, for DBC, broadens initially, then narrows as the effect of the exit boundary takes hold.

3 FINITE-VOLUME METHOD IN ONE DIMENSION

3.1 GENERATION OF THE GAUSSIAN RANDOM FIELD

The statistics of pressure distributions in a one-dimensional permeable medium are given in terms of the permeability distribution by the solution (6) and (7) to Darcy's equation (1). In two and three dimensions, the corresponding solutions of (3) are divergence-free vector fields expressed as

$$K\nabla p = \nabla \times A, \tag{10}$$

where A is a vector potential. These do not yield the simple analytic forms of (6) and (7), so we must look to numerical solutions of (3) for each realization of the permeability, then average the results. In this section, we describe the numerical method for accomplishing this, which we will then apply to the one-dimensional Darcy equation (1).

The finite-volume method (FVM) is a discretization technique for partial differential equations, especially those associated with conservation laws, such as (3). The FVM uses a volume integral formulation based on a partition of the system into volumes to discretize the equations by representing their solution as a set of algebraic equations for quantities defined within each volume. Finite-volume methods are based on applying conservation principles over each of the small volumes in the partition, so global conservation is ensured. The FVM is an established technique, especially for computational fluid dynamics, but we provide a brief description here for completeness. For more background on the finite-volume method, see, for example, Refs [6, 18].

All simulations, both for the finite-volume method and the path integral, are carried out on a discrete lattice with $N_x + 2$ sites. An example with $N_x = 4$ is shown in Fig. 4.

Simulation of the pressure subject to Eq. (3) requires a permeability field $K(x)$. To obtain such a field, one first generates the log-permeability $L(x)$ and then invokes the relation $K(x) = e^{L(x)}$. Depending on the desired covariance structure, there are many different techniques to generate $L(x)$. We present two possibilities here.

For a representation of the log-permeability field $L(x)$, the first step is to generate an array U of length N_x of standard uniform ($\sim \mathcal{U}(0,1)$) random numbers. A good choice for this procedure is the Mersenne-Twister pseudo-

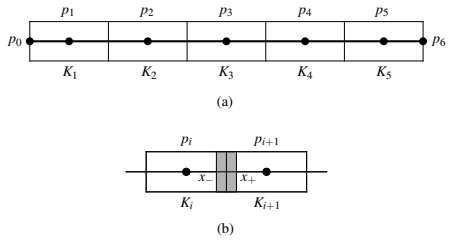

Figure 4: (a) Schematic depiction of a one-dimensional lattice partitioned into 5 cells with $N_x + 2 = 7$ sites according to the finite-volume method. The permeabilities K_i, for $i = 1, 2, 3, 4, 5$, are considered constant within each cell, and the pressures at the cell boundaries are determined from (40). (b) Section of the one-dimensional lattice with the integration region (shown shaded) used to derive the equation for the pressure.

random number generator [71]. It is freely available in a variety of coding languages. Various algorithms exist to transform the array U into an array S of standard normal ($\sim \mathcal{N}(0, 1)$) random numbers. Two examples of such algorithms are given in Appendix A. The array S, once available, must be transformed into an array of correlated random variables from the target distribution. One way to do this is to use the Cholesky decomposition of the covariance matrix C for L [80]. The Cholesky decomposition of a positive-definite, real, symmetric matrix (such as C) is the unique decomposition of the form: $C = DD^T$. The array L is then given by: $L = DS$. This type of calculation takes $\mathcal{O}(N_x^3)$ floating-point operations (or "flops") [80].

Another method, which is faster, but more complicated, is the so-called circulant embedding technique [45]. One embeds the correlation matrix C of the field $L(x)$ into a matrix S that has a circulant or block circulant structure. Products of the square roots $S^{1/2}$ with vectors of uncorrelated standard normal random numbers will then yield realizations of the desired field [27, 28]. The method relies on the fast Fourier transform (FFT). More details on the use fast Fourier transform in the generation of Gaussian random fields can be found in Ref. [66]. For an array containing N_x points, the computational requirements are those of an FFT of a vector of length $2N_x$ per realization [27], or $\mathcal{O}(2N_x \log 2N_x)$ flops. Our field-generating code is available online under Ref. [**code**].

3.2 CALCULATION OF THE DARCY PRESSURE

Once the permeability field has been determined, we can derive an equation for the pressure by integrating (3) over a small region near the boundary between the ith and $(i+1)$st cells (Fig. 8(b)):

$$\begin{aligned}\int_{x_-}^{x_+} \frac{d}{dx}\left(K\frac{dp}{dx}\right) dx \quad &= \left(K\tfrac{dp}{dx}\right)\Big|_{x_-} - \left(K\tfrac{dp}{dx}\right)\Big|_{x_+} \\ &= K_i(p-p_i) - K_{i+1}(p_{i+1}-p)\,, \end{aligned} \tag{11}$$

where p is the pressure at the boundary between the two cells and we have set the lattice spacing to one for simplicity. As there are no sources, the upper (resp. lower) limit of integration can be extended to the right (resp. left) edge of the system without affecting the value of the integral. Hence, the two terms on the right-hand side must each be equal to the same constant:

$$q_0 = -K_i(p-p_i) = K_{i+1}(p_{i+1}-p)\,. \tag{12}$$

Elimination of the boundary pressure p yields:

$$q_0 = -\frac{K_i K_{i+1}}{K_i + K_{i+1}}(p_{i+1}-p_i) \equiv -t_{i,i+1}(p_{i+1}-p_i)\,, \tag{13}$$

where we have defined the transmissibility $t_{i,i+1}$ as the harmonic mean of K_i and K_{i+1}. Under Dirichlet boundary conditions, we set $p_0 = P_i$ and $p_{N_x+1} = P_f$. Equation (3) translates into the set of linear equations:

$$\begin{pmatrix} t_{01}+t_{12} & -t_{12} & \ddots & 0 & 0 \\ -t_{12} & t_{12}+t_{23} & \ddots & 0 & 0 \\ \vdots & -t_{23} & \ddots & \vdots & \vdots \\ 0 & \vdots & \ddots & t_{N_x-2,N_x-1}+t_{N_x-1,N_x} & -t_{N_x-1,N_x} \\ 0 & 0 & \ddots & -t_{N_x-1,N_x} & t_{N_x-1,N_x}+t_{N_x,N_x+1} \end{pmatrix}$$

$$\times \begin{pmatrix} p_1 \\ p_2 \\ \vdots \\ \vdots \\ p_{N_x-1} \\ p_{N_x} \end{pmatrix} = \begin{pmatrix} t_{01}P_i \\ 0 \\ \vdots \\ \vdots \\ 0 \\ t_{N_x,N_x+1}P_f \end{pmatrix}$$

The transmissibility over the boundaries is computed by stipulating a constant flow rate over the boundary half-cell, which results in equations similar to Eqs. (12) and (13).

When working with Neumann boundary conditions, where q_0 is fixed, we set $p_0 = P_i$. We have to solve the sparse matrix equation:

$$\begin{pmatrix} t_{01} & 0 & \ddots & 0 & 0 & 0 \\ -t_{12} & t_{12} & \ddots & 0 & 0 & 0 \\ \vdots & \vdots & \ddots & \vdots & \vdots & \vdots \\ 0 & 0 & \ddots & -t_{N_x-1,N_x} & t_{N_x-1,N_x} & 0 \\ 0 & 0 & \ddots & 0 & -t_{N_x,N_x+1} & t_{N_x,N_{x+1}} \end{pmatrix} \times \begin{pmatrix} p_1 \\ p_2 \\ \vdots \\ \vdots \\ p_{N_x-1} \\ p_{N_x} \end{pmatrix} = \begin{pmatrix} t_{01}P_i + q_0 \\ q_0 \\ \vdots \\ \vdots \\ q_0 \\ q_0 \end{pmatrix}$$

The calculations were done with the sparse matrix solver UMFPACK [25], which can solve a sparse matrix equation in $\mathcal{O}(N_x \log N_x)$ flops.

4 PATH INTEGRAL FORMALISM

4.1 THE "PATH INTEGRAL" IDEA

Imagine a particle following some spatial trajectory $x(t)$, subject to initial condition $x(t_i) = x_i$ and final condition $x(t_f) = x_f$. The difference between the final time t_f and the initial time t_i is some amount of time T. In classical mechanics, Newtonian dynamics predicts the unique trajectory. In quantum mechanics and in the context of stochastic theory, motion is not constrained by Newton's laws. There is a variety of conceivable paths from x_i to x_f within time T. How does one associate a probability to the occurrence of each possible path?

Suppose one makes a large number of successive position measurements of a quantum particle, separated by a small time interval Δt. The position that results from a measurement at time t_j is denoted by x_j. The successive values x_1, x_2, x_3,... practically define a spatial trajectory $x(t)$. The probability density associated with a specific path materializes is a function of x_1, x_2, x_3,..., say $P(...,x_j,x_{j+1},...)$. By integrating $P(...,x_j,x_{j+1},...)$ over a spatial region, one obtains the probability that the path lies within that region. Thus, the probability that x_j lies between a_j and b_j, x_{j+1} lies between a_{j+1} and b_{j+1}, etc. is given by

$$... \int_{a_j}^{b_j} \int_{a_{j+1}}^{b_{j+1}} ...P(...x_j,x_{j+1},...)...dx_j\ dx_{j+1}... \tag{14}$$

To find the probability that the particle follows a path within some predefined region of space, one integrates over the contributions from each possible path in the region. Each contribution will be of type (14).

4.2 WIENER'S "CALCULATION OF THE PROBABILITY FOR A PATH"

In his 1922 paper [98] Norbert Wiener writes about a Brownian particle: Let us consider a particle free to wander along the X-axis. (...) It may then be

shown that the probability that after a time t it has wandered from the origin to a position lying between $x = x_1$ and $x = x_2$ is

$$\frac{1}{\sqrt{\pi c t}} \int_{x_1}^{x_2} \exp\left[-\frac{x^2}{ct}\right] \, dx, \tag{15}$$

where c is a constant which we may reduce to 1 by a proper choice of units." He introduces the concept of "particle histories" or "time-paths": "There are certain assemblages of time-paths to which we can immediately assign a measure, a probability. These assemblages are obtained by restricting the position of the particle at certain specified times, finite in number, to certain specified finite or infinite intervals. An example is the set of all time-paths $x = \Phi(t)$, such that

$$\begin{aligned} &x_{11} \leqslant \Phi(t_1) \leqslant x_{12} \\ &x_{21} \leqslant \Phi(t_2) \leqslant x_{22} \\ &\ldots \\ &x_{n1} \leqslant \Phi(t_n) \leqslant x_{n2} \\ (0 \leqslant &t_1 \leqslant t_2 \leqslant \ldots \leqslant t_n \leqslant 1.) \end{aligned} \tag{16}$$

This assemblage of time-paths may be considered as possessing the compound probability that after a time t, the particle shall occupy a position between x_{11} and x_{21}, that by time t_2 it shall have wandered from whatever position it shall have occupied at time t_1 to a position between x_{21} and x_{22}, and so on. By (15), this compound probability is

$$\begin{aligned} &\frac{1}{\sqrt{\pi^n t_1 (t_2 - t_1)(t_3 - t_2)\ldots(t_n - t_{n-1})}} \\ &\times \int_{x_{11}}^{x_{12}} \int_{x_{21}}^{x_{22}} \ldots \int_{x_{n1}}^{x_{n2}} \exp\left[-\frac{\xi_1^2}{t_1} + \frac{(\xi_2 - \xi_1)^2}{(t_2 - t_1)} + \ldots + \frac{(\xi_n - \xi_{n-1})^2}{(t_n - t_{n-1})}\right] \\ &\times \, d\xi_1 \, d\xi_2 \, \cdots d\xi_n." \end{aligned} \tag{17}$$

Each negative of an exponential in Eq. (17) is known as a "Lagrangian". The Gaussian weight attached to each event follows from the definition of Brownian motion. Alternatively, it can be inferred from the solution to the diffusion equation, or the Fokker-Planck equation for Brownian motion:

$$\frac{\partial \psi}{\partial t} = D \frac{\partial^2 \psi}{\partial x^2}, \tag{18}$$

where ψ is the probability density of the particle's position and, in Wiener's units, $D = 1$.

In the continuum limit $N \to \infty$, $\Delta t \to 0$, such that the product $N\Delta t$ remains fixed, one obtains for Eq. (17) (up to a normalization factor):

$$\int_{x_{11}}^{x_{12}} \dots \int_{x_{n1}}^{x_{n2}} \prod_{t=0}^{T} d\xi(t) \exp\left[-\int_0^T \left(\frac{d\xi}{dt}\right)^2 dt\right] \equiv \int \mathcal{D}\xi(t) \exp\left[-\int_0^T \left(\frac{d\xi}{dt}\right)^2 dt\right]. \tag{19}$$

We can use equation (17) to calculate the average value of any functional of the trajectories:

$$\langle (F\{\xi(t)\}\rangle \propto \int_{-\infty}^{\infty} \dots \int_{-\infty}^{\infty} F\{\xi(t)\} \exp\left\{-\int_0^T \left[\frac{d\xi(t)}{dt}\right]^2 dt\right\} \prod_0^t d\xi(t) \equiv \int F\{\xi(t)\} d_w\xi, \tag{20}$$

where we have taken the limit as the time intervals go to zero in Eq. (17) to define a probability measure d_w. In particular, we are often interested in covariance functions. The covariance function

$$\begin{aligned} \langle \xi(t_1)x(t_1)\rangle =& \frac{1}{\mathcal{Z}} \int \mathcal{D}\xi(t)\xi(t_1)\xi(t_2) \exp\left[-\int_0^T \left(\frac{d\xi}{dt}\right)^2 dt\right]; \\ \mathcal{Z} =& \int \mathcal{D}\xi(t) \exp\left[-\int_0^T \left(\frac{d\xi}{dt}\right)^2 dt\right] \end{aligned} \tag{21}$$

is derived by adding a source term to the continuous version of the Lagrangian. For a fuller explanation of the use of functional integration to calculate covariance functions, see Appendix B. Formally, Eq. (21) satisfies the definition of a Green function for the diffusion equation. To underline the natural applicability of the path integral formalism to the stochastic problem of Darcy flow, we have shown that the path integral can be seen as a stochastic integral in Appendix C.

4.3 DERIVATION OF THE PATH INTEGRAL FOR DARCY FLOW

In this Section, we formulate the solution to Eq. (4) as a path integral. The path integral for Darcy's law is derived with methods used in classical statistical dynamics [31, 57, 58, 79]. A one-dimensional system of length X is divided into N_x segments of length Δx. The pressure is defined at $0, (i-\frac{1}{2})\Delta x$, for $i = 1, 2, \dots N_x$, and X, so a stochastic pressure path through the system

is $(p_0, p_1, \ldots, p_{N_x}, p_{N_x+1})$ (see Fig. 4). The discrete form of Darcy's law (4) on this lattice is (cf. Eq. (12))

$$\frac{p_i - p_{i-1}}{\Delta x} = -q_0 e^{-L_i}. \tag{22}$$

Here, $K_i = e^{-L_i}$ is the permeability at the i^{th} grid point. The choice $\mathbb{E}[L_i] = 0$ implies $\mathbb{E}[K_i] = 1$: the so-called geometric mean of the permeability equals 1.

The stochastic generating functional for correlation functions of the pressure at fixed log-permeability is

$$Z_L(\{u_i\}) = \int \prod_i dp_i \exp\left(\sum_i u_i p_i\right) \delta\left(\frac{p_i - p_{i-1}}{\Delta x} + q_0 e^{-L_i}\right). \tag{23}$$

For detailed background information on stochastic generating functions, see Ref. [105]. The Jacobian $J = (\Delta x)^{-N}$ that arises from factor $\frac{p_i - p_{i-1}}{\Delta x}$ inside the δ-functional [79], has been omitted. Although J becomes infinite as $\Delta x \to 0$, this quantity is cancelled by the same divergence in expressions for averages. Taking the average of Z_L over the probability density of the log-permeability yields the generating function for pressure correlations:

$$Z(\{u_i\}) = \int \prod_i dL_i P(\{L_i\}) Z_L(\{u_i\}) e^{-\sum_i L_i} \tag{24}$$

The factor q_0 in the Jacobian $q_0 \exp(-\sum_i L_i)$ has been omitted. The log-permeabilities are taken to follow a correlated Gaussian distribution:

$$P(\{L_i\}) = \frac{1}{(2\pi)^{N/2} |C_L|^{1/2}} \exp\left[-\sum_{ij} L_i (C_L^{-1})_{ij} L_j\right], \tag{25}$$

where C_L is the correlation matrix and $|C_L|$ its determinant. Substituting (23) and (25) into (24) and again omitting constant prefactors,

$$\begin{aligned} Z(\{u_i\}) = &\int \prod_i dp_i \int \prod_i dL_i \exp\left(\sum_i u_i p_i\right) \\ &\times \exp\left[-\sum_{ij} L_i (C_L^{-1})_{ij} L_j\right] \exp\left[-\sum_i L_i\right] \\ &\times \delta\left(\frac{p_i - p_{i-1}}{\Delta x} + q_0 e^{-L_i}\right), \end{aligned} \tag{26}$$

and integrating over the L_i, yields a path integral for the probability density Q of the pressures:

$$Q(\{p_i\}) = \frac{e^{-S(\{p_i\})}}{Z}, \tag{27}$$

where

$$Z = \int \prod_i dp_i e^{-S(\{p_i\})}, \tag{28}$$

with the discrete "action"

$$\begin{aligned} S(\{p_i\}) &= \sum_i \log\left(\frac{p_{i-1} - p_i}{q_0 \Delta x}\right) \\ &+ \sum_{ij} \log\left(\frac{p_{i-1} - p_i}{q_0 \Delta x}\right) (C_L^{-1})_{ij} \log\left(\frac{p_{j-1} - p_j}{q_0 \Delta x}\right). \end{aligned} \tag{29}$$

Averages over pressure are determined by integrals over Q. For example, the average $\langle p_k \rangle$ of the pressure p_k at the kth lattice point is

$$\langle p_k \rangle = \frac{1}{Z} \int \prod_i dp_i \, p_k \, e^{-S(\{p_i\})}, \tag{30}$$

which confirms the cancellation of the omitted factors. Higher-order correlation functions and cumulants are calculated analogously.

5 USER'S GUIDE TO EVALUATING PATH INTEGRALS

This Chapter provides a user's guide to the calculation of path integrals on a lattice, with the quantum harmonic oscillator as an example. We will focus on trajectories $x(t)$ in one spatial dimension. The time t is described by a lattice and takes discrete values. This toy model has the advantage of having an exact solution, which enables the verification of the methodology.

5.1 THEORETICAL BACKGROUND OF THE QUANTUM HARMONIC OSCILLATOR

The solution to the initial-value problem of the Schrödinger equation,

$$i\hbar\frac{\partial\psi}{\partial t} = \hat{H}\psi\,, \tag{31}$$

can be written as

$$\psi(x,t) = e^{-i\hat{H}t/\hbar}\psi(x,0)\,, \tag{32}$$

where the exponential factor is known as the "evolution operator". The exponential of an operator $\hat{O}$ is defined by the Taylor series of the exponential function:

$$e^{\hat{O}} = \sum_{n=0}^{\infty}\frac{\hat{O}^n}{n!}\,. \tag{33}$$

Equation (32) is only a formal solution to Eq. (31) because obtaining an explicit solution from the evolution operator is no simpler than solving the original equation.

The connection between the evolution operator and Feynman's path integral can be made by considering the matrix elements of the evolution operator between any two initial and final position eigenstates. In Dirac's bra-ket notation [95]

$$\langle x_f|e^{-i\hat{H}(t_f-t_i)/\hbar}|x_i\rangle = \langle x_f,t_f|x_i,t_i\rangle\,. \tag{34}$$

These matrix elements embody all the information about how a system with the Hamiltonian $\hat{H}$ evolves, or propagates, in time, and is known as the "propagator". In particular, the evolution of the wave function is given by

$$\psi(x_f, t_f) = \langle x_f, t_f|\psi\rangle \tag{35}$$
$$= \int \langle x_f, t_f|x_i, t_i\rangle\langle x_i, t_i|\psi\rangle \, dx_i \tag{36}$$
$$= \int \langle x_f, t_f|x_i, t_i\rangle\psi(x_i, t_i) \, dx_i \,, \tag{37}$$

which shows that the propagator (34) is a type of Green function known as the fundamental solution of Eq. (31).

5.1.1 Derivation of the path integral

The standard derivation of the path integral from the evolution operator considers the evolution of a system over a short time Δt. The method can be demonstrated for the Hamiltonian

$$\hat{H} = \frac{\hat{p}^2}{2m} + V(\hat{x}) \,, \tag{38}$$

of a particle of mass m moving in a potential V, where $\hat{p}$ and $\hat{x}$ signify momentum and position operators.

The propagator to be evaluated is

$$\langle x_f, t_i + \Delta t|x_i, t_i\rangle = \langle x_f|e^{-i\hat{H}\Delta t/\hbar}|x_i\rangle \tag{39}$$
$$= \int \langle x_f|p\rangle\langle p|e^{-i\hat{H}\Delta t/\hbar}|x_i\rangle \, dp \,. \tag{40}$$

We expand the exponential to first order in Δt:

$$\langle p|e^{-i\hat{H}\Delta t/\hbar}|x_i\rangle = \left\langle p \left| 1 - \frac{i\hat{H}\Delta t}{\hbar} + \mathcal{O}(\Delta t)^2 \right| x_i \right\rangle . \tag{41}$$

The explicit mention of $\mathcal{O}(\Delta t)^2$ corrections will be henceforth omitted.

For the Hamiltonian in Eq. (38) the matrix elements of the operators on the right-hand side of Eq. (41) are evaluated using

$$\langle p|1|x_i\rangle = \langle p|x_i\rangle \tag{42}$$
$$\langle p|\hat{p}^2|x_i\rangle = \langle p|\hat{p}^2|p\rangle\langle p|x_i\rangle = p^2\langle p|x_i\rangle \tag{43}$$
$$\langle p|V(\hat{x})|x_i\rangle = \langle p|x_i\rangle\langle x_i|V(\hat{x})|x_i\rangle = V(x_i)\langle p|x_i\rangle \,. \tag{44}$$

The short-time propagator in Eq. (41) can now be approximated as

$$\langle p|e^{-i\hat{H}\Delta t/\hbar}|x_i\rangle \approx \left[1 - \frac{ip^2\Delta t}{2m\hbar} - \frac{i\Delta t}{\hbar}V(x_i)\right]\langle p|x_i\rangle \tag{45}$$

$$\approx \exp\left\{-\frac{i}{\hbar}\left[\frac{p^2\Delta t}{2m} + V(x_i)\Delta t\right]\right\}\langle p|x_i\rangle\,, \tag{46}$$

with the approximations becoming equalities for infinitesimal Δt. We use

$$\langle p|x\rangle = \frac{e^{-ipx/\hbar}}{\sqrt{2\pi\hbar}}\,, \tag{47}$$

to obtain

$$\langle p|e^{-i\hat{H}\Delta t/\hbar}|x_i\rangle = \frac{1}{\sqrt{2\pi\hbar}}\exp\left\{-\frac{i}{\hbar}\left[px_i + \frac{p^2\Delta t}{2m} + V(x_i)\Delta t\right]\right\}. \tag{48}$$

We return to the right-hand side of Eq. (40) and invoke Eq. (47) to find,

$$\langle x_f, t_i + \Delta t|x_i, t_i\rangle = \int \frac{dp}{2\pi\hbar}\exp\left\{-\frac{i\Delta t}{\hbar}\left[\frac{p(x_i - x_f)}{\Delta t} + \frac{p^2}{2m} + V(x_i)\right]\right\} \tag{49}$$

$$= \sqrt{\frac{m}{2\pi i\hbar\Delta t}}\exp\left\{\frac{i}{\hbar}\left[\frac{m(x_f - x_i)^2}{2\Delta t} - V(x_i)\Delta t\right]\right\}. \tag{50}$$

The integral has been evaluated by completing the square in the argument of the exponential. If we make the identification

$$\left(\frac{dx}{dt}\right)^2 = \left(\frac{x_f - x_i}{\Delta t}\right)^2\,, \tag{51}$$

we see that the argument of the exponential on the right-hand side of Eq. (50) is the product of Δt and the classical Lagrangian L:

$$L\,\Delta t = \left[\frac{m}{2}\left(\frac{x_f - x_i}{\Delta t}\right)^2 - V(x_i)\right]\Delta t\,. \tag{52}$$

Hence, the short-time propagator reduces to

$$\langle x_f, t_i + \Delta t|x_i, t_i\rangle = \sqrt{\frac{m}{2\pi i\hbar\Delta t}}\,e^{iL\Delta t/\hbar}\,. \tag{53}$$

We can now evaluate propagators over finite times by dividing the time interval into slices of duration Δt,

$$\begin{aligned}\langle x_f, t_f | x_i, t_i \rangle = &\iint \cdots \int \langle x_f, t_f | x_{N-1}, t_{N-1} \rangle \\ &\times \langle x_{N-1}, t_{N-1} | x_{N-2}, t_{N-2} \rangle \cdots \langle x_2, t_2 | x_1, t_1 \rangle \\ &\times \langle x_1, t_1 | x_i, t_i \rangle \, dx_1 \, dx_2 \cdots dx_{N-1} \,,\end{aligned} \tag{54}$$

and applying Eq. (53) to each slice:

$$\langle x_f, t_f | x_i, t_i \rangle = \int \prod_{n=1}^{N-1} dx_n \exp\left[\frac{i\Delta t}{\hbar} \sum_{n=1}^{N-1} L(t_n)\right] . \tag{55}$$

We have omitted the prefactors in Eq. (55) because they will not be needed in the following.

In the continuum limit ($N \to \infty$, $\Delta t \to 0$, such that the product $N\Delta t$ is fixed), the integral over positions at each time is the same as the integral over all paths between the initial and final positions:

$$\langle x_f, t_f | x_i, t_i \rangle = \int Dx(t) \, e^{-iS/\hbar} \,, \tag{56}$$

where $Dx(t) \equiv \prod_{n=1}^{N-1} dx_i$ and, as $N \to \infty$, the action S of the path $x(t)$ becomes

$$S = \int_{t_i}^{t_f} L(x(t)) \, dt = \int_{t_i}^{t_f} \left[\frac{m}{2}\left(\frac{dx}{dt}\right)^2 - V(x(t))\right] dt \,. \tag{57}$$

5.1.2 Imaginary time path integrals

The path integral in Eqs. (56) and (57) yields transition amplitudes as the sum of the phases of all paths between the given initial and final positions. For our purposes imaginary time path integrals, where the time t is replaced by $-i\tau$, with τ real, are of primary interest.

There are two main applications of imaginary time path integrals. In statistical mechanics $\tau = \hbar/(k_B T)$, where k_B is Boltzmann's constant and T is the absolute temperature. Thus, for equal initial and final positions x, an integration over x produces the partition function Z:

$$Z = \int \langle x | e^{-\hat{H}\tau/\hbar} | x \rangle \, dx = \mathrm{Tr}\left(e^{-\hat{H}\tau/\hbar}\right) , \tag{58}$$

in which the trace Tr is the sum/integral of the diagonal elements of an operator.

Another application is the determination of the energy spectrum of a quantum system. This calculation utilizes the identity $1 = \sum_n |n\rangle\langle n|$ in terms of the eigenfunctions of the Hamiltonian, such that $\hat{H}|n\rangle = E_n|n\rangle$,

$$Z = \int \langle x|e^{-\hat{H}\tau/\hbar}|x\rangle \, dx = \int \sum_n \langle x|e^{-\hat{H}\tau/\hbar}|n\rangle\langle n|x\rangle \, dx \tag{59}$$

$$= \int \sum_n e^{-E_n\tau/\hbar}\psi_n(x)\bar{\psi}_n(x)dx = \sum_n e^{-E_n\tau/\hbar}, \tag{60}$$

where we have used the fact that $\psi_n(x)$ is normalized. Similarly, we can expand the propagator $\langle x_f, t_f|x_i, t_i\rangle$ in terms of the eigenfunctions $\{|n\rangle\}$:

$$\langle x_f, t_f|x_i, t_i\rangle = \sum_{n=0}^{\infty} e^{-E_n(t_f-t_i)/\hbar}\langle x_f|n\rangle\langle n|x_i\rangle. \tag{61}$$

The derivation of the imaginary-time path integral proceeds along the same lines as the real-time propagator, with the result corresponding to Eq. (50) given by

$$\langle x_f|e^{-\hat{H}\Delta\tau/\hbar}|x_i\rangle = \sqrt{\frac{m}{2\pi\hbar\Delta\tau}} \exp\left\{-\frac{\Delta\tau}{\hbar}\left[\frac{m}{2}\left(\frac{x_f - x_i}{\Delta\tau}\right)^2 + V(x_i)\right]\right\}, \tag{62}$$

In the limit $N \to \infty$, Eq. (62) can be used to write the partition function in a form analogous to Eqs. (56) and (57):

$$Z = \mathrm{Tr}\left(e^{-\hat{H}(\tau_f-\tau_i)/\hbar}\right) = \int Dx(\tau)\, e^{-S/\hbar}, \tag{63}$$

where S is the (Euclidean) action over a path $x(\tau)$ with $\tau_f \geqslant \tau \geqslant \tau_i$, and $x(\tau_f) = x_f$, $x(\tau_i) = x_i$.

$$S = \int_{\tau_i}^{\tau_f} L(x(\tau))\, d\tau = \int_{\tau_i}^{\tau_f} \left[\frac{m}{2}\left(\frac{dx}{d\tau}\right)^2 + V(x(\tau))\right] d\tau. \tag{64}$$

The integrals in Eqs. (63) and (64) and their real-time counterparts in Eqs. (56) and (57) are over all paths weighted by Lagrangian-type quantities. However, in the imaginary-time formalism, quantities associated with the paths are real.

5.1.3 The quantum harmonic oscillator

The Hamiltonian for a particle of mass m bound by a harmonic potential with force constant k is

$$\hat{H} = \frac{\hat{p}^2}{2m} + \frac{k\hat{x}^2}{2} = \frac{\hat{p}^2}{2m} + \frac{m\omega^2\hat{x}^2}{2}, \tag{65}$$

where $\omega = \sqrt{k/m}$ is the natural frequency of the oscillator. The discretized Euclidean Lagrangian for this system is

$$L_i = \left[\frac{m}{2}\left(\frac{x_{i+1} - x_i}{\Delta\tau}\right)^2 + \frac{m\omega^2 x_i^2}{2}\right]\delta\tau, \tag{66}$$

which allows us to express the Euclidean action and the partition function as

$$S = \sum_{n=1}^{N-1} L_i \tag{67}$$

$$Z = \int_{-\infty}^{\infty} \prod_{i=1}^{N-1} dx(\tau_i) \exp\left(-\frac{\Delta\tau}{\hbar} S\right). \tag{68}$$

The energy eigenvalues of $\hat{H}$ are $E_n = \hbar\omega(n + \frac{1}{2})$ for $n = 0, 1, 2, \ldots$. The normalized ground state wave function is

$$\psi_0 = \left(\frac{m\omega}{\pi\hbar}\right)^{\frac{1}{4}} \exp\left(-\frac{m\omega x^2}{2\hbar}\right), \tag{69}$$

from which all other wave functions can be obtained through ladder operations. Expectations of observable quantities in the ground state are determined by $\psi_0(x)$.

5.2 COMPUTATIONAL METHOD

The formalism discussed in Sec. 5.1 will be applied to the harmonic oscillator. However, the range of applicability is much broader. The idea is that if the partition function can be constructed ("if the system can be simulated"), an arbitrary observable can be determined ("measured") with a statistical uncertainty that decreases as the simulation is extended. For the construction of such observables and their evaluation the complete tool set of statistical mechanics can be used. An overview of all parameters and their meanings is given in Table 1.

5.2.1 Monte Carlo methods

The simulation is done on a discrete time lattice with N_τ time slices with periodic boundary conditions so that the time slice $N_\tau + 1$ equals the time slice 1. To calculate the statistics of the observables, many particle trajectories of the form $(x_1, \ldots, x_{N_\tau})$ are needed, where each coordinate is a real number. Starting from an initial, thermalized configuration path$^{(0)}$ (see Sec. 5.2.4), the path is updated by the Metropolis–Hastings algorithm. The application of

Parameter	Meaning
N_τ	number of elements of the time lattice
$i\Delta\tau$	Euclidean time, with $i \in \{1, \ldots, N_\tau\}$ the site index
t_{MC}	Monte Carlo time; refers to index of a path in the Markov chain
sweep	N_τ applications of the single-site Metropolis–Hastings algorithm
$N_{sep} - 1$	number of discarded paths between successive paths used for measurement
$\Delta\tau$	lattice spacing
$\tilde{m}$	dimensionless effective mass: $\tilde{m} = m\Delta\tau$
$\tilde{\omega}$	dimensionless frequency: $\tilde{\omega} = \omega\Delta\tau$
N	number of paths within an ensemble
ξ	"correlation time": Euclidean time for two-point correlations to diminish by a factor e
m_{eff}	effective mass: $m_{eff} = 1/\xi$
N_B	number of bins in jackknife procedure
B	bin width $B = N/N_B$
$\tau_{O,exp\,/int}$	exponential and integrated autocorrelation time of observable O

Table 1: An overview of all parameters used in the context of the harmonic oscillator, and their meanings.

this elementary update to the variable x_i for each time slice i constitutes one "sweep" or one Monte Carlo step per site. One Metropolis sweep yields the next path in the sequence, e.g., $\text{path}^{(1)}$ from $\text{path}^{(0)}$. Because $\text{path}^{(\nu)}$ relies only on $\text{path}^{(\nu-1)}$, the trajectories constitute a Markov chain. The computational method is illustrated in Fig. 5. We distinguish between Euclidean time $\tau = i\Delta\tau$, which indicates the index i of a lattice site, and Monte Carlo time, which refers to the index of a path ν in the Markov chain. Because each path in the chain is based on the previous path, the paths are correlated. We will discuss these correlations in more detail in Sec. V. To combat the autocorrelation, we discard a number $N_{sep} - 1$ of paths between every two paths used for measurements. We will refer to the remaining paths used to calculate average quantities as "configurations."

5.2.2 Dimensionless variables and observables

Because computer code can handle only pure numbers, it is necessary to express the physics of the system in dimensionless form. A naive way of doing this is by expressing all quantities in metric units, e.g., meters. A disadvantage of this choice is that it leads to numbers that often span several orders of magnitude. To avoid this problem, we express all variables in

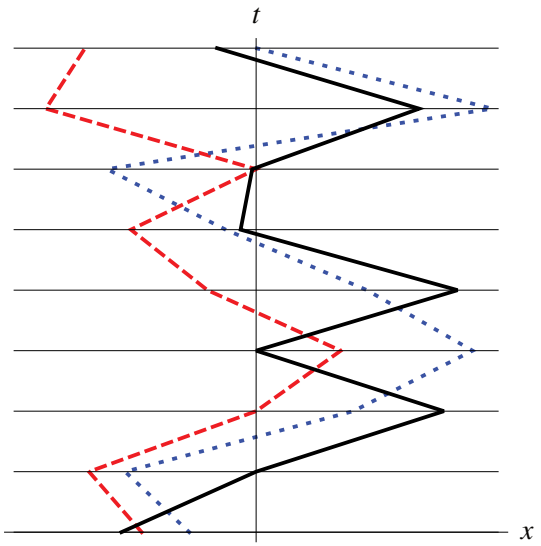

Figure 5: Illustration of the computational method. The spatial location of the particle at time τ_i, where $i = 1, \ldots, N_\tau = 8$, can take any real value, but is constrained by the potential centered at the origin and its neighboring positions at times τ_{i-1} and τ_{i+1}. The solid line represents the thermalized path$^{(0)}$; the dotted line is the next path in the Markov chain, path$^{(1)}$; and the dashed line is the resulting trajectory after 19 further Metropolis sweeps.

terms of the appropriate power of the lattice spacing $\Delta\tau$. To this end, we set $\hbar = 1 = c$, which implies that [time] = [length] = [mass^{-1}] = [energy^{-1}]. We introduce the dimensionless variables:

$$\tilde{m} = m\Delta\tau, \quad \tilde{\omega} = \omega\Delta\tau, \quad \tilde{x}_i = \frac{x_i}{\Delta\tau}, \tag{70}$$

The dimensionless action becomes

$$\tilde{S} = \sum_{i=1}^{N_\tau} \frac{1}{2}\tilde{m}(\tilde{x}_{i+1} - \tilde{x}_i)^2 + \frac{1}{2}\tilde{m}\tilde{\omega}^2\tilde{x}_i^2, \tag{71}$$

where $\tilde{m}$, $\tilde{\omega}$ and $\{\tilde{x}_i\}$ are dimensionless. Note that the summation range differs from the one in Eq. (68), due to periodic boundary conditions. We restrict ourselves to the subspace $\tilde{m} = \tilde{\omega}$ of the available parameter space. The parameter $\tilde{m}$ can thus be viewed as the effective lattice spacing of a harmonic oscillator with unit mass and unit natural frequency.

The continuum limit applies to observables and is not taken for an individual simulation. Rather, we run a series of simulations, each with a smaller effective lattice spacing (that is, a smaller value of $\tilde{m}$) and a greater value of N_τ than the previous, such that the product $N_\tau\tilde{m}$ is fixed.

For a quadratic action, all odd moments of $\hat{x}$ have zero expectation value. An analytic expression for $\langle \hat{x}^2 \rangle$ is derived in Ref. [23]:

$$\langle \hat{x}^2 \rangle = \frac{1}{2\tilde{m}\tilde{\omega}\sqrt{1+\frac{1}{4}\tilde{\omega}^2}} \left(\frac{1+R^{N_\tau}}{1-R^{N_\tau}} \right), \tag{72}$$

with the auxiliary variable

$$R = 1 + \frac{\tilde{\omega}^2}{2} - \tilde{\omega}\sqrt{1+\frac{\tilde{\omega}^2}{4}}. \tag{73}$$

The other observable we need is

$$\langle \hat{x}^4 \rangle = \frac{3}{(2\tilde{m}\tilde{\omega})^2(1+\frac{1}{4}\tilde{\omega}^2)} \left(\frac{1+R^{N_\tau}}{1-R^{N_\tau}} \right)^2 = 3\langle \hat{x}^2 \rangle^2. \tag{74}$$

Derivations of the expressions for Eqs. (72) and (74) are given in Ref. [95].

5.2.3 The Metropolis update

The core of our path-generating algorithm is an update of a single site based on the Metropolis-Hastings (MH) algorithm [50, 72]. The output is a set of N paths $\{\tilde{x}_1, \ldots, \tilde{x}_{N_\tau}\}$ with Boltzmann weights $\rho[\{\tilde{x}_i\}] \sim \exp[-\tilde{S}[\{\tilde{x}_i\}]]$. The input of the Metropolis update is an array path with N_τ sites, a real number h, and the parameters $\tilde{m}$ and $\tilde{\omega}$. Periodic boundary conditions avoid the need to abandon (in the data) sites affected by the lattice edges. One sweep visits N_τ sites in random order. A site may be visited repeatedly or not at all, but the mean number of visits per sweep for each site is one. Each Metropolis update to a given site consists of four steps.

1. Generate a random number u from a uniform distribution in the interval $[-h, h]$.
2. Propose a change to the visited site, $\tilde{x}_i \to \tilde{x}_i' = \tilde{x}_i + u$.
3. Compute the change in the action $\Delta\tilde{S}$ as a result of this trial modification.
4. Accept the change with probability $\min\{1, e^{-\Delta\tilde{S}}\}$.

Pseudocode is provided in Appendix D. The probability $\min\{1, e^{-\Delta\tilde{S}}\}$ in step 4 implies that proposed modifications that lower the action are always accepted. A trial that would increase the action is accepted with probability $e^{-\Delta\tilde{S}}$. This decision is made in an accept/reject step. The Metropolis update satisfies detailed balance [74]:

$$p(\tilde{x}_i \to \tilde{x}_i') e^{-\tilde{S}(\tilde{x}_i)} = p(\tilde{x}_i' \to \tilde{x}_i) e^{-\tilde{S}(\tilde{x}_i')}. \tag{75}$$

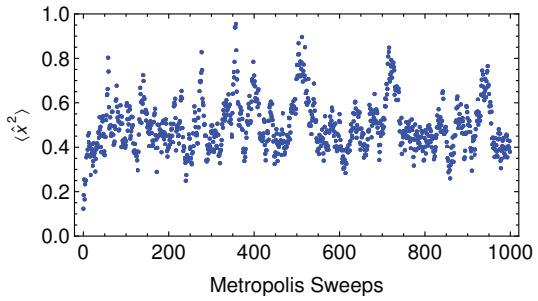

Figure 6: A trial run for $\langle \hat{x}^2 \rangle$ to illustrate thermalization effects ($\tilde{m} = \tilde{\omega} = 0.1$, $N_\tau = 1200$). One thousand paths were discarded between every two configurations whose output is shown. The first 50-100 configurations should not be used for measurements.

Because of this property, the estimated average of an observable $\hat{O}$ reduces to an arithmetic average. After one sweep, the acceptance ratio is computed. The value of h is adjusted to meet a predefined acceptance ratio. We chose the desired acceptance ratio to be 0.8 (which is a conventional choice in lattice QCD), even though we suspect the ideal value for the harmonic oscillator, with the choices of $\tilde{m} = \tilde{\omega}$ listed in Table II, to be smaller. Although algorithms with too low or too high an acceptance ratio are less efficient, the generated Boltzmann distribution of paths is unaffected by this choice.

5.2.4 Thermalization

The required thermalization process can start from an array of zeros (a "cold" start), random numbers (a "hot" start), or an initial path that is expected to be close to a thermalized path. The initial thermalization steps are not characteristic of the probability density $\rho[\{\tilde{x}_i\}] \sim \exp[-\tilde{S}\{\tilde{x}_i\}]$ and must be discarded lest they skew the simulation. A trial run is one way to choose the number of sweeps needed before the array qualifies as a thermalized path. An example of a thermalization process is given in Fig. 6. For each configuration, the observable $\langle \hat{x}^2 \rangle$ was measured to monitor its fluctuations around the expected values [1]. In our code we first average $\tilde{x}_i^2$ over the N_τ time slices in a given configuration, and then compute the ensemble average of that number over the configurations. For actions for which the exact answer is not known, independent "hot" and "cold" runs can help to establish the expectation value. In this case, the first 50-100 configurations should not be used.

1 Different observables can approach their equilibrium values at different rates.

5.2.5 Two-point correlation function

To make optimal use of CPU time, it is important to choose the number of sites N_τ as small as possible, but large enough to avoid finite-size effects. How is the lower bound on N_τ established? Correlations within a lattice are quantified by the connected two-point function:

$$G(\Delta\tau) = \langle x(\tau)x(\tau+\Delta\tau)\rangle - \langle x(\tau)\rangle \langle x(\tau+\Delta\tau)\rangle\,, \tag{76}$$

where we have written $x(\tau)$ instead of x_i to emphasize the dependence of G on the time difference $\Delta\tau$, where τ and $\Delta\tau$ can be any multiple of the lattice spacing. Because $\langle x(\tau)\rangle = 0$ for all τ for the harmonic oscillator, we work with the two-point function

$$G(\Delta\tau) = \langle x(\tau)x(\tau+\Delta\tau)\rangle \tag{77}$$

$$= \frac{1}{N_\tau}\sum_{i=1}^{N_\tau} \sum_{\substack{j \\ (j-i)\bmod N_\tau = \Delta\tau}} x(i)x(j). \tag{78}$$

An example of the exponential decay of $G(\Delta\tau)$ is shown in Fig. 7(a) [42],

$$G(\Delta\tau) = Ae^{-\Delta\tau/\xi} + Ae^{-(T-\Delta\tau)/\xi}, \tag{79}$$

where ξ is the correlation time and T is the final time. The second term in Eq. (79) is due to periodic boundary conditions. The total length of the lattice must be greater than ξ. We choose N_τ to be about $10\tilde{\xi}$ (where $\tilde{\xi}$ is the correlation time expressed in lattice units).

An estimate of $1/\tilde{\xi}$ can be obtained from the local logarithmic slope for suitable $\Delta\tau$ [42] [2]:

$$\frac{1}{\tilde{\xi}} = \frac{1}{2}\log\left[\frac{G(\Delta\tau-1)}{G(\Delta\tau+1)}\right]. \tag{80}$$

The quantity $1/\xi$ is known as the effective mass m_{eff}. Figure 7(b) shows $\tilde{m}_{\text{eff}}$ for the same set of paths used for Fig. 7(a).

Figure 8 suggests that there is a power-law dependence of $\tilde{\xi}$ on the effective lattice spacing. To construct Fig. 8, we repeated the procedure illustrated in Fig. 7 for 13 effective lattice spacings listed in Table 3. The physical length, the product of $\tilde{m} = \tilde{\omega}$ and N_τ, was kept constant. With this choice of parameters, we were able to explore two orders of magnitude in the lattice spacing; the associated N_τ are round numbers.

2 The logarithmic slope can also be determined less locally, as long as one stays within the range for which Eq. (79) holds.

$\tilde{m} = \tilde{\omega}$	N_τ	$\tilde{m} = \tilde{\omega}$	N_τ
1	120	0.1	1200
0.8	150	0.08	1500
0.6	200	0.06	2000
0.5	240	0.05	2400
0.3	400	0.03	4000
0.2	600	0.02	6000
		0.01	12000

Table 2: Effective lattice spacings used for the results shown in Figs. 4–8.

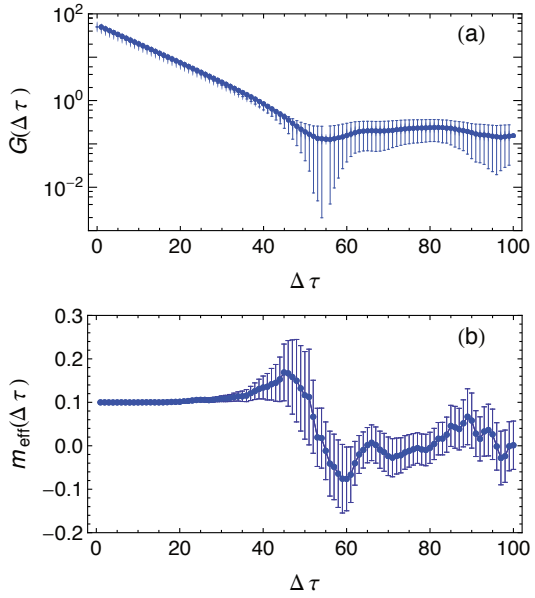

Figure 7: (a) The symmetrized two-point correlation function ($N_\tau = 1200$, $\tilde{m} = \tilde{\omega} = 0.1$, $N = 10^4$). The exponential decrease is swamped by noise after approximately 40 time slices and the magnitude of the error bars starts to increase significantly, and eventually the error bars become unreliable. (b) The effective mass $1/\tilde{\xi}$. The estimates of the errors are reliable until $\Delta\tau \approx 40$. If the error on the error had started to increase at some $\Delta t^* < 40$, Δt^* would have determined the cutoff for this parameter set.

5.3 JACKKNIFE ANALYSIS

Suppose we compute values $O_1, \ldots, O_N$, of an observable $\hat{O}$ (typically a moment of $\hat{x}$), with the expectation value and variance:

$$\langle \hat{O} \rangle = \langle O \rangle \tag{81}$$

$$\langle (\hat{O} - \langle \hat{O} \rangle)^2 \rangle = \sigma_O^2 \,. \tag{82}$$

The quantity $E(O)$ provides an unbiased estimator of the mean:

$$E(O) = E_N(O) = \frac{1}{N} \sum_{i=1}^{N} O_i \,, \tag{83}$$

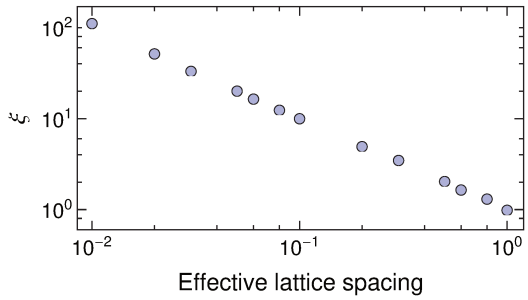

Figure 8: The correlation length ξ *versus* the effective lattice spacing ($N_{sep} = 300$, $N = 10^4$). The points fall on a straight line, indicating a power-law dependence. The error bars were constructed using a jackknife analysis. Error bars are smaller than the symbol size.

where N is the number of measurements. An unbiased estimator of the sample variance is given by

$$\sigma^2_{O,\mathrm{std}} = \frac{1}{N-1}\sum_{i=1}^{N}[O_i - E(O)]^2. \tag{84}$$

This estimator is applicable even if the measurements are somewhat correlated, that is, not entirely independent of each other. The square root of the variance of the estimator of the sample mean is the error in our estimate, not the square root of the variance of the distribution. For the former quantity it matters whether the measurements are independent or not. For uncorrelated (independent) measurements the relation is

$$\sigma^2_{E(O),\mathrm{naive}} = \frac{\sigma^2_{O,\mathrm{std}}}{N}. \tag{85}$$

The subscript "naive" refers to the assumption that the variables are not correlated. This assumption implies that the statistical error of the mean in Eq. (83) is given by

$$\mathrm{err}_O = \sqrt{\sigma^2_{E(O),\mathrm{naive}}} = \frac{\sigma_{O,\mathrm{std}}}{\sqrt{N}}. \tag{86}$$

For correlated data the factor of N in the denominator of Eq. (85) is replaced by $N_{\mathrm{eff}} < N$, and the statistical error of the mean differs from the naive estimate in Eqs. (85) and (86). That is, for correlated data the naive estimate underestimates the true statistical error of the sample mean as shown in Fig. 9 for $\langle\hat{x}^3\rangle$ and $\langle\hat{x}^4\rangle$. The statistical error is smaller than the size of the dots in Fig. 9, yet many of the dots do not lie on the exact curve. For a fixed number of sweeps between adjacent measurements ($N_{sep} = 300$) the problem is seen to worsen for smaller effective lattice spacings.

The jackknife procedure [81] provides a more realistic estimate of the variance of the mean of a set of correlated variables. The jackknife variance of

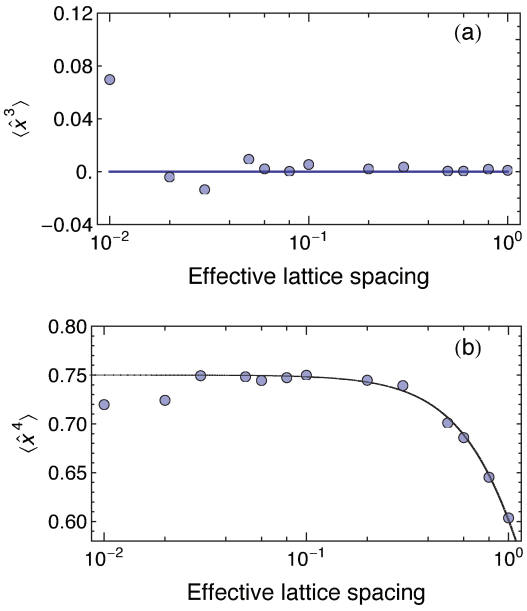

Figure 9: (a) Simulations of $\langle \hat{x}^3 \rangle$ as a function of the effective lattice spacing ($N_{sep} = 300$). (b) Simulations of $\langle \hat{x}^4 \rangle$ as a function of the effective lattice spacing (with the same parameters). The solid line is the exact result Eq. (74). The error bars are smaller than the size of the symbols, because the naive error ignores correlations between measurements.

a parameter is found by systematically leaving out batches of observations from a dataset, calculating the variance each time a different batch is omitted, and finding the average of these variance calculations. A theoretical justification of this procedure is given in Ref. [88]. The N samples are divided into N_B blocks of bin width B. The block estimators are

$$o_k = \frac{1}{B} \sum_{i=1}^{B} O_{(k-1)B+i} \quad (k = 1, \ldots N_B). \tag{87}$$

The bin width B should exceed the autocorrelation time of the observable to ensure that the N_B values can be treated as uncorrelated [3]. The bin-based variance of the mean is given by

$$\sigma^2_{E(O),\text{bins}} = \frac{1}{N_B(N_B-1)} \sum_{k=1}^{N_B} [o_k - E(O)]^2. \tag{88}$$

The estimator o_k in Eq. (88) is an average over only the N_Bth fraction of all the measurements. This limited number of measurements may prevent the determination of o_k for some k (for instance a fit based on too few configu-

3 Initially the jackknife variance will increase monotonically with bin size. After a while, it will reach a plateau *versus* the bin size, and eventually the jackknife variance will fluctuate: that is, vary non-monotonically as a function of the bin size. We should choose the bin size in the plateau region.

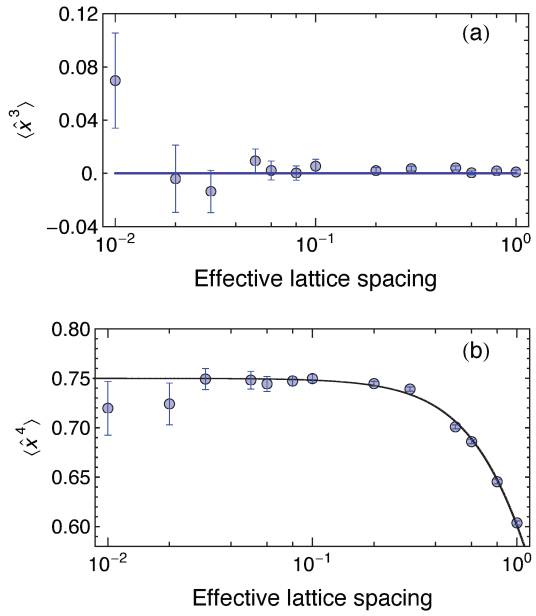

Figure 10: (a) Simulations of $\langle \hat{x}^3 \rangle$ as a function of the effective lattice spacing ($N_{sep} = 300$) with jackknife error bars, which account for correlations within the data. (b) Simulations of $\langle \hat{x}^4 \rangle$ as a function of the effective lattice spacing ($N_{sep} = 300$) with jackknife error bars. The data are always within two jackknife errors of the theoretical results in Eq. (74).

rations may occasionally fail to converge) [102]. This problem is overcome by using complementary bins:

$$\tilde{o}_k = \frac{1}{N-B}\left(\sum_{i=1}^{N} O_i - B o_k\right). \tag{89}$$

Rather than N_B estimators $o_1, \ldots, o_{N_B}$, each containing B measurements, as in Eq. (87), we work with N_B jackknife estimators $\tilde{o}_1, \ldots, \tilde{o}_{N_B}$, each based on $N - B \gg B$ measurements. The resulting complementary bin-based or jackknife variance of the mean is

$$\sigma^2_{E(O),\mathrm{jack}} = \frac{N_B - 1}{N_B} \sum_{k=1}^{N_B} [\tilde{o}_k - E(O)]^2. \tag{90}$$

Figure 10 features the same data set as Fig. 9, but this time the statistical errors are determined as $\sigma_{E(O),\mathrm{jack}}$ (see Eq. (90)). The errors are assessed reliably; the $\sigma_{E(O),\mathrm{jack}}$ error bars miss the analytical curve at a frequency consistent with the expected 32%. This figure corresponds to the relative area outside the $\pm 1\sigma$ band around the center of a normal distribution.

Note that for $\langle \hat{x}^3 \rangle$ and $\langle \hat{x}^4 \rangle$ the bin-based estimator (88) would have served the same purpose. The jackknife formula (90) is built to reproduce the result of (88) whenever an observable can be determined from a single configuration. In general, this is not true (e.g. for "secondary" observables derived

from "primary" observables through a fit). It is, therefore, common practice to use the jackknife procedure by default.

5.4 AUTOCORRELATION TIME

The correlation of a sequence of generated configurations arises naturally because one configuration differs from the next only by the result of a fixed number of sweeps. The autocorrelation time provides information on how strongly subsequent measurements are correlated. Because correlations lead to increased errors in measurements, its accurate assessment is important. The autocorrelation for an observable $\langle \hat{O} \rangle$, which takes values $\{O_i\}$, as a function of Monte Carlo time t_{MC} is defined as:

$$A_O(t_{MC}) = E[(O_i - E(O_i))(O_{i+t_{MC}} - E(O_{i+t_{MC}}))] \tag{91}$$

$$= \frac{1}{N - t_{MC} - 1} \sum_{i=1}^{N-t_{MC}} [O_i - E(O_i)][O_{i+t_{MC}} - E(O_{i+t_{MC}})], \tag{92}$$

where the average $E(O_i)$ is over the first $N - t_{MC}$ measurements and the average $E(O_{i+t_{MC}})$ over the last $N - t_{MC}$ measurements. Note that $A_O(0) = \sigma^2_{O,std}$.Comparisons between autocorrelation times for different observables are easier to make when the normalized $A_O(t_{MC})/A_O(0)$ is considered instead.

Two parameters can be extracted from Eq. (91): the asymptotic (or exponential) and the integrated autocorrelation times. The autocorrelation function of O typically exhibits multi-exponential behavior [42]:

$$\frac{A_O(t_{MC})}{A_O(0)} = a_0 e^{-t_{MC}/\tau_0} + a_1 e^{-t_{MC}/\tau_1} + \cdots, \tag{93}$$

with $\tau_0 < \tau_1 < \tau_2 < \cdots$. Usually $a_0 \gg a_1 \gg a_2 \gg \cdots$, where $a_0 + a_1 + a_2 + \cdots = 1$. Determining the "true" exponential autocorrelation time, defined as $\max(\tau_0, \tau_1, \tau_2, \cdots)$, requires precise data at large t_{MC}, which are not normally available. To obtain an estimate for the exponential autocorrelation time, we make a multi-exponential fit as in Eq. (93). In practice, such a fit is likely to contain one or two terms.

To determine the integrated autocorrelation time, we start from the variance of the unbiased estimator of the mean. Let t_{MC} be the absolute time difference between measurement i and j, such that

$$\begin{aligned}
&\left(\frac{1}{N}\sum_{i=1}^{N} O_i - E(O_i)\right)^2 \\
&= \frac{1}{N^2}\sum_{i=1}^{N}\sum_{j=1}^{N}[O_i - E(O_i)][O_j - E(O_j)] \\
&= \frac{1}{N}\sigma^2_{O,\mathrm{std}} + \frac{1}{N^2}\sum_{i=1}^{N}\sum_{j\neq i}[O_i - E(O_i)](O_j - E(O_j)] \\
&= \frac{1}{N}\sigma^2_{O,\mathrm{std}} + \frac{2}{N^2}\sum_{i=1}^{N-1}\sum_{j=i+1}^{N}[O_i - E(O_i)][O_j - E(O_j)] \\
&= \frac{\sigma^2_{O,\mathrm{std}}}{N}\left\{1 + \frac{2}{N}\frac{1}{\sigma^2_{O,\mathrm{std}}}\sum_{t_{MC}=1}^{N-1}\sum_{i=1}^{N-t_{MC}}[O_i - E(O_i)][O_{i+t_{MC}} - E(O_{i+t_{MC}})]\right\} \\
&= \frac{2\sigma^2_{O,\mathrm{std}}}{N}\left\{\frac{1}{2} + \frac{N - t_{MC}}{N}\sum_{t_{MC}=1}^{N-1}\frac{A_O(t_{MC})}{A_O(0)}\right\}. \qquad (94)
\end{aligned}$$

For $N \gg 1$ the right-hand side of Eq. (94) approaches $(2\sigma^2_{O,\mathrm{std}}/N)\tau_{O,\mathrm{int}}$, where

$$\tau_{O,\mathrm{int}} = \frac{1}{2} + \sum_{t_{MC}=1}^{N-1}\frac{A_O(t_{MC})}{A_O(0)}. \qquad (95)$$

Comparison of Eq. (94) with the naive variance of the mean in Eq. (85) shows that the effective number of independent measurements is $N_{\mathrm{eff}} = N/(2\tau_{O,\mathrm{int}})$.

To compute the integrated correlation time, we have to cut off the sum where the exponential relation for $A_O(t_{MC})$ breaks down. If the cutoff is clearly defined (for example, at the first value where the autocorrelation becomes negative), the integrated autocorrelation time takes a unique value for a given data set, and is thus less subjective than the exponential correlation time. However, the latter clearly captures the exponential behavior of the autocorrelations[4].

Figure 11 shows the dependence of the autocorrelation time of an observable $\hat{X}$ on the lattice spacing. For a given operator $\hat{O}$, we expect [42, 56] $\tau_O \sim \tilde{\xi}^z$ and $z \simeq 2$ for local updating algorithms [73]. Similar power-law behavior can be observed for the integrated autocorrelation time. We have chosen the number of lattice sites N_τ to be inversely related to the lattice spacing to keep the time T in physical units constant. Hence, when moving

4 The Matlab function UWerr.m, Version 6, described in Ref. [102], was used to determine the statistical errors of the autocorrelation time.

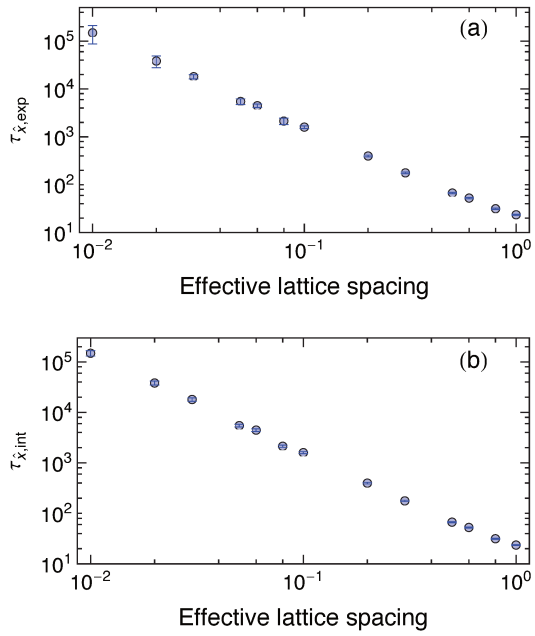

Figure 11: (a) Number of lattice updates required to generate a path independent of its predecessor as a function of the lattice spacing $\tilde{m}$. The exponential autocorrelation time of the observable $\hat{x}$ exhibits power-law behavior as a function of $\tilde{m}$, $\tau_{\hat{x},exp} \sim \tilde{m}^{-1.86}$. (b) The integrated autocorrelation time as a function of $\tilde{m}$. As for the exponential autocorrelation time, the time required for two independent paths exhibits power-law behavior, $\tau_{\hat{x},int} \sim \tilde{m}^{-1.85}$.

toward the continuum, the time increases as $\tau_O \tilde{\xi}^d$ in d dimensions (in our case $d = 1$).

Another way to express the computational difficulties in taking the continuum limit is that for fixed computational time, the exponential increase in the autocorrelation time as a function of the inverse lattice spacing causes an increase of the statistical errors, meaning that the reliability of results is limited for very small lattice spacings. A possible remedy is to change the updating strategy. The multigrid method, which employs intrinsically nonlocal updates, is an effective way to address large correlation lengths.

5.5 OVER-RELAXATION

The goal of the over-relaxation method is to reduce autocorrelation times. To this end, a trial change $\tilde{x}_{i,trial}$ far from the old value $\tilde{x}_i$, but involving small changes in the action, is proposed. Creutz [22] and Brown and Woch [14] suggest:

$$\tilde{x}_{i,trial} = \frac{\tilde{x}_{i-1} + \tilde{x}_{i+1}}{1 + \frac{1}{2}\tilde{\omega}^2} - \tilde{x}_i \,. \tag{96}$$

The variable

$$\tilde{x}_{i,\mathrm{mid}} \equiv \frac{\tilde{x}_{i-1} + \tilde{x}_{i+1}}{2 + \tilde{\omega}^2} \tag{97}$$

minimizes the part of the action that depends on $\tilde{x}_i$. Thus, $\tilde{x}_{i,\mathrm{trial}}$ lies "on the other side" of this minimum for fixed x_{i-1} and x_{i+1}. The update $\tilde{x}_i \to \tilde{x}_{i,\mathrm{trial}}$ is microcanonical, meaning that the action is constant under this change and no Metropolis accept/reject step is needed. The disadvantage of Eq. (96) is that the procedure is not applicable to actions for which $\tilde{x}_{i,\mathrm{mid}}$ cannot be found exactly, such as an anharmonic oscillator. Because the ratio of the kinetic to potential energy increases strongly in the continuum limit, we propose a trial change that preserves the kinetic part of the action:

$$\tilde{x}_{i,\mathrm{kin}} = (\tilde{x}_{i-1} + \tilde{x}_{i+1}) - \tilde{x}_i, \tag{98}$$

followed by a standard accept/reject procedure. In the continuum limit, the term $1 + \tilde{\omega}^2/2$ in Eq. (96) approaches 1. Thus, in this limit, the trial change $\tilde{x_i}''$ approaches the choice of $\tilde{x_i}'$ by Creutz [22] and Brown and Woch [14]. We note that the acceptance rate for $\tilde{x_i}''$ approaches one in the continuum limit, where the kinetic term dominates. Equation (98) can be used for any potential term. The only change in the pseudocode given in Appendix D is the value of x_{new}. Usually all sweeps are Metropolis sweeps; for the over-relaxation routine used to create Fig. 12, four in five Metropolis sweeps were exchanged for over-relaxed sweeps. The error bars are visibly smaller with over-relaxation. Because the CPU time needed for an over-relaxed sweep is comparable to that required for an ordinary Metropolis sweep, the accuracy of the measurements is significantly improved at constant computational cost.

5.5.1 The anharmonic oscillator

The anharmonic oscillator is interesting, not just as an application of the Monte Carlo Markov chain method developed here, but as a system where exact solutions are not available. The Rayleigh-Schrödinger perturbation is known [8] to diverge, which has led to the development of approximate methods to estimate and place bounds on the energy levels of this system [51].

The action of the quantum anharmonic oscillator is

$$\tilde{S} = \sum_{i=1}^{N_\tau} \frac{1}{2}\tilde{m}(\tilde{x}_{i+1} - \tilde{x}_i)^2 + \frac{1}{2}\tilde{m}\tilde{\omega}^2\tilde{x}_i^2 + \frac{1}{4}\lambda\tilde{x}_i^4. \tag{99}$$

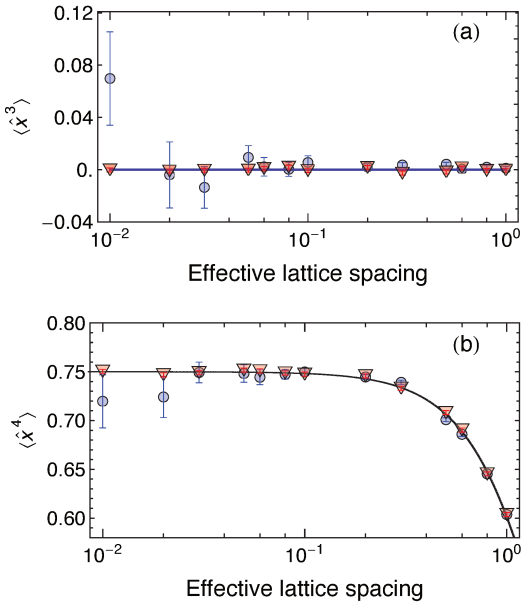

Figure 12: Over-relaxed simulations for the observables $\langle \hat{x}^3 \rangle$ and $\langle \hat{x}^4 \rangle$ are shown by the triangles ($N_\tau = 120/\tilde{m}$; $N_{sep} = 300$). The reliability of the results is improved with no additional computational expense.

We have chosen the over-relaxation update $x_i \to \tilde{x}_i''$ in Eq. (98) such that it carries over to actions with an anharmonic term.

6 ONE-DIMENSIONAL RESULTS

This Chapter is again focused on one-dimensional Darcy flow. It presents detailed comparisons of pressure statistics results obtained through the finite-volume and path integral methods, under Neumann and Dirichlet boundary conditions.

6.1 PRESSURE STATISTICS FOR NEUMANN BOUNDARY CONDITIONS

Pressure statistics for Darcy flow obtained from the stochastic differential equation and the path integral are shown in Fig. 13. We have used a system size of $X = 240$ m with $P_i/X = 10^4$ Pa/m and $q_0 = 10^{-6}$ m/s, which are typical estimates for Darcy flow of oil in rocks. The probability density of the pressure was calculated at various points in the rock for several values of the correlation length. These correspond to vertical slices at the chosen points through the realizations of the type shown in Fig. 3. Because the initial pressure is greater than the final pressure, the pressure distributions are shown at positions that increase from right to left. For the three largest values of the correlation length, the graph corresponding to $x = 0.9X$ was left out to improve clarity. The pressure is fixed at $x = 0$. Away from this point, the distributions broaden in a manner determined by the correlation length of the permeability (Fig. 2), but the free boundary condition at $x = X$ means that the broadening continues unabated for $x > 0$.

The resistance term $R(x)$ is an integral over correlated log-normal stochastic variables. For small values of x/ξ, R is the integral over weakly correlated log-normal variables over a short distance (small ξ), or the integral over more strongly correlated stochastic variables over a longer distance (larger ξ). In both of these cases, we are able to make a log-normal fit to $R(x)$ and, consequently, to $p(x)$. These fits (Fig. 13) are based on the empirical first and second moments of the simulations.

Table 3 compares the mean and standard deviation of the pressure distribution obtained from the evaluation of the path integral (μ_s and σ_s), from the solutions (168) and (170) of the Fokker-Planck equation of the Ornstein-Uhlenbeck process (μ_c and σ_c), found in App. E and the discrete forms (172) and (174) corresponding to the discretization of the finite-volume method in Section 3.2 ($\mu_d = \mu_c$ and σ_d), found in App. F. There are two sources of

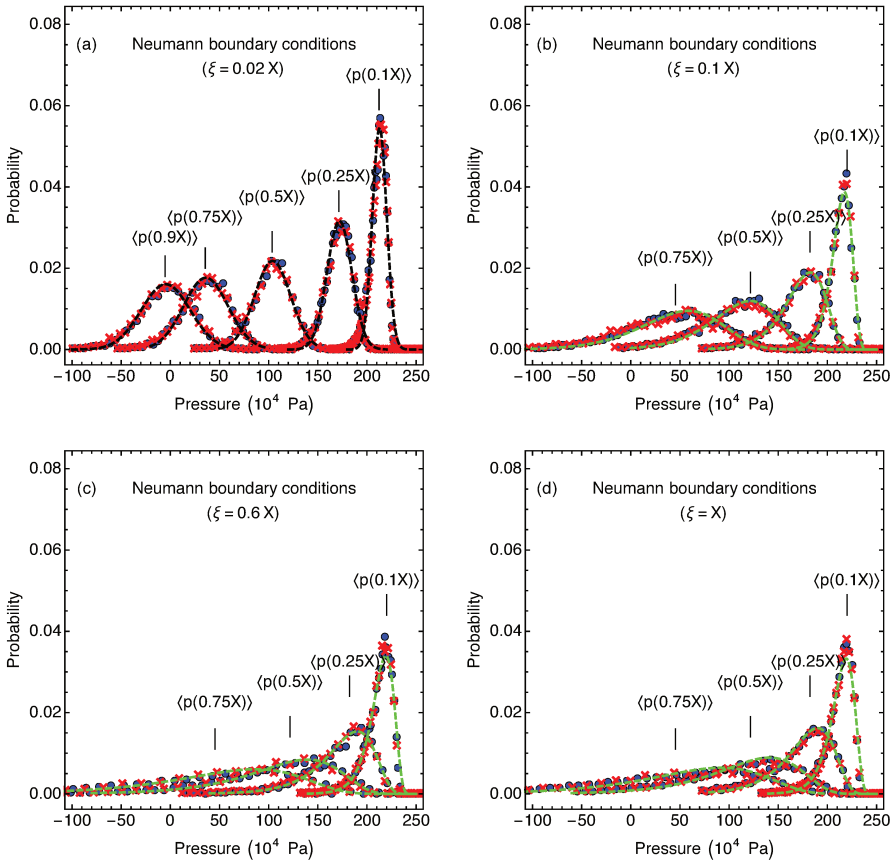

Figure 13: Pressure statistics for Darcy flow under NBC for correlation lengths of the stochastic permeability (Fig. 7) of (a) $\xi = 0.02X$, (b) $\xi = 0.1X$, (c) $\xi = 0.6X$, and (d) $\xi = X$ obtained from the finite volume method (disks) and the path integral (crosses). Fewer data points are shown than used for statistical analysis. The dashed green and black lines represent the log-normal fits and Gaussian approximations, respectively. The calculations are based on $N = 10^4$ simulations on lattices with $N_x = 240$ sites and spacing $\Delta x = 0.5$ m. The path integral and stochastic data agree to a confidence level of 95%.

the discrepancies between the results from the path integral, which are regarded as "exact", and the two sets of calculations in Appendix F.1: lattice effects and correlations.

Figure 13 shows that the Gaussian approximation is most accurate for the smallest correlation length (Fig. 13(a)), with correlation effects becoming more evident with increasing correlation length (Fig. 13(b,c,d)). Correlation effects play a role in both the discrete and the continuous approximations to the path integral calculations. The Gaussian approximation becomes more appropriate as the ratio ξ/x decreases. The "breakdown of Gaussianity" can be clearly seen in Fig. 13(b,c,d): Gaussian fits are only appropriate for the smallest correlation length. Due to the strong correlation, the pressure distributions are seen to broaden appreciably away from the boundary. The data in Table 3 support this trend in the comparisons between the values of the mean and standard deviation obtained from the path integral and the

$\xi(X)$	$x(X)$	μ_s	μ_c	σ_s	σ_d	σ_c
	0.1	212.168	212.804	8.08306	7.32955	7.97994
	0.25	171.354	172.011	13.5634	12.6210	13.4854
0.02	0.5	103.348	104.022	19.5774	18.3138	19.4676
	0.75	35.4959	36.0333	24.3331	22.6163	24.0024
	0.9	-5.27945	-4.76007	26.6637	24.8427	26.3513
	0.1	212.318	212.804	12.5381	12.1807	12.2510
	0.25	171.466	172.011	25.5700	25.1552	25.1849
0.1	0.5	103.167	104.022	39.9844	39.8835	39.8997
	0.75	35.3963	36.0333	50.5274	50.7368	50.7478
	0.9	-5.26133	-4.76007	55.8586	56.2633	56.2723
	0.1	212.055	212.804	14.6806	13.9840	14.0545
	0.25	171.198	172.011	34.4524	33.5988	33.6267
0.6	0.5	103.320	104.022	63.2270	62.8236	62.8375
	0.75	35.2116	36.033	88.2456	88.5658	88.5751
	0.9	-5.83536	-4.76007	102.159	102.640	102.648
	0.1	212.203	212.804	14.6486	13.8463	14.2264
	0.25	171.397	172.011	35.1531	34.2714	34.6159
1.0	0.5	103.082	104.022	67.2820	65.9685	66.3126
	0.75	34.7882	36.033	96.7118	95.1455	95.4987
	0.9	-6.18528	-4.76007	113.349	111.588	111.947

Table 3: Means and standard deviations of the pressure as a function of position x and noise correlation length ξ for Neumann boundary conditions for a one-dimensional system obtained from simulations (μ_s and σ_s) and calculations from the solution to the Fokker-Planck equation (μ_c and σ_c), and from a calculation that incorporates the discreteness of the simulation (σ_d).

approximations. A comparison between the discrete and continuous approximations to the standard deviation (σ_d and σ_c, respectively) makes apparent that σ_c is a better approximation to the standard deviation σ_s obtained from the path integral calculation. These discrepancies are indicative of the error caused by the discretization, which diminishes with increasingly refined lattice spacing.

We now consider the case of small ξ/x. In the limiting case $\xi \to 0$, each stochastic variable $K(x)$ is drawn from the Gaussian probability function (App. E). Indeed, the central limit theorem (CLT) mandates that the sum of N independent, identically distributed random variables tends to a normal distribution in the limit of large N if all moments of the distribution are finite. An alternative version of the CLT holds for correlated random variables and states that the sum of N realizations of an ergodic process (whose long-term average is equal to its expectation value [60]), will behave as a Gaussian random variable in the limit of large N [12]. The process K is a Markov process with continuous trajectories, otherwise known as a "diffusion" process [78]. The probability law of K is invariant under time reversal. Since all reversible diffusions are ergodic [78], the alternative version of the CLT applies to $R(x)$.

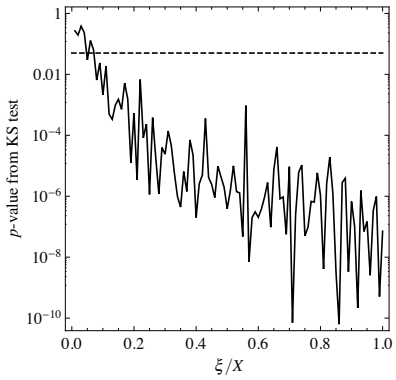

Figure 14: The p-value obtained from the KS test for $R(X)$ as a function of ξ/X.

Under what conditions can $R(x)$ be approximated by a Gaussian random variable? Clearly, the criterion depends on the ratio ξ/x. We have determined the order of magnitude of ξ/x below which $R(x)$ is approximately Gaussian. To do so, we made use of the Kolmogorov-Smirnov (KS) test, which is a statistical test that determines the probability (or "p-value" [94]) that a data sample follows a given distribution (one-sided test), as well as the probability that two data sets follow the same distribution (two-sided test) [70]. More details on the Kolmogorov-Smirnov test can be found in Appendix G. For $R(x)$, we performed a one-sided KS test at the 95% confidence level: if the p-value is below 5%, we reject the "null hypothesis" that the sample is normally distributed. Of course, the greater the p-value, the better the quality of the approximation. A two-sided KS test was carried out for all pairs of data sets (FVM and path integral) at the 95% confidence level, which all pairs of data sets passed.

We have carried out a KS test for 100 different values of ξ/x, each based on $N = 1000$ realizations of R [1]. The realizations were of $R(X)$; if R is found to be Gaussian at any point in $[0, X]$, then it is Gaussian on the entire interval, due to the strict stationarity of Gaussian stochastic processes (App. E). From Fig. 14 we infer that the Gaussian approximation breaks down for

$$x \gtrsim 10\,\xi. \tag{100}$$

For $\xi = 0.02X$, we were therefore able to make Gaussian fits to $p(x)$ for all values of x. These fits are shown in Fig. 14. If it is possible to make a Gaussian approximation, it is advantageous to do so, because it can be based on the theoretical mean and variance of $p(x)$ and does not require any simulations. A calculation of the first and second moments of $p(x)$ under NBC can be found in F.1.

1 The in-built KS test *kstest2* of MATLAB_R2014b, The MathWorks, Inc. was used for this analysis.

6.2 PRESSURE STATISTICS FOR DIRICHLET BOUNDARY CONDITIONS

Under Dirichlet boundary conditions, the pressure $p(x)$ takes the form

$$p(x) = P_i - (P_f - P_i)\frac{R(x)}{R(X)}. \tag{101}$$

From the Kolmogorov-Smirnov test done in Section 6.1 we know that $R(x)$ can be approximated by a Gaussian random variable whose mean is strictly positive and much greater than its variance (see App. F.2), provided the condition (100) is met. The ratio

$$\frac{R(x)}{R(X)} = \frac{\int_0^x \frac{1}{K(x')}\,dx'}{\int_0^x \frac{1}{K(x')}\,dx' + \int_x^X \frac{1}{K(x')}\,dx'} \tag{102}$$

is then a function of correlated Gaussians. We have taken as our working assumption that a Gaussian approximation can be made to (102) if $x \gtrsim 10\xi$. This assumption, verified by further Kolmogorov-Smirnov tests, turns out to be correct. As for NBC, we have made Gaussian approximations to the pressure distributions for the parameter choice $\xi = 0.02X$; for the other parameter choices, we have made lognormal fits to the pressure distributions. A derivation of these approximations is given in Appendix F.

The Gaussian theoretical curves and log-normal fits were made green in Fig. 15. Other than the final pressure, $P_f/X = 0$ Pa/m, and q_0, which is not fixed, all parameters were set to the same values as under Neumann boundary conditions. Because the initial and final pressures are fixed, the distributions are narrowest near the ends of the system. The distributions broaden away from the endpoints. The pressure range is greater for the system with the smaller correlation length for the permeability. This results from the pressure paths showing a smaller variation with the smaller correlation length. In the case of DBC, the pressure distributions $p(x)$ are symmetric about $x = X/2$, due to the strict stationarity of the Ornstein-Uhlenbeck process (see App. E). The influence of the correlation length is, therefore, felt at both ends of the interval $[0, X]$, and the Gaussian approximation is best in the center of the "rock".

The comparison between the mean and standard deviation obtained from path integral simulations with those from discrete and continuous calculations with the Gaussian approximation is shown in Table 4. As expected, the accuracy of the Gaussian approximation diminishes with increasing correlation length. The spatial effect of increased Gaussianity is less apparent under Dirichlet boundary conditions: the "rock" has two boundaries. One

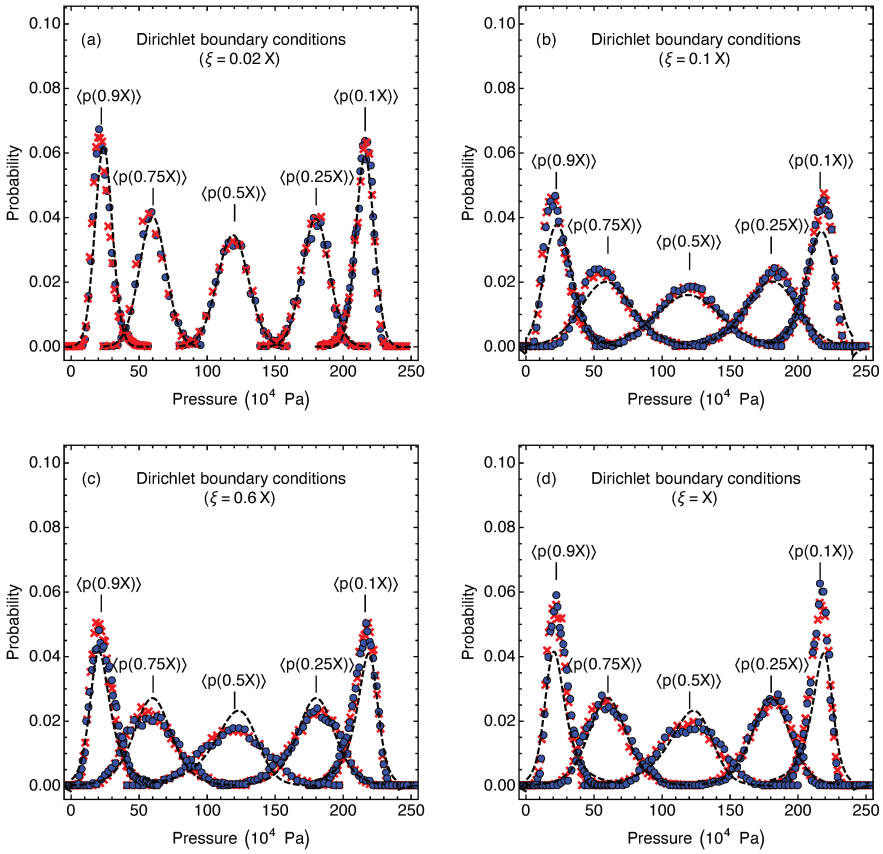

Figure 15: Pressure statistics for Darcy flow under DBC for correlation lengths $\xi = 0.02X$ (a), $\xi = 0.1X$ (b), $\xi = 0.6X$ (c) and $\xi = X$ (d). Simulations were done using the finite volume method (disks) and path integral method (crosses). Fewer data points are shown than used for statistical analysis. The dashed green and black lines represent the log-normal fits and Gaussian approximations, respectively. The calculations are based on $N = 10^4$ simulations on a lattice of $N_x = 240$ lattice sites and lattice spacing $\Delta x = 0.5$ m. The path integral and stochastic data agree to a confidence level of 95%.

can only get half as far away from the boundary, where the approximation is most fitting.

Contrary to the calculations done for Neumann boundary conditions, there is no exact equality between the mean resulting from the Fokker-Planck equation (μ_s) and its discrete counterpart (μ_d). Under Neumann boundary conditions, the approximate mean depends only on the expectation value of R (Eq. (167)). This quantity does not depend on the nature of the approximation. By contrast, under Dirichlet boundary conditions the standard deviation of the pressure depends on many quantities, including the variance of R and the correlation between values of R at different points. These variables in turn depend on correlation effects, which a discrete setup estimates more crudely than a continuous one.

$\xi(X)$	$x(X)$	μ_s	μ_d	μ_c	σ_s	σ_d	σ_c
	0.1	215.537	215.638	215.793	6.65118	7.39637	8.05491
	0.25	179.497	179.830	179.748	9.976593	8.61085	10.4318
0.02	0.5	119.300	120.50	119.499	11.76703	11.2895	12.0930
	0.75	59.3505	59.2513	59.2475	10.1345	9.64244	10.3687
	0.9	23.2585	23.1188	23.1126	6.512375	6.08723	7.71568
	0.1	215.517	212.630	214.834	9.782208	10.7666	9.08430
	0.25	179.703	178.413	179.655	17.73364	19.0602	14.6467
0.1	0.5	119.857	120.427	119.500	21.855	26.1954	17.1548
	0.75	60.0631	59.8698	59.3168	17.65783	20.9629	14.4449
	0.9	23.8099	23.7858	23.2374	9.600161	11.0541	8.66795
	0.1	214.934	204.426	203.015	8.798261	22.7199	25.6091
	0.25	178.866	169.881	168.652	17.41341	35.2504	36.1574
0.6	0.5	119.463	116.881	115.825	22.56851	44.9074	45.2879
	0.75	60.1718	62.4917	62.4303	17.27851	35.2585	35.6411
	0.9	24.0128	26.8928	26.9697	8.472904	21.3853	21.6713
	0.1	215.072	202.156	200.700	7.567443	26.8830	29.5648
	0.25	178.946	166.939	166.407	15.25785	38.9908	39.8613
1.0	0.5	119.497	115.702	114.638	19.99505	47.5015	47.8495
	0.75	59.8951	62.6097	62.5277	15.08735	37.3308	37.6855
	0.9	23.817	27.4292	27.4930	7.327701	23.4083	23.6594

Table 4: Means and standard deviations of the pressure as a function of position x and noise correlation length ξ for Dirichlet boundary conditions for a one-dimensional system obtained from simulations (μ_s and σ_s) and calculations from the solution to the Fokker–Planck equation (μ_c and σ_c), and from a calculation that incorporates the discreteness of the simulation (μ_d and σ_d)

7 EXTENSION TO HIGHER DIMENSIONS

7.1 THE FINITE-VOLUME METHOD IN HIGHER DIMENSIONS

The finite-volume method was designed to solve Equation (3), subject to appropriate boundary conditions, numerically. Its use does not require an analytic expression for the pressure. Its one-dimensional form, given in Section 3.2, is readily generalized.

In two dimensions, the pressure is defined on an $N_x \times (N_y + 2)$ lattice. To cast Eq. (3) in matrix form, the pressure must be expressed as a vector. We have used the common form

$$(p_{(00)}, p_{(01)}, \cdots, p_{(N_x-1,0)}, p_{(01)}, \cdots, p_{(N_x-1,1)}, \cdots, p_{(0,N_y+1)}, \cdots, p_{(N_x-1,N_y+1)})^T. \tag{103}$$

Dirichlet boundary conditions are imposed at $y = 0$ and $y = N_y + 1$, which makes the y-direction into the main flow direction. The lattice sites

$$\{p_{(00)}, \cdots, p_{(N_x-1,0)}\} \tag{104}$$

are fixed at the value P_i, while the sites

$$\{p_{(0,N_y+1)}, \cdots p_{(N_x-1,N_y+1)}\} \tag{105}$$

take the value P_f. At the "top" and "bottom" of the lattice Neumann boundary conditions are implemented. These dictate that the flow between $p_{(0,j)}$ and $p_{(1,j)}$ and that between $p_{(N_x-2,j)}$ and $p_{(N_x-1,j)}$ is zero for $j = 1, ..., N_y$. This standard set of boundary conditions will be referred to as "no-flow boundary conditions". The resulting transmissibility matrix is symmetric and pentadiagonal.

In three dimensions, the obvious analogue is an $N_x \times (N_y+2) \times N_z$ lattice. The pressure is "rolled up" as

$$\begin{aligned}
&(p_{(000)}, p_{(010)}, \cdots, p_{(N_x-1,00)}, p_{(010)}, \cdots, p_{(N_x-1,10)}, \cdots, p_{(0,N_y+1,0)}, \cdots,\\
&p_{(N_x-1,N_y+1,0)}, \cdots,\\
&p_{(001)}, p_{(011)}, \cdots, p_{(N_x-1,01)}, p_{(011)}, \cdots, p_{(N_x-1,11)}, \cdots, p_{(0,N_y+1,1)}, \cdots,\\
&p_{(N_x-1,N_y+1,1)}, \cdots,\\
&p_{(00,N_z-1)}, p_{(01,N_z-1)}, \cdots, p_{(N_x-1,0,N_z-1)}, p_{(01,N_z-1)}, \cdots,\\
&p_{(N_x-1,1,N_z-1)}, \cdots, p_{(0,N_y+1,,N_z-1)}, \cdots, p_{(N_x-1,N_y+1,,N_z-1)})^T. \qquad (106)
\end{aligned}$$

As in two dimensions, Dirichlet boundary conditions are imposed at $y = 0$ and $y = N_y + 1$. The 3D-transmissibility matrix is heptadiagonal, and, of course, symmetric.

7.2 EULER–LAGRANGE APPROACH

The one-dimensional path integral is an integral over all pressure trajectories that (subject to the boundary conditions) follow Darcy's law, which is enforced by means of a delta functional (see Eq. (26)). Computationally, one generates pressure paths according to the probability distribution $S(\{p_i\})$, with the discrete action (29) based on the solution to Darcy's law.

An analogous path integral in two dimensions is obtained with the standard procedure for classical statistical dynamics [31, 57, 58, 79]:

$$\begin{aligned}
Z_{2D} = &\int \prod_{ij} dp_{ij} \int \prod_{kl} dL_{kl} \exp\left(-\sum_{ij} L_{ij}\right)\\
&\times \exp\left[-\sum_{ij,kl} L_{ij} (C_L^{-1})_{ij,kl} L_{kl}\right] \delta\left\{\left[\frac{\partial(e^L \nabla p)}{\partial x}\right]_{i,j} + \left[\frac{\partial(e^L \nabla p)}{\partial y}\right]_{i,j}\right\}. \qquad (107)
\end{aligned}$$

The delta-function enforces the discrete form of Darcy's law, where we have used the notation

$$\begin{aligned}
\left[\frac{\partial(e^L \nabla p)}{\partial x}\right]_{i,j} &= \frac{1}{\Delta x}\left[e^{L_{i,j}}\left(\frac{p_{i,j}-p_{i-1,j}}{\Delta x}\right) - e^{L_{i-1,j}}\left(\frac{p_{i-1,j}-p_{i-2,j}}{\Delta x}\right)\right]\\
&= \frac{1}{\Delta x^2}\left[e^{L_{i,j}} p_{i,j} - (e^{L_{i,j}} + e^{L_{i-1,j}}) p_{i-1,j} + e^{L_{i-1,j}} p_{i-2,j}\right]\\
\left[\frac{\partial(e^L \nabla p)}{\partial y}\right]_{i,j} &= \frac{1}{\Delta y}\left[e^{L_{i,j}}\left(\frac{p_{i,j}-p_{i-1,j}}{\Delta y}\right) - e^{L_{i-1,j}}\left(\frac{p_{i-1,j}-p_{i-2,j}}{\Delta y}\right)\right]\\
&= \frac{1}{\Delta y^2}\left[e^{L_{i,j}} p_{i,j} - (e^{L_{i,j}} + e^{L_{i-1,j}}) p_{i-1,j} + e^{L_{i-1,j}} p_{i-2,j}\right] \qquad (108)
\end{aligned}$$

The next step is to represent the delta-function as the limit of an exponential, so that the exponentials in (107) can be combined into a single exponential whose argument is the action. The usual procedure [31, 57, 58, 79] is to apply a functional Fourier transform, which yields a *complex* action. This is appropriate for formal studies involving perturbation expansion, where the complex action yields real results despite the complex nature of intermediate calculations. However, the Markov chain Monte Carlo method relies on real variables from the outset, so we represent the delta functional as the limit of a Gaussian probability density:

$$\begin{aligned} Z_{2D} = \int \prod_{ij} dp_{ij} \int \prod_{kl} dL_{kl} \exp\left(-\sum_{ij} L_{ij}\right) \\ \times \exp\left[-\sum_{ij,kl} L_{ij} (C_L^{-1})_{ij,kl} L_{kl}\right] \\ \times \lim_{t\to 0} \left\{ \exp\left[\frac{1}{t}\left(\frac{e^{L_{i,j}} p_{i,j} - (e^{L_{i,j}} + e^{L_{i-1,j}}) p_{i-1,j} + e^{L_{i-1,j}} p_{i-2,j}}{\Delta x^2}\right.\right.\right. \\ \left.\left.\left. + \frac{e^{L_{i,j}} p_{i,j} - (e^{L_{i,j}} + e^{L_{i-1,j}}) p_{i-1,j} + e^{L_{i-1,j}} p_{i-2,j}}{\Delta y^2}\right)\right]\right\}. \end{aligned} \tag{109}$$

This expression is readily generalized to three dimensions.

Averages of pressure and correlation functions can be calculated from (109) by first generating permeability fields, then setting t to some value, and finally using the Metropolis-Hasting (MH) algorithm to minimize the discrete action:

$$S^{\text{disc}} = \sum_{ij} \left\{ \left[\frac{\partial(e^L \nabla p)}{\partial x}\right]_{i,j} + \left[\frac{\partial(e^L \nabla p)}{\partial y}\right]_{i,j} \right\}. \tag{110}$$

Successively smaller values of t are chosen until there is convergence of the pressure distributions. This procedure, which requires separate calculations for each value of t, is not especially efficient.

Rather, computation of the integral (109) requires generating permeability fields according to their assigned distribution, followed by a determination of the pressure field that minimizes the discrete action. To account for any number of dimensions, let us write the action in its continuum form:

$$S^{\text{cont}} = \int \frac{1}{2} K (\nabla p)^2 \, dV, \tag{111}$$

where the integral is carried out over the entire volume under consideration.

We show that the minimized pressure follows Darcy's law. The objective is to extremize the action (111) with respect to the pressure. We vary the action

with respect to p by adding an infinitesimal pressure δp and imposing the condition

$$S^{\text{cont}}[p(x) + \delta p(x)] - S^{\text{cont}}[p(x)] = 0\,. \tag{112}$$

Any boundary conditions are unchanged, so $\delta p(x) = 0$ at the boundaries of the volume V. If there exists a p^* such that the stationarity condition (112) holds, the action S is stationary at p^*. Retaining δp only to first order and performing an integration by parts, we obtain

$$\begin{aligned} S^{\text{cont}}[p + \delta p] - S^{\text{cont}}[p] &= \int K\,(\nabla p)\,(\nabla \delta p)\;\mathrm{d}V \\ &= -\int \nabla \cdot (K \nabla p)\,\delta p\,\mathrm{d}V - \int_{\partial V} K \delta p \nabla p \cdot \mathrm{d}S\,. \end{aligned} \tag{113}$$

The boundary term vanishes because of Dirichlet boundary conditions fix the pressure across the entry and exit surfaces, and the absence of pressure fluctuations along surfaces perpendicular to the flow direction. Because K is always nonzero, the condition (112) translates into

$$\nabla \cdot (K \nabla p) = 0, \tag{114}$$

which is Darcy's law for incompressible flow. Thus, if p^* can be found such that the stationarity condition is met at fixed K, then p^* follows Darcy's law.

7.3 SIMULATED ANNEALING

The simulated annealing algorithm [65] can be applied to the action (111) to solve for the pressure. It is inspired by the process of annealing: a treatment whereby a solid is slowly cooled until its structure is eventually frozen at its minimum energy configuration [34]. If a solid is heated past its recrystallization temperature, atoms migrate in the crystal lattice, altering its structure. As the material is cooled, it progresses towards its equilibrium state. Its eventual structural properties will depend on the rate of cooling. If cooled too fast, the material will get stuck in a configuration corresponding to a local minimum of its "energy landscape", and the resulting crystal will contain imperfections. The defect-free crystal state corresponds to the global minimum energy configuration.

The corresponding computational method is based on the Metropolis-Hastings algorithm, a step-by-step explanation of which is presented in Section 5.2.3. In the present case, simulated annealing seeks to minimize the action (111). Clearly, the minimum attainable value is zero. The algorithm consists of the following steps.

1. Initialize a random pressure that is consistent with the boundary conditions.

2. Execute the MH algorithm some $M \gg 1$ times. The MH algorithm lowers the value of the action S, but also accepts some modifications to the pressure that increase the action. It explores the entire "state space" (the set of values of S as a function of $p(\vec{x})$) and does not get stuck in a local minimum of the state space.

3. After every $N_s \gg 1$ steps, check the value of S. When the value of S starts to fluctuate around a constant value, go to step 4.

4. Adapt the Metropolis-Hastings accept/reject criterion to: "accept the change in the action with probability $\min(1, e^{-\delta S/T})$ for some constant $0 < T < 1$". This is a "cooling step". The state space is explored in smaller steps than was the case for the standard MH algorithm, while maintaining a constant acceptance rate. The lower the value of T, the smaller the steps. In our context, T does not have the interpretation of a temperature, but its effect remains that of slowing down the state space exploration.

5. Repeat steps 3-4 until the action attains a critically low value ϵ_1, say $\epsilon_1 = 0.1$.

6. Employ a modification of the MH algorithm known as the "greedy algorithm", which accepts only changes to the pressure that lower the action, until S dives below a second critical value ϵ_2, say $\epsilon_2 = 10^{-2}$.

It should be noted that the "cooling parameter" T does not have the dimensions of a temperature, as the analogy with the cooling of solids suggests. Rather, it has the same units as the action: those of an energy dissipation rate.

For this work, we used an exponential cooling scheme

$$T^{(k)} = \alpha^k T_{\text{init}}, \tag{115}$$

where k indicates the cooling step. These parameters are vital to the efficiency and accuracy of the SA algorithm. Some care should be taken in determining their values for every new parameter set $\{\sigma, \xi, N_x, N_y, N_z\}$.

7.4 COMPUTATIONAL EXPENSE

In comparing the computational efforts involved in running the finite-volume and path integral or simulated annealing methods, we note that both require a permeability field as input. For the sake of the argument, we assume that

the calculations were run on a grid of dimensions N_x^d i. e., $N_z = N_y = N_x$. If the number of grid points is not the same for all directions, N_x^d needs to be replaced by $N_x N_y N_z$. The computational cost associated with the FFT required to generate the permeability field is $\mathcal{O}(2N_x^d \log N_x^d)$ floating point operations. The key calculation within the FVM is a sparse matrix inversion. The sparse matrix solver UMFPACK [25] can solve such an equation in $\mathcal{O}(N_x^d \log N_x^d)$ flops.

Contrary to the finite-volume method, the path integral and simulated annealing methods require $\mathcal{O}(N_x^{2d})$ flops to calculate a pressure realization. One factor N_x^d arises from the number of lattice sites. The number of required intermediate updates N_{sep} introduces a further factor N_x^d. However, there are techniques, such as over-relaxation (see Sect. 5.5) and the multigrid method [46], whose implementation is likely to decrease the run time considerably. In addition, the performance of the Metropolis-Hastings algorithm can often be improved through directed sampling [35, 36, 67].

8 HIGHER-DIMENSIONAL RESULTS

8.1 PRESSURE STATISTICS IN TWO DIMENSIONS

8.1.1 Sanity check to recover 1D-type flow

As a sanity check in two dimensions, consider an 8×240 lattice, with correlation length $\xi_x = 0.01X$ in the x-direction and $\xi_y = 0.1Y$ in the main flow direction. Dirichlet boundary conditions were imposed at $y = 0$ ($P(x, 0) = 2.4 * 10^6$ Pa) and at $y = Y$ ($P(x, Y) = 0$ Pa). No-flow boundary conditions were specified at $x = 0$ and $x = X$. We have used the exponential cooling scheme 115, within which we used the Metropolis-Hastings algorithm $M = 2,000$ times and repeated the cooling algorithm $N_s = 3,000$ times. We have calculated the pressure statistics along the "flow line" $x = 4$. The results are shown in Fig. 16. Because the correlation length in the direction transverse to the flow is very short, we anticipate recovery of the behavior of one-dimensional flow with a correlation length equal to one-tenth of the total length of the "rock". Given the short correlation length, we expect to be able to make Gaussian fits (see Sect. 6.1 for an explanation). Gaussian fits (based on the empirical mean and variance) to the pressure statistics are indeed very accurate, as Fig. 16 shows.

We have analyzed the statistics of the flow in both directions at the same points. Because of the Dirichlet boundary conditions, the flow q_y in the y-direction is peaked around $1 * 10^{-6}$ m/s. The flow in the y-direction is highly unlikely to be negative, due to the DBC and the strict positivity of the permeability. The relatively small correlation length ξ_y implies minimal fluctuations. Therefore, the distribution of ξ_y resembles that of K. The flow q_x is peaked around zero because the flow is mostly constrained to the y-direction. Due to the short correlation length ξ_x, the variance is very small.

8.1.2 Two-dimensional flow

In addition, we have simulated two-dimensional flow on a lattice that has equal lengths in both dimensions, $X = Y$, as well as equal correlation lengths in both dimensions, $\xi_x = 0.25X$; $\xi_y = 0.25Y$. Because of the Dirichlet boundary conditions, the fluid mainly flows in the y-direction. The flow is truly two-dimensional, however. We used the same cooling parameters as for the

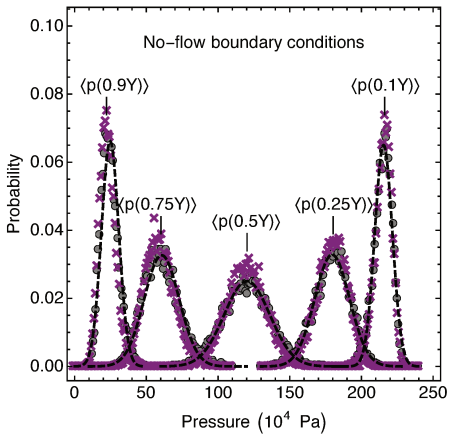

Figure 16: Pressure statistics for $N_x = 8$; $N_y = 240$, $\Delta x = \Delta y = 0.5$ m, correlation lengths $\xi_x = 0.01X$; $\xi_y = 0.1Y$. Simulations were done using the FVM (crosses) and SA (disks). Gaussian fits (dashed lines) were based on calculations of the first and second moments of the corresponding pressure statistics.

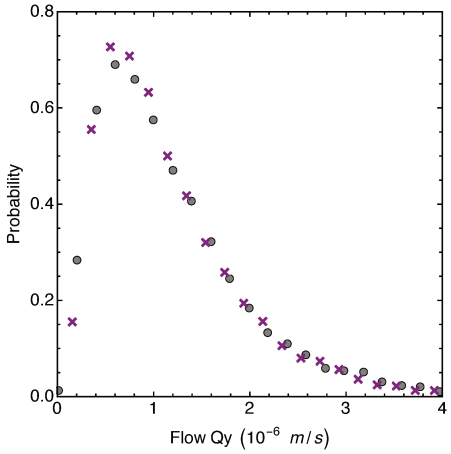

Figure 17: Flow statistics for $N_x = 8$; $N_y = 240$, correlation lengths $\xi_x = 0.01X$; $\xi_y = 0.1Y$, calculated at $x = 4$, $y = 120$. The probability density plot is sharply peaked. The flow in the y-direction approaches a log-normal distribution.

previous set of calculations. One-dimensional flow with correlation length $\xi_y = 0.25Y$ is not well-approximated by Gaussian fits (see Sect. 6.1). In this instance, Gaussian approximations are appropriate, as is shown in Fig. 18. A broadening of the pressure statistics compared to the previous case (Fig. 16) can be seen as a result of the relatively unconstrained flow. The conclusion that the fluid flows more freely can also be drawn from the flow in the x-direction, shown in Fig. 19. It is still centered at zero, but the variance is large compared to that in Fig. 17. A greater spread can be seen in the main flow direction, too, plotted in Fig. 19. Thus, as the correlation length in the direction transverse to the main flow direction increases compared to that in the main flow direction, the two-dimensional flow is less well approximated by a one-dimensional system.

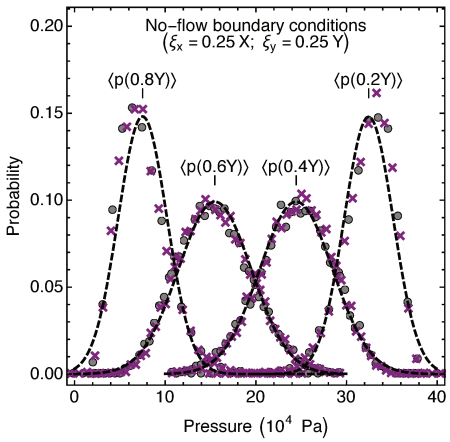

Figure 18: Pressure statistics for $N_x = 40$; $N_y = 40$, $\Delta x = \Delta y = 1$ m, correlation lengths $\xi_x = 0.25X$; $\xi_y = 0.25Y$ and no-flow boundary conditions. Simulations were done using FVM (crosses) and SA (disks). Gaussian fits (dashed lines) were based on calculations of the first and second moments of the corresponding pressure statistics.

No.	Log-permeability variance σ^2	Colour
1	0.125	grey
2	0.25	red
3	0.5	blue
4	1.0	magenta
5	1.75	brown
6	2.5	orange

Table 5: Values used for the log-permeability variance σ^2.

8.2 PRESSURE STATISTICS IN THREE DIMENSIONS

Our three-dimensional, bounded porous medium is simulated on a grid of

$$N_x \times N_y \times N_z = 50 \times 70 \times 50$$

lattice elements, representing a domain of size

$$X \times Y \times Z = 40\text{m} \times 85\text{m} \times 25\text{m}.$$

The correlation lengths in the permeability field are

$$\lambda_x = 8\text{m};\ \lambda_y = 8\text{m};\ \lambda_z = 5\text{m}.$$

We have used Dirichlet boundary conditions along the y-direction, making that the main flow direction. No-flow boundary conditions were imposed along the other boundaries. The values chosen for the log-permeability variance σ^2, the defining feature of the six parameter sets, are given in Table 5.

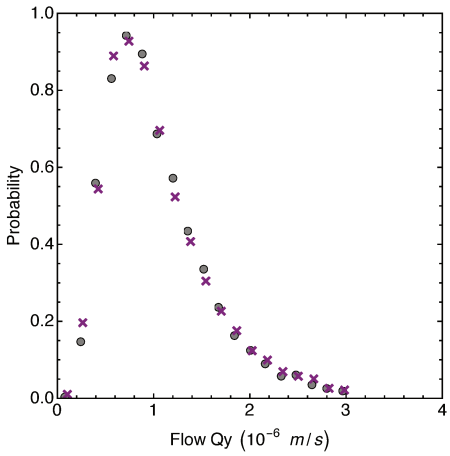

Figure 19: Flow statistics for $N_x = 40$; $N_y = 40$, correlation lengths $\xi_x = 0.25X$; $\xi_y = 0.25Y$, calculated at $x = 20$, $y = 20$. The probability density plots exhibit the same basic features as those in Fig. 17. Due to the stronger permeability correlations in the x-direction, the spread in the pressure statistics is greater in both directions.

To expedite the simulated annealing algorithm, we have used over-relaxation (see Sec. 5.5). We have again used the exponential cooling scheme 115. The Metropolis-Hastings algorithm was executed $M = 2,000$ times for all parameters. For $\sigma^2 \leqslant 1$, repeating the cooling algorithm $N_s = 3,000$ times was found to be a good choice. For $\sigma^2 > 1$, it was necessary to set $N_s = 6,000$. To calculate empirical probability density functions for the pressure and flow, we have worked with $N = 10,000$ realizations for each parameter set. We have calculated empirical probability densities for the pressure p, the flow components q_y and q_x, and the total flow Q_y and looked at the effect of the variance of the log-permeability σ^2. Based on information about boundedness, we have made parametric fits, using the choices made in [76] for guidance.

All quantities were normalized for straightforward interpretation. The Dirichlet boundary conditions were chosen to yield a pressure difference

$$\Delta p = 1m.$$

The flow components were normalized as

$$\begin{aligned} q_{x,y}* &= q_{x,y}/(K_e I_0) \\ Q_y^* &= Q_y/(K_e I_0 A), \end{aligned}$$

where K_e is the theoretical expectation value of the permeability, $I_0 = \Delta p/L_y$ and $A = L_x \times L_z$. Computationally, the normalization was achieved by setting $K_e = 1/(I_0 A)$.

Due to the nonlinearity of Darcy's law, the distributions of pressure and flow are in general not expected to be Gaussian, especially when the variance

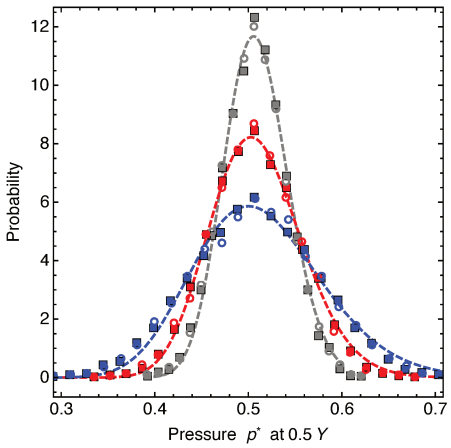

Figure 20: Pressure statistics for Darcy flow at the center of the domain with the log-permeability variance σ^2 taking the values: 0.125 (grey), 0.25 (red) and 0.5 (blue). The squares represent the results of the finite-volume method, the circles those of simulated annealing.

of the log-permeability is high. The pressure in the main direction takes values in the interval $[0, 1]$, due to the Dirichlet boundary conditions. Given this constraint and the choice of stochastic model for the permeability, the log-normal distribution is an obvious contender for parametric fits to the pressure.

To visualize the dependence of the pressure on its position along the main axis, we have made empirical probability density plots at two positions: $(0.5X, 0.5Y, 0.5Z)$, which is the center of the domain (Figures 20 and 21) and $(0.5X, 0.8Y, 0.5Z)$ (Figures 22 and 23). From the two sets of figures it is apparent that the lognormal distribution is most evident near the boundary. Towards the center of the domain, the histograms bear more resemblance to the normal distribution [1], as the generalized Central Limit Theorem predicts [12]. For a more extensive explanation of this theorem in the context of Darcy flow, see Sec. 6.1. These boundary effects increase with the log-permeability variance, as can also be observed for the flow.

Like the pressure, the flow along the main axis is subject to a non-negativity constraint, which enforces a one-sided bound. The flow could only be negative in the unlikely event of flow reversal due to locally very high permeability. The observed values for the cases considered in this work were non-negative. For the flow, as for the pressure, the shape of the probability density depends on the vicinity to a restricting boundary. We have evaluated the flow in the main direction at the center of the domain. The results are shown in Figures 24 and 25.

One can see that for high values of the log-permeability variance, the flow statistics are most clearly log-normal. This is because the boundary effects are more strongly felt for high values of σ^2, a pattern that can also be observed by comparing Figures 20 and 21 to Figures 22 and 23.

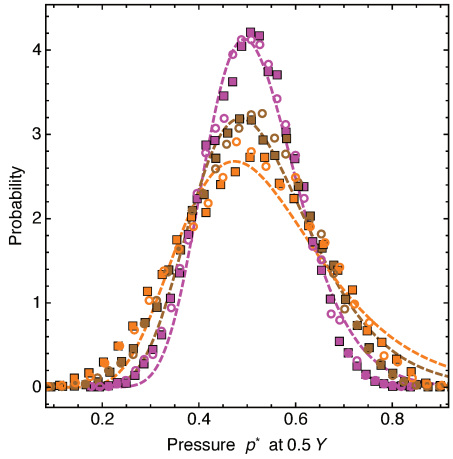

Figure 21: Pressure statistics at the center of the domain, for the remaining values of the log-permeability variance: 1.0 (pink), 1.75 (brown) and 2.5 (orange), as listed in Table 5. The squares represent the results of the finite-volume method, the circles those of simulated annealing.

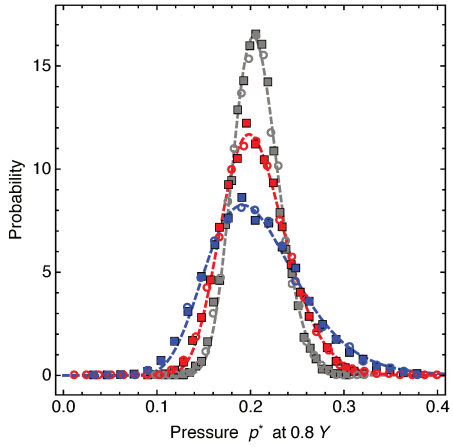

Figure 22: Pressure statistics at the point $(0.5X, 0.8Y, 0.5Z)$ for finite-volume simulations (squares) and simulated annealing (circles) for σ^2 equal to 0.125 (grey), 0.25 (red) and 0.5 (blue).

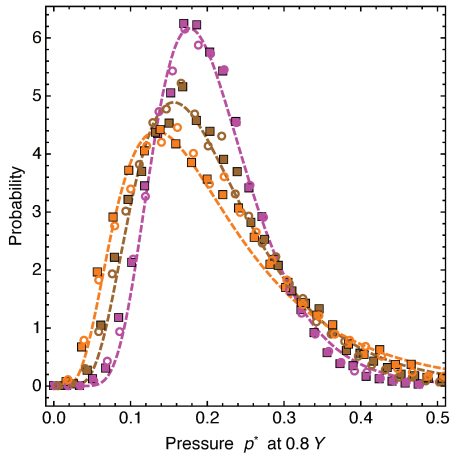

Figure 23: Pressure statistics, again at the point $(0.5X, 0.8Y, 0.5Z)$ for finite-volume simulations (squares) and simulated annealing (circles) for σ^2 equal to 1.0 (pink), 1.75 (brown) and 2.5 (orange).

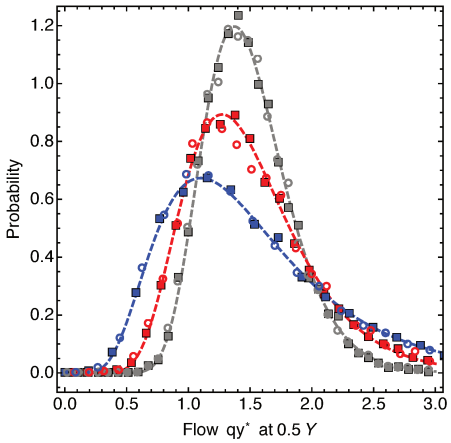

Figure 24: Normalized flow in main direction q_y^* for the log-permeability variances σ^2 equal to 0.125 (grey), 0.25 (red) and 0.5 (blue), measured at the center of the domain.

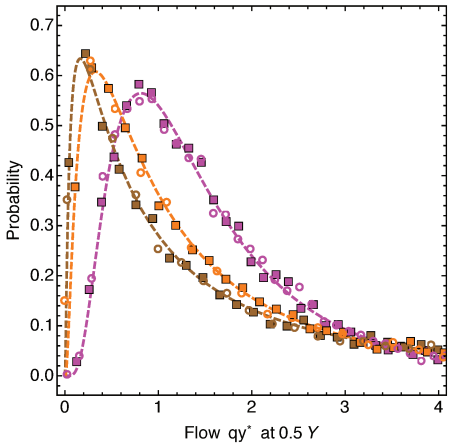

Figure 25: Normalized flow in main direction q_y^*, here for the log-permeability variances σ^2 equal to 1.0 (pink), 1.75 (brown) and 2.5 (orange), again measured at the point $(0.5X, 0.5Y, 0.5Z)$. The log-normal pattern manifests itself most clearly for high values of σ^2. For these high values, the boundary effects, which dictate the log-normality, have the strongest influence on the flow statistics.

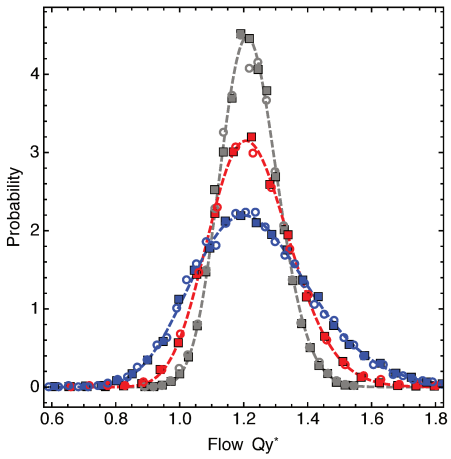

Figure 26: Normalized total flow in the main direction Q_y^* for the values: σ^2 equal to 0.125 (grey), 0.25 (red) and 0.5 (blue). The distribution of Q_y^* resembles that of q_y^* shown in Fig. 24.

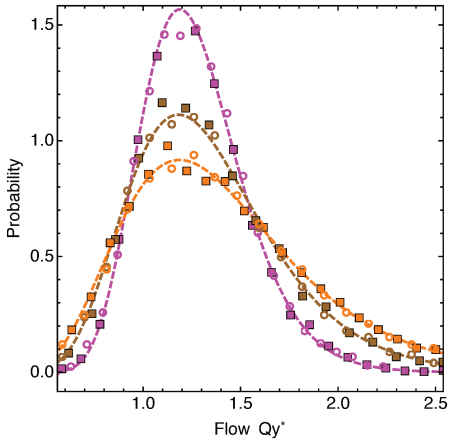

Figure 27: Normalized total flow in the main direction Q_y^* for the values remaining values of σ^2 stated in Table 5. Due to the averaging over a cross-section, the distributions appear more Gaussian.

The total flow in the main direction, defined as the average over a cross-section perpendicular to the y-axis, is conserved along the y-axis. The results can be seen in Figures. 26 and 27.

When comparing Figs. 24 and 25 to Figs. 26 and 27, an obvious difference is that the flow statistics of the total flow approximate the Gaussian distribution more closely. The log-normal distribution tends to the normal distribution in the limit $(\sigma'/\mu')^2 \to 0$. The Gaussian appearance is a result of the averaging over a cross-section that defines the total flow.

To the transverse flow q_x^*, shown in Figures 28 and 29, we fitted an exponential power distribution. This choice reflects the expectation that the transverse flow is symmetric about zero. The probability density function for the exponential power law is:

$$g(x) = \frac{1}{2\sigma''\Gamma(1+1/k)} \exp\left[-\frac{|x-\mu''|^k}{(\sigma'')^2}\right]. \tag{116}$$

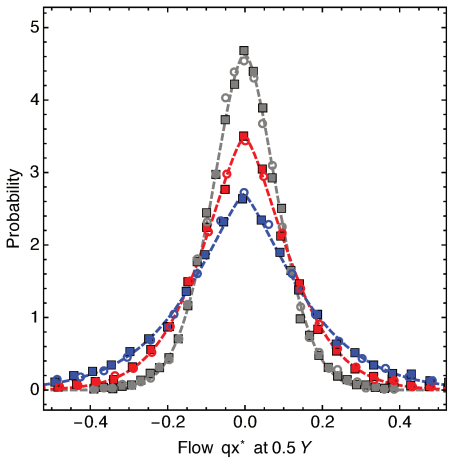

Figure 28: Statistics of the normalized flow in the x-direction, q_x^*, again for the first three elements of the parameter set given in Table 5. The parametric fits of the exponential power distribution reflect the symmetry of the statistics about zero. The tails become heavier for greater values of σ^2.

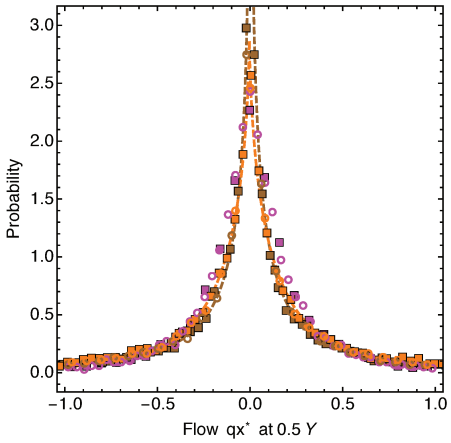

Figure 29: Statistics of the normalized flow in the x-direction, q_x^*, for the final three elements of the parameter set given in Table 5. In the limit $\sigma \gg 1$, the flow either continues along the main axis or "hits a wall" and reverses course. Thus, in this limit, the likelihood of small values for q_x^* is very small.

The Gaussian distribution corresponds to the case $k = 2$. All parametric fits for the parameters $\{\mu', \mu'', \sigma', \sigma'', k\}$ were made using the in-built routine *FindFit* of the package *Mathematica* [54].

A striking feature of the transverse flow statistics are the long and heavy tails. The exponential power distribution was chosen because it reflects this feature. This choice was also made in [76]. The tails are heaviest for high values of the log-permeability variance. In the limit of high variance, the permeability can take a very wide range of values. Thus, it will often occur that the flow either continues along its main axis, or is diverted. This behavior is reflected in the statistics by the tails of the distribution.

9 CONCLUSIONS AND OUTLOOK

In this thesis, we have investigated a path integral approach to Darcy flow through a stochastic permeable medium. The application we have considered is that of the flow of oil through a rock. The differential equation that is Darcy's law can be solved using a discretization technique known as the finite-volume method. Outlines of the finite-volume method in one and more dimensions can be found in Chapters 3 and 7, respectively. The idea to develop a path integral approach to Darcy flow in addition to the existing finite-volume approach was based on the observation that the path integral is a versatile mathematical construct that can be used to capture the physics of virtually any system with a source of noise. Two further considerations seemed to render the path integral well-suited to the case of Darcy flow. First, Darcy flow gives rise to a so-called free field theory (a theory with no higher-order terms in the action). Such theories are mathematically easy to deal with. Sometimes, as in the case of the quantum harmonic oscillator, the corresponding path integral can be solved analytically. More details on the quantum harmonic oscillator are presented in Section 5.1. Second, the conventional finite-volume method relies on the inversion of a large sparse matrix. The path integral would allow one to simulate from the distribution of Darcy pressure directly, thus bypassing the matrix equation. The initial hope was that path integral simulations would be less demanding in terms of computational time and storage. We abandoned that hope while studying the simulation of path integrals on a lattice.

Simulating path integrals on a lattice is a nontrivial exercise. A user's guide to the calculation of path integrals is given in Chapter 5. One has to carefully monitor the autocorrelation within the Markov chain of paths. This autocorrelation depends exponentially on the lattice spacing. While small lattice spacings lead to qualitatively better results, they come at a computational price. Autocorrelation can be addressed by discarding some N_{sep} paths between every two paths used for measurement. This feature of Markov chain Monte Carlo methods makes the path integral for Darcy flow computationally expensive: the computational time for one realization in d dimensions with a total number of Nx^d lattice sites scales with N_x^{2d}. This computational time compares unfavorably with the finite-volume method, whose computational effort scales with $N_x^d \log(N_x^d)$. Room for improvement does exist, in the form of over-relaxation, the multigrid method [46, 56, 68], directed sampling [35, 36, 67], and even analytical methods that systemat-

ically improve the convergence of path integrals [11]. One suggestion for future work would be to optimize the evaluation of the path integral for Darcy flow, to make it computationally competitive. However, there is no a priori argument to suppose that such optimization methods can beat the speed of the finite-voume method.

We have made progress in terms of a stochastic description of the Darcy pressure statistics. Criteria for the validity of a Gaussian approximation are given in Chapter 6. Expressions for Gaussian approximations that do not rely on the pressure simulations are provided in Appendix F, both for Neumann and Dirichlet boundary conditions. Where the Gaussian model is not valid, lognormal parametric fits are shown to approximate the pressure very well. The path integral and finite-volume simulations are shown to pass a Kolmogorov-Smirnov test at the 95% confidence level for all parameter sets considered.

In higher dimensions, Darcy pressure statistics can be obtained through simulated annealing. Given a random permeability field, one minimizes the action for which Darcy's law is the Euler-Lagrange equation; one thus finds the Darcy pressure corresponding to that permeability field. Like the path integral, simulated annealing yields very good agreement with the finite-volume method. The algorithm is conceptually simple, but, like the original Metropolis-Hastings algorithm, suffers from autocorrelation. On the flip side, the hope is that any optimization techniques successfully implemented in one dimension carry over to the higher-dimensional cases.

Another suggestion for future work is the application of the renormalization group, a quantitative framework for systems that fluctuate over many length scales [99, 100]. The idea would be to "coarse-grain" the Darcy flow and analyze its behavior at different scales. The renormalization group has successfully been used to build coarse-scale permeability coefficients [49, 63]. An application of the renormalization group to the stochastic theory of subsurface solute transport can be found in Ref. [41]. Though potentially feasible in any number of dimensions, the problem might change character as a function of dimensionality.

To make the path integral approach to flow through porous media more realistic than the case of single-phase Darcy flow, one could extend it to multiphase Darcy flow. For multiphase flow a generalized form of Darcy's law is used [17]: $q_i = -k_{r,i}(S_i)K\nabla p$, where the subscript i represents the fluid phase (oil, water or gas). The relative permeability $k_{r,i}$ is highly system-specific [26]. The incompressibility constraints still hold for an incompressible fluid. The key question would be whether the coupled equations for the pressure and the flow could be captured in one action, which could then be used for simulated annealing. Anyone interested in following up a simu-

lated annealing approach to Darcy flow is advised start by the construction of a suitable action.

BIBLIOGRAPHY

[1] R. Ababou et al. "Numerical simulation of three-dimensional saturated flow in randomly heterogeneous porous media." In: *Transport in Porous Media* 4.6 (Dec. 1989), pp. 549–565. ISSN: 1573-1634. DOI: 10.1007/BF00223627. URL: https://doi.org/10.1007/BF00223627.

[2] R. Abdelaziz, F. Sussumu Komori, and M. N. P. Carreño. "Multiphase thermal-fluid flow through geothermal reservoirs." In: *Energy Procedia* 95 (2016). International Scientific Conference "Environmental and Climate Technologies", CONECT 2015, pp. 22–28. ISSN: 1876-6102. DOI: https://doi.org/10.1016/j.egypro.2016.09.006. URL: http://www.sciencedirect.com/science/article/pii/S1876102163064 52.

[3] B. Abramovich and P. Indelman. "Effective permittivity of log-normal isotropic random media." In: *Journal of Physics A: Mathematical and General* 28.3 (1995). URL: http://stacks.iop.org/0305-4470/28/i=3/a=022.

[4] J. S. Andrade et al. "Inertial effects on fluid flow through disordered porous media." In: *Phys. Rev. Lett.* 82.26 (June 1999), pp. 5249–5252. DOI: 10.1103/PhysRevLett.82.5249. URL: https://link.aps.org/doi/10.1103/PhysRevLett.82.5249.

[5] S. Aramideh, P. P. Vlachos, and A. M. Ardekani. "Pore-scale statistics of flow and transport through porous media." In: *Phys. Rev. E* 98 (1 July 2018), p. 013104. DOI: 10.1103/PhysRevE.98.013104. URL: https://link.aps.org/doi/10.1103/PhysRevE.98.013104.

[6] K. Aziz and A. Settari. *Petroleum reservoir simulation*. London: Applied Science Publishers, 1979, pp. 135–139.

[7] J. Bear. *Modeling phenomena of flow and transport in porous media*. Switzerland: Springer, 2018.

[8] C. M. Bender and T. T. Wu. "Anharmonic oscillator." In: *Phys. Rev.* 184 (Aug. 1969), pp. 1231–1260. DOI: 10.1103/PhysRev.184.1231. URL: https://link.aps.org/doi/10.1103/PhysRev.184.1231.

[9] B. Berkowitz. "Characterizing flow and transport in fractured geological media: A review." In: *Advances in Water Resources* 25.8 (2002), pp. 861–884. DOI: https://doi.org/10.1016/S0309-1708(02)00042-8. URL: http://www.sciencedirect.com/science/article/pii/S0309170802000428.

[10] Sylvio Bistafa. "On the development of the Navier-Stokes equation by Navier." In: *Revista Brasileira de Ensino de Física* 40 (Nov. 2017). DOI: 10.1590/1806-9126-rbef-2017-0239.

[11] A. Bogojević, A. Balaž, and A. Belić. "Systematically accelerated convergence of path integrals." In: *Phys. Rev. Lett.* 94 (May 2005), p. 180403. DOI: 10.1103/PhysRevLett.94.180403. URL: https://link.aps.org/doi/10.1103/PhysRevLett.94.180403.

[12] J.-Ph. Bouchaud and A. Georges. "Anomalous diffusion in disordered media: statistical mechanisms, models and physical applications." In: *Physics Reports* 195.4 (1990), pp. 127–293. ISSN: 0370-1573. DOI: https://doi.org/10.1016/0370-1573(90)90099-N. URL: http://www.sciencedirect.com/science/article/pii/037015739090099N.

[13] G. E. P. Box and M. E. Muller. "A note on the generation of random normal deviates." In: *Ann. Math. Statist.* 29.2 (June 1958), pp. 610–611. DOI: 10.1214/aoms/1177706645. URL: https://doi.org/10.1214/aoms/1177706645.

[14] F. R. Brown and T. J. Woch. "Overrelaxed heat-bath and Metropolis algorithms for accelerating pure gauge Monte Carlo calculations." In: *Phys. Rev. Lett.* 58 (June 1987), pp. 2394–2396. DOI: 10.1103/PhysRevLett.58.2394. URL: https://link.aps.org/doi/10.1103/PhysRevLett.58.2394.

[15] S. G. Brush. "Functional integrals and statistical physics." In: *Rev. Mod. Phys.* 33 (Jan. 1961), pp. 79–92. DOI: 10.1103/RevModPhys.33.79. URL: https://link.aps.org/doi/10.1103/RevModPhys.33.79.

[16] S. G. Brush. "Resource letter HP-1: history of physics." In: *American Journal of Physics* 55.8 (1987), pp. 683–691. DOI: 10.1119/1.15057. URL: https://doi.org/10.1119/1.15057.

[17] S. E. Buckley and M. C. Leverett. *Mechanism of fluid displacement in sands*. Vol. 1. Society of Petroleum Engineers, Transactions of the AIME, Dec. 1942. DOI: https://doi.org/10.2118/942107-G.

[18] G. Chavent and J. Jaffré. *Mathematical models and finite elements for reservoir simulation*. North Holland: Elsevier, 1986.

[19] S. Chen and G. D. Doolen. "Lattice Boltzmann method for fluid flows." In: *Annual Review of Fluid Mechanics* 30.1 (1998), pp. 329–364. DOI: 10.1146/annurev.fluid.30.1.329. URL: https://doi.org/10.1146/annurev.fluid.30.1.329.

[20] T. C. Coburn, J. M. Yarus, and R. L. Chambers, eds. *Stochastic modeling and geostatistics: principles, methods, and case studies, volume II*. Vol. 5. The American Association of Petroleum Geologists, 2006.

[21] G.-A. Coche. *Multiscale modelling of flow in porous media. MSc thesis submitted to the Centre for Doctoral Training in Theory and Simulation of Materials at Imperial College London*. 2013.

[22] M. Creutz. "Overrelaxation and Monte Carlo simulation." In: *Phys. Rev. D* 36 (July 1987), pp. 515–519. DOI: 10.1103/PhysRevD.36.515. URL: https://link.aps.org/doi/10.1103/PhysRevD.36.515.

[23] M. Creutz and B. Freedman. "A statistical approach to quantum mechanics." In: *Annals of Physics* 132.2 (1981), pp. 427–462. DOI: https://doi.org/10.1016/0003-4916(81)90074-9. URL: http://www.sciencedirect.com/science/article/pii/0003491681900749.

[24] H. Darcy. *Les fontaines publiques de la ville de Dijon. Exposition et application des principes à suivre et des formules à employer dans les questions de distribution d'eau*. Ed. by V. Dalmont. Paris: Libraire des corps impériaux des ponts et chausées et des mines, 1856.

[25] T. A. Davis. "Algorithm 832: UMFPACK V4.3—an unsymmetric-pattern multifrontal method." In: *ACM Trans. Math. Softw.* 30.2 (June 2004), pp. 196–199. ISSN: 0098-3500. DOI: 10.1145/992200.992206. URL: http://doi.acm.org/10.1145/992200.992206.

[26] A. H. Demond and P. V. Roberts. "Estimation of two-phase relative permeability relationships for organic liquid contaminants." In: *Water Resources Research* 29.4 (), pp. 1081–1090. DOI: 10.1029/92WR02987. URL: https://agupubs.onlinelibrary.wiley.com/doi/abs/10.1029/92WR02987.

[27] C. R. Dietrich and G. N. Newsam. "A fast and exact method for multidimensional Gaussian stochastic simulations." In: *Water Resources Research* 29.8 (1993), pp. 2861–2869. DOI: 10.1029/93WR01070. URL: https://agupubs.onlinelibrary.wiley.com/doi/abs/10.1029/93WR01070.

[28] C. R. Dietrich and G. N. Newsam. "Fast and exact simulation of stationary Gaussian processes through circulant embedding of the covariance matrix." In: *SIAM Journal on Scientific Computing* 18.4 (1997), pp. 1088–1107. DOI: 10.1137/S1064827592240555. URL: https://doi.org/10.1137/S1064827592240555.

[29] P. A. M. Dirac. "The Lagrangian in quantum mechanics." In: *Feynman's Thesis — A New Approach to Quantum Theory*, pp. 111–119. DOI: 10.1142/9789812567635_0003. URL: https://www.worldscientific.com/doi/abs/10.1142/9789812567635_0003.

[30] P. A. M. Dirac. *The principles of quantum mechanics*. London: Oxford University Press, 1947.

[31] C. De Dominicis and L. Peliti. "Field-theory renormalization and critical dynamics above T_c: helium, antiferromagnets, and liquid-gas systems." In: *Phys. Rev. B* 18 (July 1978), pp. 353–376. DOI: 10.1103/PhysRevB.18.353. URL: https://link.aps.org/doi/10.1103/PhysRevB.18.353.

[32] H. Dong and M. J. Blunt. "Pore-network extraction from micro-computerized-tomography images." In: *Phys. Rev. E* 80 (Sept. 2009). DOI: 10.1103/PhysRevE.80.036307. URL: https://link.aps.org/doi/10.1103/PhysRevE.80.036307.

[33] I. T. Drummond. "Path-integral methods for turbulent diffusion." In: *Journal of Fluid Mechanics* 123 (1982), pp. 59–68. DOI: 10.1017/S00221208200295X.

[34] K.-L. Du and M. N. S. Swamy. *Search and optimization by metaheuristics*. Switzerland: Springer, 2016.

[35] A. B. Duncan, T. Lelièvre, and G. A. Pavliotis. "Variance reduction using nonreversible Langevin samplers." In: *Journal of Statistical Physics* 163.3 (May 2016), pp. 457–491. ISSN: 1572-9613. DOI: 10.1007/s10955-016-1491-2. URL: https://doi.org/10.1007/s10955-016-1491-2.

[36] A. B. Duncan, N. Nüsken, and G. A. Pavliotis. "Using perturbed underdamped Langevin dynamics to efficiently sample from probability distributions." In: *Journal of Statistical Physics* 169.6 (Dec. 2017), pp. 1098–1131. ISSN: 1572-9613. DOI: 10.1007/s10955-017-1906-8. URL: https://doi.org/10.1007/s10955-017-1906-8.

[37] A. Einstein. "Über einen die Erzeugung und Verwandlung des Lichtes betreffenden heuristischen Gesichtspunkt." In: *Annalen der Physik* 322.6 (), pp. 132–148. DOI: 10.1002/andp.19053220607. URL: https://onlinelibrary.wiley.com/doi/abs/10.1002/andp.19053220607.

[38] R. P. Feynman. "Space-time approach to non-relativistic quantum mechanics." In: *Rev. Mod. Phys.* 20 (Apr. 1948), pp. 367–387. DOI: 10.1103/RevModPhys.20.367. URL: https://link.aps.org/doi/10.1103/RevModPhys.20.367.

[39] R. P. Feynman and A. R. Hibbs. *Quantum mechanics and path integrals*. New York, NY: McGraw-Hill, 1965.

[40] A. R. Freeze. "A stochastic-conceptual analysis on one-dimensional groundwater flow in non-uniform homogeneous media." In: *Water Resources Research* 11 (Oct. 1975), pp. 725–741.

[41] Garrison G. Sposito. "Methods of quantum field theory in the physics of subsurface solute transport." In: *Transport in Porous Media* 42.1 (Jan. 2001), pp. 181–198. DOI: 10.1023/A:1006724801223. URL: https://doi.org/10.1023/A:1006724801223.

[42] C. Gattringer and C. B. Lang. *Quantum chromodynamics on the lattice: an introductory presentation*. Berlin: Springer, 2010.

[43] I. M. Gel'fand and A. M. Yaglom. "Integration in functional spaces and its applications in quantum physics." In: *Journal of Mathematical Physics* 1.1 (1960), pp. 48–69. DOI: 10.1063/1.1703636. eprint: https://doi.org/10.1063/1.1703636. URL: https://doi.org/10.1063/1.1703636.

[44] D. T. Gillespie. "The mathematics of Brownian motion and Johnson noise." In: *American Journal of Physics* 64.3 (1996), pp. 225–240. DOI: 10.1119/1.18210. URL: https://doi.org/10.1119/1.18210.

[45] T. Gneiting et al. "Fast and exact simulation of large Gaussian lattice systems in $\mathbb{R}^2$: exploring the limits." In: *Journal of Computational and Graphical Statistics* 15.3 (2006), pp. 483–501. DOI: 10.1198/106186006X128551. URL: https://doi.org/10.1198/106186006X128551.

[46] J. Goodman and A. D. Sokal. "Multigrid Monte Carlo method for lattice field theories." In: *Phys. Rev. Lett.* 56 (Mar. 1986), pp. 1015–1018. DOI: 10.1103/PhysRevLett.56.1015. URL: https://link.aps.org/doi/10.1103/PhysRevLett.56.1015.

[47] W. G. Gray and K. O'Neill. "On the general equations for flow in porous media and their reduction to Darcy's Law." In: *Water Resources Research* 12.2 (), pp. 148–154. DOI: 10.1029/WR012i002p00148. URL: https://agupubs.onlinelibrary.wiley.com/doi/abs/10.1029/WR012i002p00148.

[48] D. J. Griffiths. *Introduction to quantum mechanics*. 2nd ed. Upper Saddle River, NJ: Pearson Education, Inc., 2005.

[49] S. Hanasoge et al. "Renormalization group theory outperforms other approaches in statistical comparison between upscaling techniques for porous media." In: *Phys. Rev. E* 96 (Sept. 2017). DOI: 10.1103/PhysRevE.96.033313. URL: https://link.aps.org/doi/10.1103/PhysRevE.96.033313.

[50] W. K. Hastings. "Monte Carlo sampling methods using Markov chains and their applications." In: *Biometrika* 57.1 (1970), pp. 97–109. DOI: 10.1093/biomet/57.1.97. URL: http://dx.doi.org/10.1093/biomet/57.1.97.

[51] F. T. Hioe and E. W. Montroll. "Quantum theory of anharmonic oscillators. I. Energy levels of oscillators with positive quartic anharmonicity." In: *Journal of Mathematical Physics* 16.9 (1975), pp. 1945–1955. DOI: 10.1063/1.522747. URL: https://doi.org/10.1063/1.522747.

[52] K. Huang. *Quantum field theory: from operators to path integrals*. 2nd ed. Weinheim: John Wiley & Sons, 2010.

[53] Z. J. Huang and J. M. Tarbell. "Numerical simulation of mass transfer in porous media of blood vessel walls." In: *American Journal of Physiology-Heart and Circulatory Physiology* 273.1 (1997), H464–H477. DOI: 10.1152/ajpheart.1997.273.1.H464. URL: https://doi.org/10.1152/ajpheart.1997.273.1.H464.

[54] Wolfram Research Inc. *Mathematica, version 11.3*. Champaign, IL, 2018.

[55] D. B. Ingham and I. Pop, eds. *Transport phenomena in porous media*. Oxford: Pergamon, 1998.

[56] W. Janke and T. Sauer. "Path integral Monte Carlo using multigrid techniques." In: *Chemical Physics Letters* 201.5 (1993), pp. 499–505. DOI: https://doi.org/10.1016/0009-2614(93)85108-Z. URL: http://www.sciencedirect.com/science/article/pii/000926149385108Z.

[57] R. V. Jensen. "Functional integral approach to classical statistical dynamics." In: *Journal of Statistical Physics* 25.2 (June 1981), pp. 183–210. ISSN: 1572-9613. DOI: 10.1007/BF01022182. URL: https://doi.org/10.1007/BF01022182.

[58] B. Jouvet and R. Phythian. "Quantum aspects of classical and statistical fields." In: *Phys. Rev. A* 19 (Mar. 1979), pp. 1350–1355. DOI: 10.1103/PhysRevA.19.1350. URL: https://link.aps.org/doi/10.1103/PhysRevA.19.1350.

[59] M. Kac. "Wiener and integration in function spaces." In: *Bull. Amer. Math. Soc.* 72 (1966), pp. 52–68.

[60] N. G. van Kampen. *Stochastic processes in physics and chemistry*. 5th ed. Amsterdam: Elsevier, 2004.

[61] A.-R.A. Khaled and K. Vafai. "The role of porous media in modeling flow and heat transfer in biological tissues." In: *International Journal of Heat and Mass Transfer* 46.26 (2003), pp. 4989–5003. DOI: https://doi.org/10.1016/S0017-9310(03)00301-6. URL: http://www.sciencedirect.com/science/article/pii/S0017931003003016.

[62] K. Khanafer, K. Cook, and A. Marafie. "The role of porous media in modeling fluid flow within hollow fiber membranes of the total artificial lung." In: *Journal of Porous Media* 15.2 (2012), pp. 113–122. ISSN: 1091-028X.

[63] P. R. King. "The use of renormalization for calculating effective permeability." In: *Transport in Porous Media* 4.1 (Feb. 1989), pp. 37–58. DOI: 10.1007/BF00134741. URL: https://doi.org/10.1007/BF00134741.

[64] G. Kirchhoff. "Über das Verhältniss zwischen dem Emissionsvermögen und dem Absorptionsvermögen der Körper für Wärme und Licht." In: *Annalen der Physik* 185.2 (1860), pp. 275–301. DOI: 10.1002/andp.18601850205. URL: https://onlinelibrary.wiley.com/doi/abs/10.1002/andp.18601850205.

[65] S. Kirkpatrick, C. D. Gelatt, and M. P. Vecchi. "Optimization by simulated annealing." In: *Science* 220.4598 (1983), pp. 671–680. DOI: 10.1126/science.220.4598.671. eprint: http://science.sciencemag.org/content/220/4598/671.full.pdf. URL: http://science.sciencemag.org/content/220/4598/671.

[66] A. Lang and J. Potthoff. "Fast simulation of Gaussian random fields." In: *arXiv* (). DOI: 10.1515/MCMA.2011.009. URL: https://arxiv.org/abs/1105.2737.

[67] T. Lelièvre, F. Nier, and G. A. Pavliotis. "Optimal non-reversible linear drift for the convergence to equilibrium of a diffusion." In: *Journal of Statistical Physics* 152.2 (July 2013), pp. 237–274. ISSN: 1572-9613. DOI: 10.1007/s10955-013-0769-x. URL: https://doi.org/10.1007/s10955-013-0769-x.

[68] J. S. Liu and C. Sabatti. "Generalised Gibbs sampler and multigrid Monte Carlo for Bayesian computation." In: *Biometrika* 87.2 (2000), pp. 353–369. URL: http://www.jstor.org/stable/2673469.

[69] Z. Liu et al. "Pore-scale characterization of two-phase flow using integral geometry." In: *Transport in Porous Media* 118.1 (May 2017), pp. 99–117. ISSN: 1573-1634. DOI: 10.1007/s11242-017-0849-5. URL: https://doi.org/10.1007/s11242-017-0849-5.

[70] F. J. Massey. "The Kolmogorov-Smirnov test for goodness of fit." In: *Journal of the American Statistical Association* 46.253 (1951), pp. 68–78. DOI: 10.1080/01621459.1951.10500769. URL: https://www.tandfonline.com/doi/abs/10.1080/01621459.1951.10500769.

[71] M. Matsumoto and T. Nishimura. "Mersenne Twister: a 623-dimensionally equidistributed uniform pseudo-random number generator." In: *ACM Trans. Model. Comput. Simul.* 8 (Jan. 1998), pp. 3–30. ISSN: 1049-3301. DOI: 10.1145/272991.272995. URL: http://doi.acm.org/10.1145/272991.272995.

[72] N. Metropolis et al. "Equation of State Calculations by Fast Computing Machines." In: *The Journal of Chemical Physics* 21.6 (1953), pp. 1087–1092. DOI: 10.1063/1.1699114. URL: https://doi.org/10.1063/1.1699114.

[73] I. Montvay and G. Münster. *Quantum fields on a lattice*. Cambridge (UK): Cambridge University Press, 1994.

[74] C. Morningstar. "The Monte Carlo method in quantum field theory." In: *arXiv* (). URL: https://arxiv.org/abs/hep-lat/0702020.

[75] S. P. Neuman. "Theoretical derivation of Darcy's law." In: *Acta Mechanica* 25.3 (Sept. 1977), pp. 153–170. DOI: 10.1007/BF01376989. URL: https://doi.org/10.1007/BF01376989.

[76] W. Nowak et al. "Probability density functions of hydraulic head and velocity in three-dimensional heterogeneous porous media." In: *Water Resources Research* 44.8 (2008). DOI: 10.1029/2007WR006383. URL: https://agupubs.onlinelibrary.wiley.com/doi/abs/10.1029/2007WR006383.

[77] H. Okabe and M. J. Blunt. "Prediction of permeability for porous media reconstructed using multiple-point statistics." In: *Phys. Rev. E* 70 (Dec. 2004). DOI: 10.1103/PhysRevE.70.066135. URL: https://link.aps.org/doi/10.1103/PhysRevE.70.066135.

[78] G. A. Pavliotis. *Stochastic processes and applications*. New York, NY: Springer, 2014.

[79] R. Phythian. "The functional formalism of classical statistical dynamics." In: *Journal of Physics A: Mathematical and General* 10.5 (1977). URL: http://stacks.iop.org/0305-4470/10/i=5/a=011.

[80] W. H. Press et al. *Numerical recipes: the art of scientific computing*. 3rd ed. Cambridge (UK): Cambridge University Press, 2007.

[81] M. H. Quenouille. "Problems in plane sampling." In: *Ann. Math. Statist.* 20.3 (Sept. 1949), pp. 355–375. DOI: 10.1214/aoms/1177729989. URL: https://doi.org/10.1214/aoms/1177729989.

[82] Ph. Renard and G. de Marsily. "Calculating equivalent permeability: a review." In: *Advances in Water Resources* 20.5 (1997), pp. 253–278. ISSN: 0309-1708. DOI: https://doi.org/10.1016/S0309-1708(96)00050-4. URL: http://www.sciencedirect.com/science/article/pii/S0309170896000504.

[83] C. P. Robert and G. Casella. *Monte Carlo statistical methods*. 2nd ed. New York, NY: Springer, 2004.

[84] H. J. Rothe. *Lattice gauge theories*. 4th ed. WORLD SCIENTIFIC, 2012. DOI: 10.1142/8229. URL: https://www.worldscientific.com/doi/abs/10.1142/8229.

[85] D. H. Rothman. "Cellular-automaton fluids: a model for flow in porous media." In: *Geophysics* 53.4 (1988), pp. 509–518. DOI: 10.1190/1.1442482. URL: https://doi.org/10.1190/1.1442482.

[86] J. Rubinstein. "Hydrodynamic screening in random media." In: *Hydrodynamic behavior and interacting particle systems*. Ed. by G. Papanicolaou. New York, NY: Springer US, 1987, pp. 137–149. ISBN: 978-1-4684-6347-7. DOI: 10.1007/978-1-4684-6347-7_12. URL: https://doi.org/10.1007/978-1-4684-6347-7_12.

[87] M. Sahimi. "Flow phenomena in rocks: from continuum models to fractals, percolation, cellular automata, and simulated annealing." In: *Rev. Mod. Phys.* 65 (4 Oct. 1993), pp. 1393–1534. DOI: 10.1103/RevModPhys.65.1393. URL: https://link.aps.org/doi/10.1103/RevModPhys.65.1393.

[88] J. Shao and D. Tu. *The jackknife and bootstrap*. New York, NY: Springer, 1996.

[89] M. A. Tanksley and J. Koplik. "Path-integral variational methods for flow through porous media." In: *Phys. Rev. E* 49 (Feb. 1994), pp. 1353–1366. DOI: 10.1103/PhysRevE.49.1353. URL: https://link.aps.org/doi/10.1103/PhysRevE.49.1353.

[90] G. E. Uhlenbeck and L. S. Ornstein. "On the theory of the Brownian motion." In: *Phys. Rev.* 36 (Sept. 1930), pp. 823–841. DOI: 10.1103/PhysRev.36.823. URL: https://link.aps.org/doi/10.1103/PhysRev.36.823.

[91] G. Upton and I. Cook. *A dictionary of statistics*. 3rd ed. Oxford: Oxford University Press, 2008.

[92] K. Vafai, ed. *Handbook of porous media*. 3rd ed. Boca Raton, FL: CRC, 2015.

[93] B. L. van der Waerden. *Sources of quantum mechanics*. New York, NY: Dover, 1968.

[94] R. L. Wasserstein and N. A. Lazar. "The ASA's Statement on p-values: context, process, and purpose." In: *The American Statistician* 70.2 (2016), pp. 129–133. DOI: 10.1080/00031305.2016.1154108. URL: https://doi.org/10.1080/00031305.2016.1154108.

[95] M. J. E. Westbroek et al. "User's guide to Monte Carlo methods for evaluating path integrals. Supplementary Information." In: *American Journal of Physics* 86.4 (2018), pp. 293–304. DOI: 10.1119/1.5024926. URL: https://doi.org/10.1119/1.5024926.

[96] S. Whitaker. "Flow in porous media I: a theoretical derivation of Darcy's law." In: *Transport in Porous Media* 1.1 (Mar. 1986), pp. 3–25. ISSN: 1573-1634. DOI: 10.1007/BF01036523. URL: https://doi.org/10.1007/BF01036523.

[97] F.W. Wiegel. "Path integral methods in statistical mechanics." In: *Physics Reports* 16.2 (1975), pp. 57–114. ISSN: 0370-1573. DOI: https://doi.org/10.1016/0370-1573(75)90030-7. URL: http://www.sciencedirect.com/science/article/pii/0370157375900307.

[98] N. Wiener. "The average value of a functional." In: *Proc. London Math. Soc.* 22 (1922), pp. 454–467.

[99] K. G. Wilson. "Renormalization group and critical phenomena. I. Renormalization group and the Kadanoff scaling picture." In: *Phys. Rev. B* 4 (Nov. 1971), pp. 3174–3183. DOI: 10.1103/PhysRevB.4.3174. URL: https://link.aps.org/doi/10.1103/PhysRevB.4.3174.

[100] K. G. Wilson. "Renormalization group and critical phenomena. II. Phase-space cell analysis of critical behavior." In: *Phys. Rev. B* 4 (Nov. 1971), pp. 3184–3205. DOI: 10.1103/PhysRevB.4.3184. URL: https://link.aps.org/doi/10.1103/PhysRevB.4.3184.

[101] H. Wio. *Path integrals for stochastic processes: an introduction*. Singapore: World Scientific, 2013.

[102] U. Wolff. "Monte Carlo errors with less errors." In: *Computer Physics Communications* 156.2 (2004), pp. 143–153. DOI: https://doi.org/10.1016/S0010-4655(03)00467-3. URL: http://www.sciencedirect.com/science/article/pii/S0010465503004673.

[103] A. Zamani and B. Maini. "Flow of dispersed particles through porous media — deep bed filtration." In: *Journal of Petroleum Science and Engineering* 69.1 (2009), pp. 71–88. ISSN: 0920-4105. DOI: https://doi.org/10.1016/j.petrol.2009.06.016. URL: http://www.sciencedirect.com/science/article/pii/S0920410509001430.

[104] J. Zinn-Justin. *Path integrals in quantum mechanics*. Oxford: Oxford University Press, 2005.

[105] J. Zinn-Justin. *Quantum field theory and critical phenomena*. 4th ed. Oxford: Clarendon Press, 2002.

A GENERATION OF STANDARD NORMAL RANDOM NUMBERS

This Appendix gives the implementation of two algorithms for the generation of standard Gaussian random variables.

A.1 THE REJECTION METHOD

The rejection method (see, for example, Ref. [83]) is based on the idea that random numbers can be drawn from a distribution whose cumulative density function (cdf) is invertible. This is done using the so-called inverse transform method [91]:

$$y_0 = G^{-1}(u), \tag{117}$$

where $G(x)$ is the cumulative density function, u is drawn from a standard uniform distribution and y_0 is the desired random number.

In the present case, we wish to generate random numbers with the probability function (pdf) $f(x) = 1/\sqrt{2\pi}\exp(x^2/2)$. The distribution with pdf $g(x) = \exp(-x)$ is such that the corresponding cdf is invertible and $g(x)$ majorizes $f(x)$. The rejection method consists of the following steps, illustrated in Fig. 30:

- Draw a random number y_0 from the distribution with pdf $g(x)$.
- Generate a uniform random number $z_0 \in [0, g(y_0)]$ using the Mersenne-Twister algorithm.
- Accept z_0 if and only if $z_0 < f(y_0)$.
- Generate a standard uniform random number u to symmetrize the distribution:

$$y_0 \mapsto \begin{cases} +y_0 \text{ if } u < 0 \\ -y_0 \text{ if } u \geqslant 0. \end{cases} \tag{118}$$

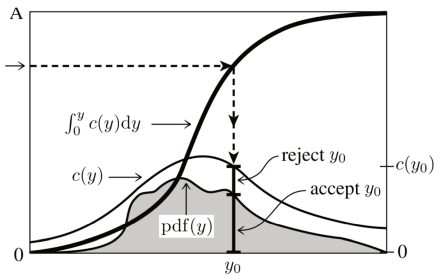

Figure 30: Illustration of the rejection method. The desired pdf is majorized by a function $g(x)$, from which random numbers can be drawn. A sample y_0 is generated according to $g(x)$; a second sample $z_0 \sim \mathcal{U}(0, g(y_0))$ fits the distribution if and only if $z_0 \leqslant f(y_0)$. Source: P. Scott, *Numerical Methods*, lectures notes, Imperial College London (2014).

A.2 THE BOX–MULLER ALGORITHM

Another well-known algorithm is the Box-Muller transform [13]. This method is based on the observation that a pair (X, Y) of independent standard random normal variables will have pdf:

$$f(x, y) = \frac{1}{2\pi} e^{-(x^2+y^2)/2}. \tag{119}$$

The polar representation of (X, Y) is:

$$(X, Y) = R(\cos(\Theta), \sin(\Theta)), \tag{120}$$

with $R > 0$ and $0 \leqslant \Theta < 2\pi$. Because the variable Θ is uniformly distributed on the interval $[0, 2\pi[$, we can write $\Theta = 2\pi u_1$, where $u_1 \sim \mathcal{U}(0, 1)$. The cdf of R can be computed explicitly as:

$$\mathbb{P}(R \leqslant r) = \frac{1}{2\pi} \int_0^r \int_0^{2\pi} e^{-r'^2/2} r' dr' d\theta = 1 - e^{-r^2/2}. \tag{121}$$

Thus, samples of R can be generated using the inverse-transform method:

$$R = \sqrt{-2\log(u_2)}; \quad u_2 \sim \mathcal{U}(0, 1). \tag{122}$$

Two independent standard normals are then given by:

$$X = \sqrt{-2\log(u_2)}\cos(2\pi u_1); \quad Y = \sqrt{-2\log(u_2)}\sin(2\pi u_1). \tag{123}$$

B FUNCTIONAL DERIVATIVES

In the discussion of correlation functions the concept of a generating functional is extremely useful. Let $\{F^{(n)}(x_1,...,x_n)\}$, $n = 0, 1, ...$ be a set of symmetric functions of their arguments. We introduce a function of one variable $f(x)$ and consider the following formal series in f [104]:

$$\mathcal{F}\{f\} = \sum_{n=0}^{\infty} \frac{1}{n!} \int F^{(n)}(x_1,...,x_n) f(x_1)...f(x_n)\, dx_1...dx_n. \tag{124}$$

The functional $\mathcal{F}\{f\}$ is called the generating functional of the functions $F^{(n)}$. The argument function $f(x)$ is known as a source term. To recover the functions $F^{(n)}$ from $\mathcal{F}(f)$, we need the concept of "functional derivative $\delta/\delta f$". Suppose we are interested in the function $F^{(2)}$, known as the two-point correlation function, at the point (ξ_1, ξ_2). We show that

$$F^{(2)}(\xi_1, \xi_2) = \frac{\delta^2 \mathcal{F}\{f\}}{\delta f(\xi_1)\delta f(\xi_2)}|_{f=0}. \tag{125}$$

Here, $\frac{\delta}{\delta f(\xi_1)}$ indicates the functional derivative with respect to f, taken locally at ξ_1. Consider the term for $n = 2$ in Eq. (124). To take the functional derivative of this expression with respect to $f(\xi)$, we consider the variation $\mathcal{F} \to \mathcal{F} + \delta\mathcal{F}$, induced by: $f \to f + \delta f$. The variation δf is defined locally as a delta function with strength ϵ:

$$\delta f = \epsilon\delta(x - \xi), \quad \epsilon \ll 1. \tag{126}$$

Armed with this definition, we take the functional derivative of $\mathcal{F}$ with respect to $f(\xi_1)$. The variation $\delta\mathcal{F}$ in the generating functional is:

$$\begin{aligned} \mathcal{F} + \delta\mathcal{F} &= \frac{1}{2}\int F^{(2)}(x_1, x_2)(f(x_1) + \epsilon\delta(x_1 - \xi_1))f(x_2)\, dx_1\, dx_2 \\ &+ \frac{1}{2}\int F^{(2)}(x_1, x_2)f(x_1)(f(x_2) + \epsilon\delta(x_2 - \xi_1)\, dx_1\, dx_2 \\ = \mathcal{F} &+ \frac{1}{2}\int \epsilon F^{(2)}(\xi_1, x_2)f(x_2)\, dx_2 + \frac{1}{2}\int \epsilon F^{(2)}(x_1, \xi_2)f(x_1)\, dx_1 \end{aligned} \tag{127}$$

Thus, we find

$$\begin{aligned}\frac{\delta\mathcal{F}}{\delta f(\xi_1)} &= \lim_{\epsilon\to 0}\frac{(\mathcal{F}+\delta\mathcal{F})-\mathcal{F}}{\epsilon}\\ &= \mathcal{F}+\frac{1}{2}\int F^{(2)}(\xi_1,x_2)f(x_2)\,dx_2+\frac{1}{2}\int F^{(2)}(x_1,\xi_2)f(x_1)\,dx_1.\end{aligned} \tag{128}$$

We repeat this procedure for $f(\xi_2)$, which yields:

$$\frac{\delta^2\mathcal{F}}{\delta f(x_1)\delta f(x_2)}|_{(x_1,x_2)=(\xi_1,\xi_2)} = \frac{1}{2}F^{(2)}(\xi_1,\xi_2)+\frac{1}{2}F^{(2)}(\xi_1,\xi_2) = F^{(2)}(\xi_1,\xi_2), \tag{129}$$

where we have used the symmetry of the functions $F^{(n)}$ in their indices. All other terms in the sum (124) are zero when we calculate $F^{(2)}$. The terms $F^{(0)}$ and $F^{(1)}$ are killed by the first and second functional derivative, respectively; the other terms reduce to zero when we evaluate $\mathcal{F}$ at $f=0$. This procedure illustrates the use of generating functionals for path integrals:

$$\mathcal{Z} = \int \mathcal{D}\phi\mathcal{D}\phi' \exp\left[-\int l(x)\phi(x)\,dx\right]\exp\left[-S\{\phi,\phi'\}\right]. \tag{130}$$

By taking functional derivatives, we can 'pull down' the desired correlation functions:

$$\begin{aligned}&\frac{1}{\mathcal{Z}}\frac{\delta\mathcal{Z}}{\delta l(x_n)...\delta l(x_1)} =\\ &\frac{1}{\mathcal{Z}}\int \mathcal{D}\phi\mathcal{D}\phi'\phi(x_1)...\phi(x_n)\exp\left[-\int l(x)\phi(x)\,dx\right]\exp\left[-S\{\phi,\phi'\}\right] \equiv\\ &\langle\phi(x_1)...\phi(x_n)\rangle.\end{aligned} \tag{131}$$

C THE PATH INTEGRAL AS A STOCHASTIC INTEGRAL

We show that the path integral can be seen as a stochastic integral. The probability weight associated with each path serves as its probability measure. We first develop the concept of a stochastic integral.

C.1 STANDARD BROWNIAN MOTION

A Brownian motion is a real-valued stochastic process $(W_t)_{t\geqslant 0}$ such that

1. $W_0 = 0$.
2. $W_t - W_s \sim \mathcal{N}(0, t-s)$ for all $0 \leqslant s \leqslant t$, where $\mathcal{N}(\mu, \sigma^2)$ indicates a normal distribution of mean μ and variance σ^2.
3. Increments over non-overlapping time intervals are independent: for all $n \in \mathbb{N}$, such that $0 \leqslant t_1 < ... < t_n$, the increments $W_{t_1}, W_{t_2} - W_{t_1}, ..., W_{t_n} - W_{t_{n-1}}$ are independent.

From this definition it follows that

1. W_t is a Gaussian process.
2. $\mu(t) = \mathbb{E}(W_t) = 0$, for all $t \geqslant 0$, where $\mathbb{E}$ denotes the expectation value.
3. $\mathrm{Cov}(W_t, W_s) = \mathbb{E}(W_t W_s) = \min(t, s)$.
4. For all $a \leqslant b$,

$$\mathbb{P}[W_t \in (a, b)] = \frac{1}{\sqrt{2\pi t}} \int_a^b e^{-\frac{x^2}{2t}} dx. \tag{132}$$

C.2 STOCHASTIC INTEGRALS

The time evolution of a stochastic process is commonly described by a stochastic differential equation (SDE). An SDE is the stochastic analogue of the deterministic ordinary differential equation (ODE):

$$\dot{x}(t) = b(x), \quad x(0) = x_0, \tag{133}$$

which has solution of the form

$$x(t) = x_0 + \int_0^t b(x(s))ds. \tag{134}$$

The "Langevin equation" for one variable is a stochastic differential equation of the form

$$\frac{dX_t}{dt} = b(x,t) + \sigma(x,t)\Gamma_t, \tag{135}$$

where Γ_t is a white noise process. In order to be able to solve SDEs, we will develop a meaningful definition of a stochastic integral in this Section.

We remind ourselves that for a deterministic function $g(t)$ the Riemann integral is defined as

$$\int_0^T g(t)dt := \lim_{n\to\infty} \sum_{j=0}^{n-1} g(t_j)(t_{j+1} - t_j), \tag{136}$$

where $0 = t_0 < t_1 < ... < t_n = T$ defines a partition of the interval $[0, T]$. For a continuous function $g(t)$ the limit does not depend on the chosen point of evaluation $t_* \in [t_j, t_{j+1}]$. For stochastic processes, however, a problem arises when we try to mimic this procedure. Suppose we want to calculate $\int_0^T W_t dW_t$. We consider a partition $0 = t_0 < t_1 < ... < t_n = T$ and evaluate the Brownian motion W_t at the starting point t_j of each interval. This yields

$$\mathbb{E} \sum_{j=0}^{n-1} W(t_j)[W(t_{j+1}) - W(t_j)] = 0,$$

by independence of $W(t_{j+1}) - W(t_j)$ and $W(t_j)$. If, instead, we evaluate W_t at the end point t_{j+1} of each interval, that would give

$$\begin{aligned}&\mathbb{E} \sum_{j=0}^{n-1} W(t_{j+1})[W(t_{j+1}) - W(t_j)] = \\ &\mathbb{E} \sum_{j=0}^{n-1} (W(t_{j+1}) - W(t_j))[W(t_{j+1}) - W(t_j)] \to T (n \to \infty).\end{aligned} \tag{137}$$

This discrepancy due to a different choice of elementary process occurs because Brownian motion, being a stochastic process, has infinite total variation[1],

$$\lim_{n\to\infty} \sum_{t_i \in \Pi_n} |W(t_{i+1}) - W(t_i)| = \infty \text{ a.s.}, \tag{138}$$

1 $X_n \to X$ a.s. (almost surely) means $\mathbb{P}(\lim_{n\to\infty} X_n = X) = 1$.

where Π_n is a sequence of increasingly fine partitions of the interval $[0, t]$. A popular choice of $t_* \in [t_j, t_{j+1}]$ is $t_* = t_j$, which gives the Itō Integral[2]:

$$\int_0^T f(t)\, dW_t \equiv \lim_{n\to\infty} \sum_{j=0}^{n-1} f(t_j)[W(t_{j+1}) - W(t_j)]. \tag{139}$$

Here, $f(t)$ is a stochastic process. An important condition for the construction of the Itō integral is the analogue of square integrability:

$$\mathbb{E}\int_0^T f(t)^2\, dt < \infty. \tag{140}$$

Ref. [78] provides a more formal definition of the stochastic integral in the Itō sense. To compute the integral

$$\int_0^T dW(t), \tag{141}$$

we note that, by definition of Brownian motion, $W(t_n) - W(t_{n-1}) \equiv \Delta W \sim \mathcal{N}(0; \Delta t)$, where $\Delta t = t_n - t_{n-1}$. Therefore, to compute the integral (141), we are integrating the position x with respect to a Gaussian probability density:

$$\int_0^T dW(t) = \frac{1}{\sqrt{2\pi}} \int_0^T \exp\left(-\frac{x^2}{2t}\right)\, dx. \tag{142}$$

Now, consider a particle performing Brownian motion, subject to the constraints

$$\begin{cases} x(t_0) &= x_0 \\ x(t_N) &= x_N. \end{cases} \tag{143}$$

In order to integrate over all possible paths, we need the probability that at time t_j, the particle's position is between x_{j1} and x_{j2}, given its previous position ξ_j at time t_{j-1}:

$$\left(\frac{1}{2\pi}\right)^{1/2} \left(\frac{1}{t_j - t_{j-1}}\right)^{1/2} \int_{x_{j1}}^{x_{j2}} \exp\left[-\frac{1}{2}\frac{(\xi_j - \xi_{j-1})^2}{(t_j - t_{j-1})}\right]\, d\xi_j. \tag{144}$$

2 An alternative that is commonly applied in physics is the Stratonovich integral, defined by $t_* = \frac{1}{2}(t_j + t_{j+1}]$. We shall not explore this here.

The compound probability for all discrete time intervals is given by Eq. (17):

$$\left(\pi^N t_1(t_2-t_1)...(t_N-t_{N-1})\right)^{-\frac{1}{2}} \times \int_{a_1}^{b_1}\int_{a_2}^{b_2}...\int_{a_N}^{b_N} \exp\left\{-\frac{x_1^2}{t_1}-\frac{(x_2-x_1)^2}{t_2-t_1}-...-\frac{(x_N-x_{N-1})^2}{t_N-t_{N-1}}\right\} dx_1...dx_N. \tag{145}$$

In the limit $N \to \infty$, the probability becomes

$$\int_{B.C.} \mathcal{D}\xi \exp\left(-\int_0^T \frac{\dot{\xi}^2}{2}\, dt\right). \tag{146}$$

Expression (146) is a path integral; each path of the free particle is weighed by its classical action.

D PSEUDOCODE

In this Appendix, we present pseudocode for the Metropolis-Hastings algorithm, including a lattice permutation, and the jackknife procedure. The pseudocode can be implemented in any coding language of choice.

D.1 PSEUDOCODE FOR THE METROPOLIS UPDATE

A sweep produces, on average, one attempted update per lattice site and requires $3N_\tau$ random numbers. One third is used to specify the ordering in which the sites are visited, one third for the proposed moves, and one third for the Metropolis accept-reject decision. We note that calling random numbers in batches is faster than generating them one by one.

For a given timeslice τ, the proposed value x_{new} is chosen symmetrically about the present value x_{old}. This is the standard recipe to ensure that the algorithm satisfies detailed balance.

The meaning of the *if* statement in the following routine is summarized as follows. If the action is lowered by the proposed change, $e^{-s_{new}+s_{old}} > 1$, then the change is made. If $s_{new} > s_{old}$, the use of the random number, uniformly distributed in the interval $[0, 1[$, ensures that the proposal is accepted with the probability $e^{-s_{new}+s_{old}}$. The random number randm$[N_\tau + i]$ used in the accept/reject step is different from the number randm$[i]$ used to calculate the proposed new value x_{new}.

The Mersenne-Twister algorithm [71] was used to generate the uniform random numbers. The ideal acceptance rate `idrate` was set to 0.8 at the start of the program.

Within the first `for loop` of the routine "specify site visiting order", a time slice τ may be visited more than once, while another τ is not visited at all. On average, however, there is one proposed update per site. After $N_{sep} \gg 1$ sweeps, the differences in updates between the sites are negligible. Alternatively, this piece of code can be replaced with a call to the following routine, which fills the array `index` with a random permutation of the indices $0, \ldots, N_\tau - 1$.

Input: integers N_τ, array path;
real numbers h, m and ω.
Initialize: real number accrate=0.
Declare: integers τ_{min}, τ_{plu}, i;
real numbers x_{new}, s_{old}, s_{new};
real array randm($2N_\tau$);
integer array index(N_τ)

for ($i = 0$; $i < N_\tau$; $i = i + 1$) — specify site visiting order
 index[i]=floor(N_τ * getrnd());
endfor
for ($i = 0$; $i < 2 * N_\tau$; $i = i + 1$) — getrnd() produces a uniform
 randm[i] = getrnd(); — [0,1[random number.
endfor
for ($i = 0$; $i < N_\tau$; $i = i + 1$)

  τ = index[i];
  $\tau_{min} = (\tau + N_\tau - 1)$ modulo N_τ; — periodic boundary conditions
  $\tau_{plu} = (\tau + 1)$ modulo N_τ;
  x_{new} = path[τ] + h * (randm[i] − 0.5) — proposed new value of path[τ]
  $s_{old} = \frac{1}{2}m(\text{path}[\tau_{plu}] - \text{path}[\tau])^2$
  $+\frac{1}{2}m(\text{path}[\tau] - \text{path}[\tau_{min}])^2$
  $+\frac{1}{2}m\omega^2(\text{path}[\tau])^2$; — current value of the action
  $s_{new} = \frac{1}{2}m(\text{path}[\tau_{plu}] - x_{new})^2$
  $+\frac{1}{2}m(x_{new} - \text{path}[\tau_{min}])^2$ — proposed new value
  $+\frac{1}{2}m\omega^2(x_{new})^2$; — of the action
  if (randm[$N_\tau + i$] < exp($-s_{new} + s_{old}$))
    path[τ] = x_{new}; — build in accepted x_{new}
    accrate=accrate + $1/N_\tau$; — adjustment of acceptance rate
  endif
endfor
$h = h$ * accrate/(idrate) — adjust target interval for future use

Output: path, h.

Table 6: Pseudocode for a Metropolis sweep.

D.2 PSEUDOCODE FOR THE JACKKNIFE AVERAGE

Let O[.] be a one-dimensional array of length N, which contains the measurements O_i, $i = 1 \ldots N$, of the observable O. An unbiased estimator for the sample mean is $mean = sum/N$, where $sum = \sum_{i=1}^{N} O[i]$. An unbiased estimator is obtained this way, regardless of a possible autocorrelation within the set of measurements.

Input: integer N_τ.
Initialize: integer array $p(N_\tau)$.
Declare: integers i, j, k, tmp,
real array randm$(N_\tau - 1)$.

for $(i = 0; i < N_\tau; i = i + 1)$
 p[i]=i; — p contains the indices,
endfor — initially in increasing order.

for $(i = 0; i < N_\tau - 1; i = i + 1)$ — getrnd() produces a uniform [0,1[
 randm[i] = getrnd(); — random number.
endfor

for $(j = N_\tau - 1; j \geqslant 1; j = j - 1)$
 k = floor(double(j) * randm[j − 1]); — random integer between 0 and $j - 1$
 tmp = p[k]; p[k] = p[j]; p[j] = tmp; — interchange p[k] and p[j]
endfor
Output: p.

Table 7: Pseudocode for a permutation of the lattice indices.

In case of uncorrelated data, the statistical uncertainty of the mean is related to the standard deviation of the overall distribution by a factor $1/\sqrt{N}$; [73, 84] that is, the statistical error of the mean is

$$\sqrt{1/(N(N-1))} \sum_{i=1}^{N} \left[(O[i] - \text{mean})^2 \right]. \tag{147}$$

The goal of the jackknife procedure is to generalize this relation to the case where some autocorrelation is present in the data. For example, if the data were only pairwise correlated, we could combine two adjacent measurements, and use the same relation with $N \to N/2$.

A first step is to divide the measurements into N/B blocks or bins, each holding B adjacent measurements. Naturally, the integer B must divide N. The bin size B must be small compared to the total number of measurements for the jackknife error to be based on a sufficient number of block averages, but larger than the autocorrelation time to ensure that correlation between the blocks is minimal. The user is invited to monitor the estimate of the statistical uncertainty as a function of B; it will reach a plateau once B is in the right ballpark.

The second key idea is to operate on "inverse blocks"; that is, on all data but a block of B successive measurements. This is vital if the procedure contains as an intermediate step for example, an effective mass fit to the data in $O[.]$. (With B measurements the fit often fails to converge, while with $N - B$ data elements the fit runs smoothly.)

In the following routine the first `for loop` determines the sample mean. The second calculation consists of an inner and outer loop. The result of the

inner loop, `elim`, is B times the sample mean of one block. In the outer loop, the jackknife estimator is calculated. The jackknife estimator is the average over all variables but those in the block under consideration, hence based on $N - B$ measurements.

The final loop determines the variance of the jackknife estimator, from which the jackknife error follows by taking a square root, with an appropriate prefactor.

```
Input: array O of size N;                 O contains the data;
integer B which divides N.                B is the block size
Declare: integers i, j, n,
real numbers sum, mean, elim,
mean_j, variance_j, error_j;              j is short for "jackknife"
array estimator_j of size N/B;

if (B does not divide N)
  Drop the first few elements of O
  such that B divides the number
  of remaining elements, which
  becomes the new value of N.
endif

sum = 0;
for (n = 0; n < N; n = n + 1)
 sum+ = O[n];
endfor
mean=sum/N                                calculating the sample mean
for (i = 0; i < N/B; i = i + 1)

  elim = 0;
  for(j = i * B; j < i * B + B; j = j + 1)
    elim+ = O[j];                         summing over the ith block
  endfor
  estimator_j[i] = (sum-elim)/(N - B)     ith estimator is based on all
                                          variables except the ith block
endfor

variance_j = 0;
for(i = 0; i < N/B; i = i + 1)
  variance_j+ = (N/B - 1)/(N - B)
  ×(estimator_j[i] - mean)^2;             calculating the jackknife variance
endfor
error_j = sqrt(variance_j)
Output: mean_j; error_j.
```

Table 8: Pseudocode for the jackknife estimator and its error.

E PERMEABILITY

E.1 CONDITIONAL PROBABILITY FOR LOG-PERMEABILITY

The conditional probability density $P(L_2, x_2; L_1, x_1)$ that, given that the log permeability takes the value L_1 at x_1, the value L_2 at x_2 is

$$P(L_2, x_2; L_1, x_1) = \frac{1}{\sqrt{2\pi\sigma^2[1 - e^{-(x_2-x_1)/\xi}]}} \exp\left\{-\frac{1}{2\sigma^2}\frac{[L_2 - L_1 e^{-(x_2-x_1)/\xi}]^2}{1 - e^{-2(x_2-x_1)/\xi}}\right\}. \tag{148}$$

This function is a Gaussian probability density with mean $L_1 e^{-(x_2-x_2)/\xi}$ and variance $\sigma^2[1 - e^{-2(x_2-x_1)/\xi}]$, where ξ is a correlation length. The initial condition for P, when $x_2 = x_1$, is

$$P(L_2, x_1; L_1, x_1) = \delta(L_2 - L_1), \tag{149}$$

and, when $(x_2 - x_1)/\xi \to \infty$, that is, when $x_2 - x_1 \gg \xi$, P approaches a Gaussian distribution for L_2:

$$\lim_{(x_2-x_1)/\xi\to\infty} P(L_2, x_2; L_1, x_1) = \frac{1}{\sqrt{2\pi\sigma^2}} \exp\left(-\frac{L_2}{2\sigma^2}\right). \tag{150}$$

In fact, P in (148) is the Green function for

$$\frac{\partial P}{\partial x} = \frac{1}{\xi}\frac{\partial(\ell P)}{\partial \ell} + \frac{\sigma^2}{\xi}\frac{\partial^2 P}{\partial \ell^2}, \tag{151}$$

which is the Fokker-Planck equation for an Ornstein-Uhlenbeck process with drift $1/\xi$ and diffusion σ^2/ξ.

E.1.1 Expression in terms of the defining SDE

The one-dimensional Ornstein-Uhlenbeck process is also the solution of a specific form of the Langevin equation (see Sect. C.2). In the case of L, the Langevin equation takes the form:

$$dL_x = -\frac{L_x}{\xi}dx + \tilde{\sigma}dW_x, \tag{152}$$

where dW_x represents standard Brownian motion and

$$\frac{\tilde{\sigma}^2 \xi}{2} = \sigma^2. \tag{153}$$

The subscript x in L_x serves as a reminder of the spatial dependence of the process L. Equation (152) can be solved using Itō calculus. We proceed as if (152) were an ordinary differential equation and multiply both sides by the integrating factor $e^{x/\xi}$:

$$e^{x/\xi}\left(dL_x + \frac{L_x}{\xi}dx\right) = e^{x/\xi}\tilde{\sigma}dW_x. \tag{154}$$

Using Itō's formula, which is the chain rule for SDEs, we obtain:

$$d\left(e^{1/\xi}L_x\right) = \frac{1}{\xi}e^{x/\xi}L_x dx + e^{x/\xi}dL_x, \tag{155}$$

hence

$$L_x = e^{-x/\xi}L_0 + \int_0^x e^{-(x-y)/\xi}\tilde{\sigma}dW_y. \tag{156}$$

We are now in a position to calculate the first and second moments of L_x. Taking expectations on both sides and using the fact that an Itō integral has mean zero we find:

$$\mathbb{E}(L_x) = e^{-x/\xi}\mathbb{E}(L_0). \tag{157}$$

For L_x to possess a stationary distribution, $\xi > 0$ is a necessary condition. Using the assumption that L_0 is independent of W_x and letting $\mathbb{E}(L_0) = \mu$, we can write the covariance of L_x as

$$\begin{aligned} \mathrm{Cov}(L_x, L_y) &= \mathbb{E}\left[\left(L_x - e^{-x/\xi}\mu\right)\left(L_y - e^{y/\xi}\mu\right)\right] \\ e^{-(x+y)/\xi}\mathrm{Var}(L_0) &+ \mathbb{E}\left[\int_0^x e^{-(x-u)/\xi}\tilde{\sigma}dW_u \int_0^s e^{-(s-v)/\xi}\tilde{\sigma}dW_v\right]. \end{aligned} \tag{158}$$

Applying the Itō isometry [1] to the second term,

$$\mathbb{E}\left[\int_0^x e^{-(x-u)/\xi}\tilde{\sigma}dW_u \int_0^y e^{-(y-v)/\xi}\tilde{\sigma}dW_y\right] =$$
$$\mathbb{E}\left[\int_0^{\min(x,y)} e^{-(x-u)/\xi-(y-v)/\xi}\tilde{\sigma}^2 du\right] =$$
$$\int_0^{\min(x,y)} e^{-((x+y)-2u)/\xi}\tilde{\sigma}^2 du =$$
$$\frac{\tilde{\sigma}^2\xi}{2}e^{-(x+y)/\xi}\left[e^{2\min(x,y)/\xi}-1\right] =$$
$$\frac{\tilde{\sigma}^2\xi}{2}\left[e^{-|x-y|/\xi}-e^{-(x+y)/\xi}\right]. \tag{159}$$

Taking $s = t$ yields

$$\mathrm{Var}(L_x) = e^{-2x/\xi}\mathrm{Var}(L_0) + \frac{\tilde{\sigma}^2\xi}{2}[1-e^{-2x/\xi}], \tag{160}$$

or, in the case of a deterministic initial condition

$$\mathrm{Var}(L_x) = \frac{\tilde{\sigma}^2\xi}{2}[1-e^{-2x/\xi}], \tag{161}$$

which converges to $\frac{\tilde{\sigma}^2 x_0}{2}$ as $x \to \infty$ provided $\xi > 0$. This suggests that the Ornstein-Uhlenbeck process L_x possesses a stationary distribution $\mathcal{N}(0, \frac{\tilde{\sigma}^2\xi}{2})$. For a proof of the existence of such a distribution, we refer the reader to Ref. [78]. Suppose that $L_0 \sim \mathcal{N}(0, \frac{\tilde{\sigma}^2\xi}{2})$; then

$$\mathrm{Cov}(L_x, L_y) = \frac{\tilde{\sigma}^2\xi}{2}e^{-(x+y)/\xi} + \frac{\tilde{\sigma}^2\xi}{2}\left[e^{-|x-y|/\xi}-e^{-(x+y)/\xi}\right] = \frac{\tilde{\sigma}^2\xi}{2}e^{-|x-y|/\xi},$$

in agreement with Eq. (9) given the substitution (153).

E.2 CORRELATION FUNCTIONS FOR PERMEABILITY

With the initial value L_1 in (148) drawn from a Gaussian probability density with mean zero and variance σ^2,

$$P_0(L_1) = \frac{1}{\sqrt{2\pi\sigma^2}}\exp\left(-\frac{L_1^2}{2\sigma^2}\right), \tag{162}$$

1 The Itō isometry is applicable to all stochastic processes X_t in this study:

$$\mathbb{E}\left(\int_0^X L_x\, dW_x\right)^2 = \mathbb{E}\int_0^X X_x^2\, dx.$$

the expectation value $\mathbb{E}(K(x))$, where $K(x) = e^{L(x)}$, is calculated as

$$\mathbb{E}(K(x)) = \int_{-\infty}^{\infty}\int_{-\infty}^{\infty} e^{L}\, P(L, x; L_0, 0) P_0(L_0)\, dL\, dL_0 = e^{\sigma^2/2}. \tag{163}$$

The two-point correlation function $\mathbb{E}(K(x_1)K(x_0))$ is

$$\begin{aligned}\mathbb{E}(K(x_2)K(x_1)) &= \int_{-\infty}^{\infty}\int_{-\infty}^{\infty} e^{L_2} e^{L_1}\, P(L_2, x_2; L_1, x_1) P_0(L_1)\, dL_1\, dL_2 \\ &= \exp\left\{\sigma^2\left[1 + e^{-(x_2 - x_1)/\xi}\right]\right\}, \end{aligned} \tag{164}$$

from which we obtain

$$\begin{aligned}\mathrm{Cov}(K(x_1)K(x_0)) &= \mathbb{E}(K(x_1)K(x_0)) - \mathbb{E}(K(x_1))\mathbb{E}(K(x_0)) \\ &= e^{\sigma^2}\left\{\exp\left[1 + e^{-(x_1 - x_0)/\xi}\right] - 1\right\}. \end{aligned} \tag{165}$$

The mean and covariance in (163) and (165) are clearly invariant under translations of x. Finally, since $K^{-1}(x) = e^{-L(x)}$, the probability distribution for K^{-1} is identical to that of K.

F GAUSSIAN APPROXIMATIONS

F.1 NEUMANN BOUNDARY CONDITIONS

From Darcy's law and the definition of R in (7), we obtain

$$p(x) = P_i - q_0 R(x)\,, \tag{166}$$

where the initial pressure $P_i = p(0)$. For Neumann boundary conditions, we specify P_i and q_0. If the correlation length is small, we can use the following Gaussian approximation for $p(x)$:

$$p(x) \sim \mathcal{N}(\mu, \sigma^2) = \mathcal{N}\left(P_i - q_0 \mathbb{E}[R(x)],\ q_0^2 \mathrm{Var}(R(x))\right). \tag{167}$$

The first and second moments of $R(x)$ are calculated based on those of the permeability in (163) and (165):

$$\mathbb{E}[R(x)] = \int_0^x e^{\sigma^2/2}\, dx = e^{\sigma^2/2} x \tag{168}$$

$$\mathrm{Var}[R(x)] = e^{\sigma^2} \left\{ \int_0^x \int_0^x e^{\sigma^2 e^{-|x'-x''|/\xi}} - 1\, dx'\, dx'' \right\}. \tag{169}$$

Similarly, the covariance of R is given by:

$$\mathrm{Cov}[R(x), R(y)] = e^{\sigma^2} \left\{ \int_0^x \int_0^y e^{\sigma^2 e^{-|x'-x''|/\xi}} - 1\, dx'\, dx'' \right\}. \tag{170}$$

The expressions in (168), (169), and (170) represent statistical characteristics of the permeability associated with a continuous medium. However, the evaluation of the path integral in Sec. 5.3 is calculated on a lattice with a particular lattice spacing. Thus, for consistency, comparisons between the pressure statistics obtained from the discrete path integral and those calculated directly from the permeability distribution function should be based on discrete approximations to the first and second moments of R. Referring to Fig. 8, we arrive at the following discrete definition of R:

$$R(l)/\delta x = \begin{cases} 0 & \text{if} \quad l = 0 \\ \frac{1}{2}K(1) + \sum_{i=1}^{l-1} K(i) & \text{if} \quad 0 < l < N_x \\ \frac{1}{2}K(1) + \sum_{i=1}^{l-1} K(i) + \frac{1}{2}K(N_x - 1) & \text{if} \quad l = N_x. \end{cases} \tag{171}$$

We concentrate here on the most relevant case: $0 < l < N_x$. The expectation value is then,

$$\mathbb{E}[R(l)/\delta x] = \frac{1}{2}e^{\sigma^2/2} + (l-1)e^{\sigma^2/2} = \left(l - \frac{1}{2}\right) e^{\sigma^2/2}, \tag{172}$$

and the second moment of R is

$$\begin{aligned}\mathbb{E}[R(l)^2/\delta x^2] &= \mathbb{E}\left[\frac{1}{4}K(1)^2 + \sum_{i=1}^{l-1}[K(i)] + \sum_{i=1}^{l-1}\sum_{j=1}^{l-1}[K(i)K(j)]\right] \\ &= \frac{1}{4}e^{\sigma^2} + \sum_{i=1}^{l-1}\left[e^{\sigma^2}e^{1+e^{-1/\xi}}\right] + (l-1)e^{\sigma^2} \\ &\quad +2\sum_{p=1}^{l-1}\left[(l-1-p)e^{\sigma^2\left(1+e^{1+e^{-p/\xi}}\right)}\right].\end{aligned} \tag{173}$$

Subtracting the square of (172) from (173), we obtain an expression for the discrete variance of R:

$$\begin{aligned}\mathrm{Var}[R(l)/\delta x] &= \left(l - \frac{3}{4}\right) e^{\sigma^2} + \sum_{i=1}^{l-1}\left[e^{\sigma^2\left(1+e^{-i/\xi}\right)}\right] \\ &\quad +2\sum_{p=1}^{l-1}\left[(l-1-p)e^{\sigma^2\left(1+e^{-p/\xi}\right)}\right] - \left(l - \frac{1}{2}\right)^2 e^{\sigma^2}\end{aligned} \tag{174}$$

The Gaussian curves in Fig. 13 are based on the discrete definition of R. The continuum definition, $R(x) = \int_0^x e^{-L(x')}\,dx'$, gives rise to the same expectation values, but smaller variances. The discrepancies are due to the discretization of the lattice: in the limit $\delta x \to 0$, the expressions (174) and (169) give rise to the same numerical values. Note, in addition, that R is strictly positive. Because the Gaussian approximation is symmetric, the positivity of R makes for a poor agreement between data and approximation for small values of x, especially for large values of the correlation length.

F.2 DIRICHLET BOUNDARY CONDITIONS

Again, we start from the integrated version of Darcy's law (6). In the Dirichlet formulation, the initial pressure P_i and final pressure $P_f = p(x = X)$ are fixed. Note that

$$q_0 = -\frac{P_f - P_i}{R(X)}. \tag{175}$$

If we let $\Delta p \equiv P_i - P_f$, the pressure is given by

$$p(x) = P_i - \Delta p \frac{R(x)}{R(X)}. \tag{176}$$

To approximate $p(x)$ by a Gaussian random variable, we have to find a Gaussian approximation to the ratio $R(x)/R(X)$, which is of the form [21]

$$Z \equiv \frac{X}{X+Y}, \tag{177}$$

for stochastic variables

$$X = \int_0^x \frac{1}{K(x')}\,dx'; \quad Y = \int_x^X \frac{1}{K(x')}\,dx'. \tag{178}$$

For the choice of stochastic variables (178) in the regime $\xi \gtrsim 0.1X$, which defines the domain of applicability of the Gaussian approximation, we can assume that the mean is much greater than the variance. This assumption is needed to ensure that the fraction Z is a strictly positive quantity, and the cdf of Z can be defined sensibly. We denote the means of X and Y by μ_x and μ_y and the variances by σ_x^2 and σ_y^2, respectively:

$$\begin{cases} X \sim \mathcal{N}(\mu_x, \sigma_x^2) \\ Y \sim \mathcal{N}(\mu_y, \sigma_y^2). \end{cases} \tag{179}$$

In the case of Darcy's law, the assumption (179) translates to:

$$\begin{cases} R(x) \sim \mathcal{N}(\mathbb{E}[R(x)], \mathrm{Var}[R(x)] \\ R(X-x) \sim \mathcal{N}(\mathbb{E}[R(X-x), \mathrm{Var}[R(X-x)]), \end{cases} \tag{180}$$

as given in Equations (168) and (169). Equation (180) holds for $x \leqslant X/2$. If $x > X/2$, the condition

$$\frac{X}{X+Y} \leqslant z \tag{181}$$

becomes

$$\frac{Y}{Y+X} \leqslant 1-z. \tag{182}$$

The discussion below still follows, with the renamed variables. The covariance matrix of X and Y is symbolically denoted by

$$\begin{pmatrix} \sigma_x^2 & c_{xy} \\ c_{xy} & \sigma_y^2 \end{pmatrix},$$

where $c_{xy} \equiv \rho\sigma_x\sigma_y$ is the covariance matrix of X and Y. The symmetric, real, positive-definite covariance matrix admits the Cholesky decomposition

$$\begin{pmatrix} \sigma_x & 0 \\ \sigma_y\rho & \sigma_y\sqrt{1-\rho^2} \end{pmatrix}.$$

The sum $X+Y$ can be written as a linear combination of unit normal ($\sim \mathcal{N}(0,1)$) random variables U and V. We observe that

$$\begin{pmatrix} X & Y \end{pmatrix} \begin{pmatrix} X \\ Y \end{pmatrix} =$$

$$\begin{pmatrix} U & V \end{pmatrix} \begin{pmatrix} \sigma_x^2 & \rho\sigma_x\sigma_y \\ \rho\sigma_x\sigma_y & \sigma_y^2 \end{pmatrix} \begin{pmatrix} U \\ V \end{pmatrix} =$$

$$\begin{pmatrix} U & V \end{pmatrix} \begin{pmatrix} \sigma_x & \sigma_y\rho \\ 0 & \sigma_y\sqrt{1-\rho^2} \end{pmatrix} \begin{pmatrix} \sigma_x & 0 \\ \sigma_y\rho & \sigma_y\sqrt{1-\rho^2} \end{pmatrix} \begin{pmatrix} U \\ V \end{pmatrix};$$

therefore, $X+Y$ has the same distribution as

$$\mu_x + \mu_y + (\sigma_x + \rho\sigma_y)U + \sqrt{1-\rho^2}\sigma_y V. \tag{183}$$

We can now find an expression for the cumulative distribution function of $\frac{X}{X+Y} \equiv Z$:

$$\begin{aligned} F(z) &= \mathbb{P}(Z \leqslant z) \\ &= \mathbb{P}\left\{ \frac{[(1-z)\mu_x - z\mu_y]\sigma_x + [(1-z)\sigma_x^2 - zc_{xy}]U}{z\sqrt{\sigma_x^2\sigma_y^2 - c_{xy}}} < V \right\} \\ &= \mathbb{P}\left\{ \frac{[(1-z)\mu_x - z\mu_y]\sigma_x}{z\sqrt{\sigma_x^2\sigma_y^2 - c_{xy}}} + \frac{[(1-z)\sigma_x^2 - zc_{xy}]}{z\sqrt{\sigma_x^2\sigma_y^2 - c_{xy}}}U - V < 0 \right\}. \end{aligned} \tag{184}$$

Let $W(z) \sim \mathcal{N}(\mu_w(z), \sigma_w^2(z))$, with

$$\begin{aligned} \mu_w(z) &= \frac{[(1-z)\mu_x - z\mu_y]\sigma_x}{z\sqrt{\sigma_x^2\sigma_y^2 - c_{xy}}}; \\ \sigma_w(z) &= \left[\frac{[(1-z)\sigma_x^2 - zc_{xy}]}{z\sqrt{\sigma_x^2\sigma_y^2 - c_{xy}}} \right]^2 + 1; \end{aligned} \tag{185}$$

then $\mathbb{P}(W(z) \leqslant 0) = \mathbb{P}(Z \leqslant z)$. Therefore, the cumulative distribution function of $W(z)$ describes $\mathbb{P}(Z \leqslant z) \equiv F(z)$.

$$\mathbb{P}(W(z) \leqslant 0) = \int_{-\infty}^{0} \frac{1}{\sqrt{2\pi}\sigma_W(z)} e^{-(z-\mu_W(z))^2/(2\sigma_W(z))^2} \, dz. \tag{186}$$

Equation (186) is an analytic formula for $F(z)$. The probability density function is $f(z) = \frac{dF(z)}{dz}$. To obtain a Gaussian approximation to the pressure density, we evaluate $\frac{1}{|\Delta p|} f\left(\frac{z-P_i}{P_f-P_i}\right)$.

G KOLMOGOROV-SMIRNOV TEST

Suppose we have a sample of values $X_1, ..., X_n$ with an unknown probability distribution $\mathbb{P}$ and we would like to test the hypothesis H_0 that it follows a particular distribution $\mathbb{P}_0$. Let us denote by $F(x) = \mathbb{P}(X_1 \leqslant x)$ the cumulative distribution function (cdf) of the underlying distribution, which we assume to be some $F_0(x)$. We define an empirical cdf by:

$$F_n(x) = \mathbb{P}_n(X \leqslant x) = \frac{1}{n}\sum_{i=1}^{n} I(X_i \leqslant x), \tag{187}$$

so that F_n counts the proportion of the sample points below level x. If the hypothesis H_0 is true, the law of large numbers implies that for any x:

$$F_n(x) \to \mathbb{E}I(X_1 \leqslant x) = \mathbb{P}(X_1 \leqslant x) = F_0(x) \ (n \to \infty), \tag{188}$$

i.e., the proportion of the sample in the set $(-\infty, x]$ approximates the cumulative distribution function F_0 at the point x. In order to verify H_0, we calculate the supremum $\sup_{x\in\mathcal{D}} |F_n(x) - F_0(x)|$, which tends to zero in the limit $(n \to \infty)$ under the hypothesis H_0:

$$\sup_{x\in\mathcal{D}} |F_n(x) - F_0(x)| \to 0 \ (n \to \infty). \tag{189}$$

An important observation is the following theorem [70], which we state here without proof:

Theorem G.0.1. *If $F(x)$ is continuous, then the distribution of $\sup_{x\in\mathcal{D}} |F_n(x) - F(x)|$ does not depend on F.*

Let us consider the following statistic:

$$D_n = \sqrt{n} \sup_{x\in\mathcal{D}} |F_n(x) - F_0(x)|. \tag{190}$$

If the null hypothesis H_0 is true, then, by theorem G.0.1, the distribution of D_n depends only on n and, hence, can be tabulated. On the other hand, suppose the null hypothesis fails, $F \neq F_0$. The empirical c.d.f. F_n will converge to F and will not approximate F_0 for large n; we will have

$$\sup_{x\in\mathcal{D}} |F_n(x) - F_0(x)| > \delta \tag{191}$$

for some small parameter δ. Equation (191) implies that, if H_0 fails,

$$D_n = \sqrt{n} \sup_{x \in \mathcal{D}} |F_n(x) - F_0(x)| > \sqrt{n}\delta, \tag{192}$$

which tends to infinity for large n. We therefore work with a decision threshold c to test H_0:

$$\begin{cases} \text{Accept } H_0 & \text{if } D_n \leqslant c \\ \text{Reject } H_0 & \text{if } D_n > c. \end{cases} \tag{193}$$

The threshold c depends on the level of significance α and can be found from the condition:

$$1/x_0 = \mathbb{P}(D_n \geqslant c | H_0). \tag{194}$$

The relevant thresholds can be found from any statistical table book; at the level of significance $\alpha = 0.05$, the threshold is given by $c \simeq 1.358$.